T.C.

DOKUZ EYLÜL ÜNİVERSİTESİ İZMİR ULUSLARARASI BİYOTIP VE GENOM ENSTİTÜSÜ

DEVELOPMENT AND CHARACTERIZATION OF OSIMERTINIB RESISTANT NON-SMALL CELL LUNG CANCER CELL LINE MODELS

SUDE ERİŞ

MOLECULAR BIOLOGY AND GENETICS

MASTER THESIS

İZMİR-2024

THESIS CODE: DEU.IBG.MSc/2021850016

T.C.

DOKUZ EYLÜL ÜNİVERSİTESİ İZMİR ULUSLARARASI BİYOTIP VE GENOM ENSTİTÜSÜ

DEVELOPMENT AND CHARACTERIZATION OF OSIMERTINIB RESISTANT NON-SMALL CELL LUNG CANCER CELL LINE MODELS

MOLECULAR BIOLOGY AND GENETICS

MASTER THESIS

SUDE ERİŞ

Advisor: Prof. Dr. Şerif Şentürk

(This thesis was supported by The Scientific and Technological Research Council of Turkey (TUBITAK) with grant number 122Z890)

THESIS CODE: DEU.IBG.MSc/2021850016

T.C.
DOKUZ EYLÜL ÜNİVERSİTESİ

İZMİR ULUSLARARASI BİYOTIP VE GENOM ENSTİTÜSÜ

YÜKSEK LİSANS TEZ SAVUNMA SINAVI TUTANAĞI

Dokuz Eylül Üniversitesi İzmir Uluslararası Biyotıp ve Genom Enstitüsü Genom Bilimleri ve Moleküler Biyoteknoloji Anabilim Dalı Moleküler Biyoloji ve Genetik Yüksek Lisans Programı 2021850016 numaralı öğrencisi Sude Eriş "Development and Characterization of Osimertinib Resistant Non-Small Cell Lung Cancer Cell Line Models" konulu Yüksek Lisans tezini 23.08.2024 tarihinde yapılan savunma sınavı sonucunda başarılı / ~~[illegible]~~ olmuştur.

BAŞKAN

Prof. Dr. Şerif Şentürk

JÜRİ ÜYESİ

Dr. Öğr. Üyesi Yavuz Oktay

JÜRİ ÜYESİ

Prof. Dr. Özden Yalçın-Özuysal

TABLE OF CONTENTS

LIST OF TABLES

LIST OF FIGURES

ABBREVIATIONS

NSCLC: Non-small cell lung cancer

KRAS: Kirsten rat sarcoma viral oncogene homologue

PBS: Phosphate Buffered Saline

FDA: US Food and Drug Administration

PCR: Polymerase chain reaction

RIPA: Radioimmunoprecipitation assay buffer

BrdU: Bromodeoxyuridine (5-bromo-2'-deoxyuridine)

IF: Immunofluorescence

EGFR: Epidermal growth factor receptor

FBS: Fetal Bovine Serum

qRT-PCR: Quantitative Real Time Polymerase Chain Reaction

LCV2-Blast: LentiCRISPR-v2 Blasticidin

OsiR: Osimertinib-resistant

IC50: Half-maximal inhibitory concentration

MTT: 3-(4,5-Dimethylthiazol-2-yl)-2,5-Diphenyltetrazolium Bromide

qRT-PCR: Quantitative Real Time Polymerase Chain Reaction

PI: Propidium Iodide

P/S: Penicillin/Streptomycin

GSEA: Gene Set Enrichment Analysis

ACKNOWLEDGEMENT

First of all, I would like to express my endless gratitude to my advisor Prof. Dr. Şerif Şentürk, who has guided me with his valuable contributions and guidance at every stage of this study. Without his knowledge, motivation and patience, it would not have been possible to complete this study.

I would also like to thank my jury members Prof. Dr. Özden Yalçın-Özuysal and Assist. Prof. Yavuz Oktay, who provided me with valuable feedback during the thesis defense process and contributed to the development of my study. I would also like to thank Prof. Dr. Gökhan Karakülah, who provided me with a solid foundation in bioinformatic analyses and shared his valuable knowledge.

I thank TÜBİTAK-BİDEB 2210/A National MSc/MA Scholarship Program for their bursary support during my Master's studies. Also, the numerical calculations reported in this thesis were partially performed at TUBITAK ULAKBIM, High Performance and Grid Computing Center (TRUBA resources).

Another gratitude goes to my laboratory colleagues who have contributed and supported me the most during my last 3 years in İzmir. I would like to thank Dr. Ece Çakıroğlu, who has been and will continue to be by my side at every moment, good or bad, and for picking me up again whenever I fall. I would also like to thank Bengisu Uluata-Dayanç, who patiently trained me when I came to this lab 3 years ago with no experience. I would like to thank Medine Zeynep Güngör, whose determination I admire, for supporting me and being there for me under all circumstances. I would like to thank Nazife Ege Gülfırat, whose presence alone is enough to make me laugh, for encouraging me under all circumstances. I would also like to thank our researcher Minenur Kalyoncu for facilitating and helping me not only technically but also in every sense. When I first came to this lab, we were a small team, but now we are a big team of 12; in this context, I would like to

thank all the old and new Şentürk Lab members for everything they contributed to me during my master's degree.

Last but not the least, I would like to express my deepest gratitude to my family for always being there for me, for their endless support, and for strengthening me through this process with their patience and love. This journey would have been much more difficult without your presence and belief.

DEVELOPMENT AND CHARACTERIZATION OF OSIMERTINIB RESISTANT NON-SMALL CELL LUNG CANCER CELL LINE MODELS

Sude Eriş, Dokuz Eylul University Izmir International Biomedicine and Genome Institute, edu.tr

ABSTRACT

Non-small cell lung cancer is the most common subtype of lung cancer and the leading cause of cancer death worldwide. Ligand-independent oncogenic activation of the EGFR is frequently seen in adenocarcinomas, which is the most common subtype of NSCLC. This activation is mostly due to mutations in the EGFR tyrosine kinase domain (most commonly: ex19del and L858R). EGFR-TKIs are used to treat advanced NSCLC patients with this mutation profile. Osimertinib is a third-generation EGFR-TKI that irreversibly inhibits EGFR-activating mutations as well as the EGFR-T790M resistance mutation that frequently occurs in patients treated with first- and second-generation EGFR-TKI's. Despite its superior efficacy, drug resistance is inevitable in osimertinib treatment. Activation of alternative downstream signaling pathways, as well as genetically encoded EGFR mutations that prevent osimertinib binding, are known resistance mechanisms. Although many mechanisms have been described in the literature on osimertinib resistance, the diversity of these resistance mechanisms further complicates treatment. The aim of this study is to obtain these osimertinib-resistant cellular models, present a detailed characterization of these models, and contribute to the understanding of the mechanisms underlying osimertinib resistance. For this purpose, two osimertinib-resistant NSCLC cell lines were developed. The cells were characterized with various cellular and molecular experiments, and it was revealed that osimertinib-resistant cells lost EGFR dependence. In addition, whole genome RNA sequencing was performed, and it was shown that the transcriptomic profiles of the cells changed as they gained resistance. Our findings show that the resistant cells obtained are compatible with the models in the

literature and have their mechanisms. In conclusion, these cell models could lead to the identification of osimertinib resistance mechanisms using different omics techniques or the development of drugs to target these resistance mechanisms.

Keywords: NSCLC, osimertinib resistance, cell models, RNA-seq

OSİMERTİNİB DİRENÇLİ KÜÇÜK HÜCRELİ OLMAYAN AKCİĞER KANSERİ HÜCRE HATTI MODELLERİNİN GELİŞTİRİLMESİ VE KARAKTERİZASYONU

Sude Eriş, Dokuz Eylül Üniversitesi İzmir Uluslararası Biyotıp ve Genom Enstitüsü, subg.edu.tr

ÖZET

Akciğer kanserinin en çok görülen türü olan küçük hücreli dışı akciğer kanseri, tüm akciğer kanseri vakalarının %85'ini oluşturur ve dünya çapında kansere bağlı ölümlerin önde gelen nedenidir. KHDAK en yaygın alt tipi olan adenokarsinomlarda sıklıkla epidermal büyüme faktörü reseptöründe onkogen aktivasyonu görülür. Bu aktivasyon çoğunlukla EGFR tirozin kinaz domainindeki mutasyonlardan kaynaklanır. Bu yüzden EGFR aktivasyonuna sahip ileri evre hastaların tedavisinde EGFR tirozin kinaz inhibitörleri kullanılmaktadır. Birinci ve ikinci nesil EGFR-TKI'lerin etkili yanıtına rağmen, hastalar belirli bir süre sonra ilaçlara karşı direnç kazanmaktadır. Bu dirence sebep olan en yaygın mekanizma EGFR'de oluşan sekonder T790M direnç mutasyonudur. Osimertinib, birinci ve ikinci nesil EGFR-TKI'lerle tedavi edilen hastalarda sıklıkla ortaya çıkan EGFR-T790M direnç mutasyonunun yanı sıra EGFR aktive edici mutasyonları geri dönüşümsüz olarak inhibe eden üçüncü nesil EGFR-TKI'dir. Osimertinib başlangıçta ikinci basamak tedavide kullanılmış olsa da EGFR mutant KHDAK hastalarında gelişmiş sağkalım nedeniyle birinci basamak tedavide de FDA onayı almış tek EGFR-TKI'dir. Daha önceki EGFR-TKI'lere benzer şekilde, osimertinib tedavisinde de direnç kaçınılmazdır. Osimertinib'e karşı direnç mekanizmaları, EGFR mutasyonlarını ve alternatif sinyal yollarının anormal aktivasyonunu içerir ve dirençli hücrelerin yüksek heterojenitesi sebebiyle direnç mekanizmaları çeşitlidir. Bu bağlamda osimertinib direnci farklı hücre hatları arasında da çeşitlilik gösterir ve genelleştirilmesi zordur. Osimertinib direncine ilişkin literatürde birçok mekanizma tanımlanmış olsa da bu direnç mekanizmalarının çeşitliliği tedaviyi daha da karmaşık hale getirmektedir. Bu çalışmanın amacı, bu osimertinib dirençli hücresel

modelleri elde etmek, bu modellerin ayrıntılı bir karakterizasyonunu sunmak ve osimertinib direncinin altında yatan mekanizmaların anlaşılmasına katkıda bulunmaktır. Bu amaçla, iki osimertinib dirençli KHDAK hücre hattı geliştirildi. Hücreler çeşitli hücresel ve moleküler deneylerle karakterize edildi ve osimertinib dirençli hücrelerin EGFR bağımlılığını kaybettiği ortaya çıktı. Ayrıca, tüm genom RNA-dizileme yapıldı ve hücrelerin transkriptomik profillerinin direnç kazandıkça değiştiği gösterildi. Bulgularımız, elde edilen dirençli hücrelerin literatürdeki modellerle uyumlu olduğunu ve mekanizmalarına sahip olduğunu göstermiştir. Sonuç olarak, bu hücre modelleri farklı omik teknikleri kullanarak osimertinib direnç mekanizmalarını belirlemeye veya direnç mekanizmalarını hedef alacak ilaçların geliştirilmesine öncülük edebilir.

Anahtar kelimeler: KHDAK, osimertinib direnci, hücresel modeller, RNA-dizileme

1. AIM OF THE STUDY

The aim of this thesis is to develop and comprehensively characterize novel cellular models of osimertinib resistance in non-small cell lung cancer (NSCLC). This work will focus on generating two osimertinib-resistant NSCLC cell lines and evaluating their molecular, cellular, and transcriptomic profiles to establish a robust platform for future research. The specific objectives of the thesis are:

1. **Development of Cellular Models:** To generate and validate osimertinib-resistant sublines from NSCLC cells with EGFR mutations, ensuring that these models accurately represent the resistance mechanisms observed in clinical scenarios.
2. **Molecular Characterization:** To investigate changes in gene expression, protein levels, and key signaling pathways linked to resistance. This includes analyzing alterations in EGFR and its downstream signaling pathways, as well as other relevant molecular markers.
3. **Cellular Characterization:** To examine changes in cell morphology, proliferation rates, and survival under osimertinib treatment, providing insights into the impact of resistance on cellular behavior and drug responsiveness.
4. **Transcriptomic Profiling:** To conduct high-throughput RNA sequencing to identify differential gene expression profiles and decode the transcriptomic landscape associated with osimertinib resistance.

The ultimate goal is to offer a detailed characterization of these cellular models, establishing a solid basis for future research into the underlying mechanisms of resistance. By enhancing our understanding of the molecular, cellular, and transcriptomic changes in these models, this thesis will potentially contribute to the foundation for exploring further aspects of osimertinib resistance.

2. INTRODUCTION

2.1. Lung Cancer and Its Histological Subtypes

According to 2022 Global Cancer Observatory data, lung cancer is the most common type of cancer, with 2.5 million new cases (1,2). As of 2024, lung cancer is the leading cause of cancer-related deaths among both women and men in the United States (3). The high mortality rate is largely attributed to the delayed onset of clinical symptoms, which often results in diagnosis at advanced stages (4). Nevertheless, the treatment of non-small cell lung cancer has evolved significantly in recent years, driven by advances in targeted therapies and immunotherapy. Historically, treatment options for NSCLC included surgery, radiation therapy, and chemotherapy, which were tailored based on the stage and characteristics of the disease (5). However, the emergence of targeted therapies, which will be discussed in greater detail later, has revolutionized the management of NSCLC. Drugs such as tyrosine kinase inhibitors (TKIs) have been developed to specifically target mutations in genes like EGFR, ALK, and ROS1, providing more personalized and effective treatment options (6).

Lung cancer is divided into two subtypes: small-cell lung cancer (SCLC) and non-small cell lung cancer (NSCLC) (7).

These subtypes are characterized by their distinct driver mutations, unique morphologies, and aggressive behaviors. In addition, response to treatment plays a crucial role in categorizing this cancer into these histological subtypes (8). SCLC accounts for approximately 15% of all lung cancer cases and is a relatively indolent type of cancer that is surgically respectable (9). NSCLC represents 85% of all cases, is highly aggressive, and tends to metastasize. Importantly, NSCLC is divided into three histological subtypes: lung adenocarcinoma, large cell carcinoma, and squamous cell carcinoma (10). Among these, lung adenocarcinoma is the most common type of NSCLC (Figure 1).

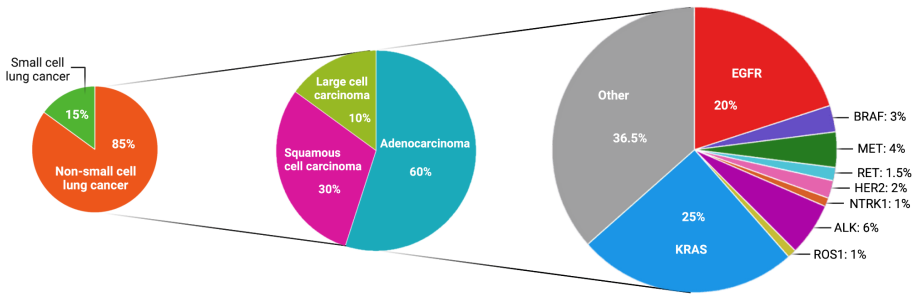

Figure 1: Histological classification of lung cancer subtypes and schematic representation of the driving mechanisms responsible for NSCLC carcinogenesis (11).

Different genetic mechanisms are implicated in the carcinogenesis of lung adenocarcinoma. These genetic abnormalities may result from mutations in more than one gene, or a single gene abnormality which directly contributes to carcinogenesis. Among many others, mutations in the *KRAS* and *EGFR* genes are the most frequent driver alterations (12). Most critically, these mechanisms are considered druggable targets. Treatment approaches vary depending on the specific mutated gene driving the cancer in each patient. Of particular importance to mention, mutations in the *KRAS* gene are not unique to lung cancer but also occur in other cancers, such as colorectal and pancreatic cancer (13,14). The *KRAS* G12C mutation, notoriously difficult to target, has recently become actionable with the development of two inhibitors, sotorasib and adagrasib, which are now used to treat NSCLC patients harboring this mutation (15). Gene fusions or chromosomal rearrangements are another significant driving mechanism in carcinogenesis (16). The *ALK* gene is particularly prone to chromosomal rearrangements with various fusion partners, with the EML4–ALK rearrangement being the most common gene fusion observed in NSCLC. For patients with this gene fusion, treatment is primarily based on ALK tyrosine kinase inhibitors (17).

The *EGFR* gene, the second most common driver mutation, is a major focus of research and offers a broad range of treatment options. Among these, EGFR tyrosine kinase inhibitors (EGFR-TKI) are widely used to target NSCLC cases with oncogenic EGFR mutations (18).

2.2. Epithelial Growth Factor Receptor (EGFR)

Human *EGFR* gene, also known as ErbB1, is a member of ErbB/HER receptor tyrosine kinase family (19). This family also includes *ErbB2* (neu, HER2) and *ErbB3* (HER3) and *ErbB4* (HER4) genes (Figure 2). These genes encode different types of receptors, and these receptors mainly consist of 5 main parts; extracellular domain, hydrophobic transmembrane segment, juxtamembrane segment located at intracellular, protein kinase domain and a carboxyterminal tail (20). Among these, the ligand binding domain of the *HER2* gene is defective, while the tyrosine kinase domain of the HER3 gene is not functional. Therefore, these receptors must heterodimerize with other members of the ErbB family in order to achieve their functionality (21–23). Among the ErbB family proteins, EGFR is the most studied due to its critical role in various cancers and its significant implications for targeted therapy development (24).

The *EGFR* gene is located at the short arm of chromosome 7 (7p11.2) and encodes a 170 kDa polypeptide of 1,210 amino acids with a total of 28 exons (20,25). The EGFR protein has three distinct regions: the extracellular region where the ligand binds, the transmembrane region, and the tyrosine kinase domain (TKD) located in the intracellular compartment that mediates signal transduction (20,26). There are currently seven different ligands known to mediate EGFR signaling activation, including epidermal growth factor (EGF), transforming growth factor-α (TGF-α), amphiregulin (AREG), heparin-binding EGF-like growth factor (HBEGF), betacellulin (BTC), epiregulin (EREG), and epigenin (EPGN) (27–29).

The EGFR signaling pathway is initiated by binding a ligand to the receptor's extracellular domain, leading to heterodimerization of EGFR with other ErbB family members or homodimerization with itself (30). After dimerization, the signal is transmitted to the transmembrane domain, causing conformational changes and rearrangements in the

juxtamembrane segment. The intracellular juxtamembrane segment interacts with the tyrosine kinase domain, thus maintaining the stability of the dimerized EGFR (20). After interaction in the tyrosine kinase domain, intracellular signaling occurs via autophosphorylation of tyrosine residues at the C-terminus. Phosphorylation at tyrosine residues is the most important step for EGFR signaling. When phosphorylated, they create docking sites for other substrates and initiate downstream signaling pathways, such as PI3K-AKT, MAPK and JAK/STAT (Figure 2) (31). Signaling pathways stimulated by EGFR regulate a variety of important cellular and biological functions, such as cell proliferation, differentiation, growth, and cell migration (25). As first mentioned in a review article by Thompson and Gill in 1985, overexpression of EGFR has been associated with various cancers and is the first receptor to provide evidence of this association (20,32).

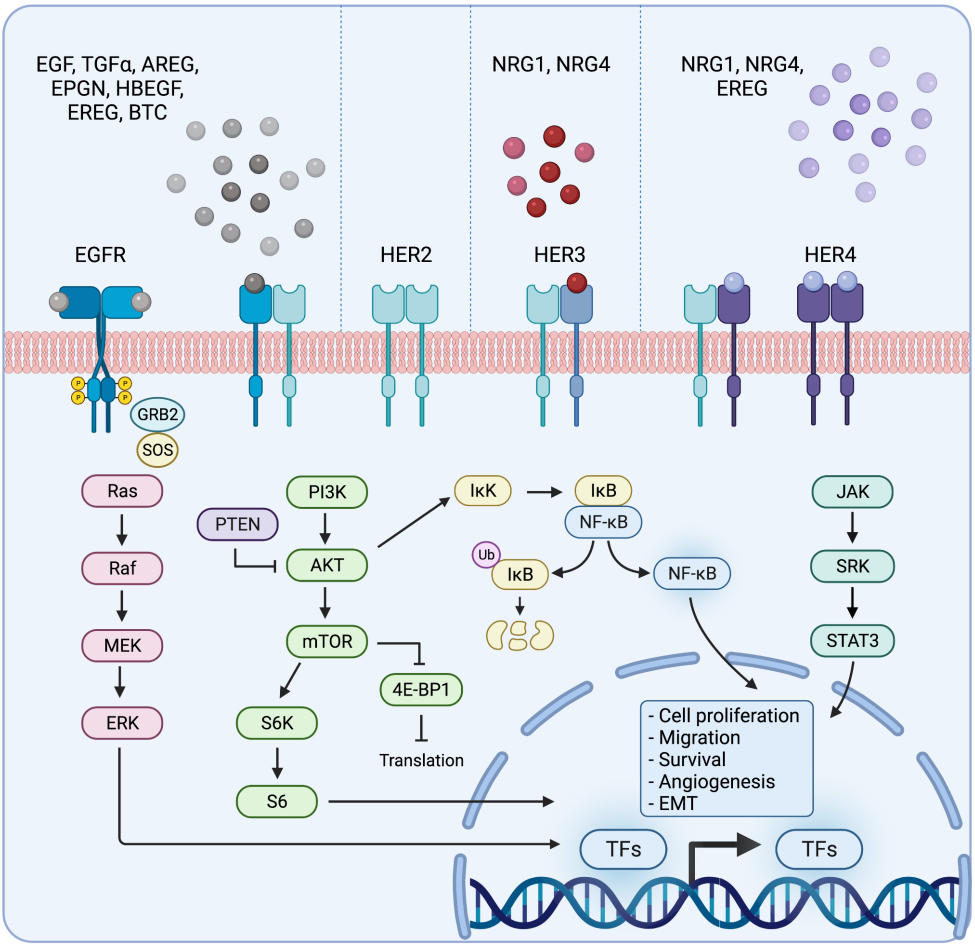

Figure 2: ErbB family members and their downstream pathways (11).

2.3. EGFR Activating Mutations

According to the COSMIC database, EGFR mutations are frequently observed in various cancer types and are present in approximately 20% of lung adenocarcinoma cases (11,20). Although not the most common mutation in NSCLC, EGFR mutations are particularly well-characterized in this context due to their significant sensitivity to EGFR-TKIs (33). The high frequency of *EGFR* somatic mutations in NSCLC, coupled with the strong response of *EGFR*-mutated NSCLC patients to EGFR-TKIs, highlights the critical role of *EGFR* mutations in supporting the malignant phenotype of these tumors (34).

In brief, somatic mutations typically occur within the tyrosine kinase domain, a region crucial for EGFR function. These mutations affect the ATP binding site, causing a conformational change that drives the EGFR protein into a constitutively active state (35). In other words, the receptor becomes capable of activation in a ligand-independent manner (25,36). Due to this continuous activation, these mutations are referred to as "activating mutations" (37).

To elaborate further, *EGFR* activating mutations occur within the tyrosine kinase domain of the gene, specifically in exons 18-21 (Figure 3) (34). These mutations are categorized into three classes based on their type. **Class I mutations** involve in-frame deletions. The prevalent mutation in this category is the exon 19 deletion, which results from a 15-nt deletion, leading to the removal of the ELREA amino acid sequence at positions 746-750 in the protein (del E746-A750). This mutation is the most prevalent, accounting for approximately 45% of all EGFR-mutated NSCLC cases (38,39). **Class II mutations** are single nucleotide substitutions, with the L858R mutation being the second most common. This mutation accounts for about 40% of all EGFR-mutated NSCLC cases (39). It occurs when thymidine is substituted by guanine at position 2573 in exon 21, resulting in the replacement of leucine (L) with arginine (R) at position 858 in the protein (40). **Class III**

mutations are in-frame duplications and/or insertions, with the most common being the exon 20 insertion. However, this mutation represents only about 5% of all EGFR-mutated NSCLC cases (39). In summary, the exon 19 deletion and the L858R mutation, which together account for 85% of all *EGFR* mutations, are referred to as classical activating mutations, while the remaining 15% are known as rare activating mutations (34).

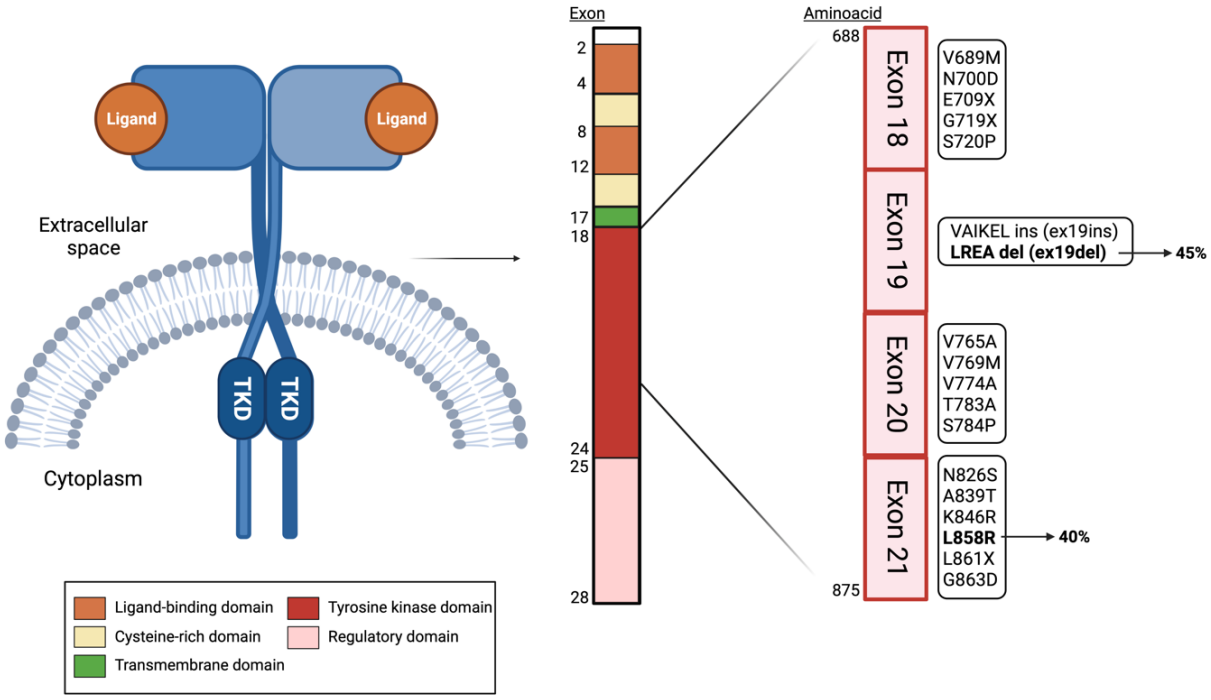

Figure 3: Schematic representation of EGFR and activating mutations in the tyrosine kinase domain (11).

As alluded to earlier, EGFR activating mutations disrupt the inactive conformation of the receptor, leading to ligand-independent dimerization and constitutive activation (41). Most notably, the specific type of activating mutation defines the mechanism of EGFR overactivation (42). The tyrosine kinase domain of EGFR comprises three key regions: the N-terminal lobe, the C-terminal lobe, and the ATP binding site located between these

two lobes (42,43). The exon 19 deletion enhances EGFR activation by disrupting a structural motif known as the β3-αC loop, which is highly conserved among oncogenes and is located in the N-terminal lobe of EGFR (44). This deletion, which removes the LREA amino acids, results in a physical alteration that stabilizes the αC-helix, thereby increasing the stability of the receptor's active form (44,45). In contrast, the L858R mutation impacts EGFR differently. In the wild-type EGFR, leucine at position 858 is a non-polar residue, but when mutated to arginine, a basic residue, the amino acid side chain undergoes a significant change. This radical conformational shift leads to the constitutive activation of the tyrosine kinase domain (7,12,13). To put it differently, the replacement of non-polar leucine with positively charged arginine disrupts the hydrophobic interactions that stabilize the inactive conformation, thereby favoring the active form (46). These mutations not only trigger EGFR activation but also differentially affect the stability of its active form. In the case of the exon 19 deletion, the limited mobility of the αC-helix confers greater stability to the active conformation (44). Conversely, with the L858R mutation, the disrupted hydrophobic interactions decrease the stability of the inactive form, making it easier for the EGFR protein to adopt the active conformation (45,46).

Changes in EGFR stability due to various mutations significantly impact treatment response and overall survival rates, depending on the specific mutation present in the patient (11,47). A study by Carey et al. demonstrated that the IC50 dose of EGFR-TKIs was lower in NSCLC cell lines with the exon 19 deletion compared to those with the L858R mutation, indicating that the exon 19 deletion is more sensitive to treatment, with binding kinetics occurring more readily (47). Interestingly, research by Shigematsu et al., as shown in Figure 4, found that the overall survival rate of patients with the L858R mutation was higher than that of patients with the exon 19 deletion (48).

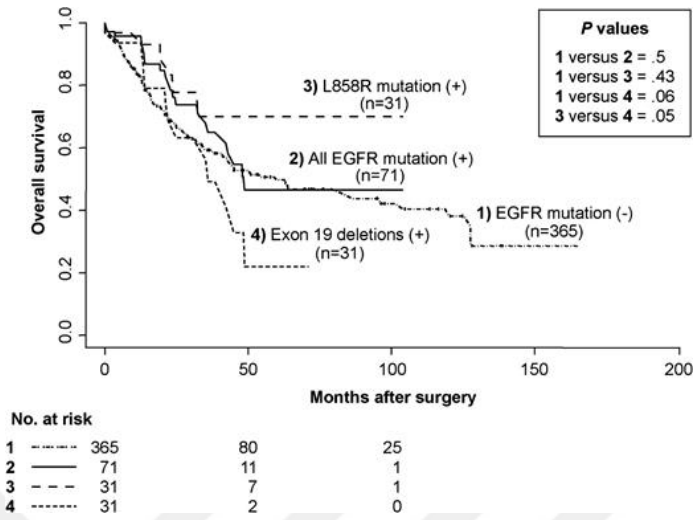

Figure 4: Kaplan–Meier survival graphs for non-small-cell lung cancer patients based on the EGFR mutation status (48).

2.4. EGFR Tyrosine Kinase Inhibitors (EGFR-TKIs)

Tyrosine kinase inhibitors (TKIs) are crucial targeted therapeutic agents in cancer treatment, disrupting the signal transduction pathways of protein kinases through various inhibition mechanisms (49). TKIs are categorized into three groups: receptor tyrosine kinases (RTKs), non-receptor tyrosine kinases (NRTKs), and dual-specificity kinases (DSKs), which include serine and threonine kinases (50). EGFR-TKIs, which target EGFR, belong to the RTK family. These small molecule inhibitors work by preventing the phosphorylation of downstream signaling pathways and inhibiting ligand-dependent EGFR dimerization in cells (51). EGFR-TKIs are further divided into two groups according to their binding dynamics (38). The first group consists of reversible inhibitors that forms covalent bonds with the ATP binding site of EGFR, competing with ATP through hydrophobic and electrostatic interactions. The second group consists of irreversible inhibitors that covalently bond with the ATP binding site, leading to permanent inhibition of EGFR activity (18,52).

The FDA approval of EGFR-TKIs marked a significant milestone in NSCLC treatment. The journey of EGFR-TKIs essentially began with the development of first-generation EGFR-TKIs (53). Gefitinib, Erlotinib, and Icotinib are notable examples of reversible first-generation inhibitors that have been approved by the FDA and are widely used in clinical practice (54–56). These inhibitors are designed to be mutation-selective, primarily targeting EGFR mutations, though they are also known to exert some inhibitory effects on wild-type EGFR (57).

Clinical studies have demonstrated that first-generation EGFR-TKIs can achieve promising progression-free survival rates (58–60). However, despite these positive outcomes, patients typically develop drug resistance after an average of 12–16 months of treatment (61). The most common resistance mechanism is the T790M secondary mutation in exon 20, observed in approximately 60% of NSCLC patients (38). This mutation causes a conformational change in the EGFR tyrosine kinase domain, leading to increased steric hindrance and competition between ATP and the inhibitor (62,63). Consequently, the binding affinity of EGFR-TKIs for the ATP binding site decreases (62). The T790M mutation is also known as a “gatekeeper mutation” because it serves as an escape mechanism to bypass inhibitor pressure (64), resulting in enhanced ATP binding and the activation of downstream signaling pathways (62).

Following the identification of resistance mechanisms against first-generation inhibitors, there was an urgent need for new therapeutic options (65). This led to the development of second-generation EGFR-TKIs. FDA-approved second-generation inhibitors, such as Afatinib and Dacomitinib, were specifically designed to address the EGFR-T790M mutation and offer improved efficacy for NSCLC patients (66,67). Dacomitinib is a pan-HER tyrosine kinase inhibitor targeting all members of the ErbB family (68), while Afatinib inhibits both EGFR and HER2 (69). These second-generation inhibitors not only target the T790M mutation but also address both EGFR-activating mutations and wild-type EGFR (70). Clinical studies have demonstrated that second-generation inhibitors exhibit

good efficacy. However, despite their promising results, these inhibitors have been associated with adverse side effects and dose intolerance, particularly in cases with T790M mutations, which limit their clinical applicability and frequency of use (71).

2.5. Third-Generation EGFR-TKIs – Osimertinib

The resistance observed with first- and second-generation EGFR-TKIs has underscored the need for newer generation inhibitors. The development of third-generation EGFR-TKIs has been informed by the resistance mechanisms identified in earlier inhibitors. These third-generation inhibitors, developed through library screening focused on kinase inhibitor core structures, feature a distinct structure from the quinazoline-based compounds of the first and second generations, binding irreversibly to the pyrimidine-based tyrosine kinase domain (72). Initially, nine different third-generation EGFR-TKIs were developed (73). Some of these inhibitors have been approved for clinical use, while others have either not succeeded in clinical trials or are still in the process of transitioning to clinical practice (74,75). Third-generation EGFR-TKIs are particularly effective against tumors with EGFR-activating mutations and are designed to overcome the T790M mutation. These mutant-selective inhibitors demonstrate significantly greater activity in cells with mutant EGFR compared to those with wild-type EGFR (76).

Osimertinib (AZD9291), developed by AstraZeneca and approved by the FDA in 2015 under the brand name Tagrisso, represents the first ever third-generation EGFR-TKI (77). It is the only EGFR-TKI approved by the FDA for both first-line treatment of patients with locally advanced or metastatic NSCLC with EGFR activating mutations and second-line treatment for those with the EGFR-T790M mutation (37,77). Osimertinib effectively addresses the T790M mutation by forming a strong covalent bond with the cysteine residue at position 797 in the ATP binding site of the tyrosine kinase domain (78). Additionally, osimertinib can target other resistance mechanisms associated with first-generation EGFR TKIs (77,79). According to a study by Cross et al. published in 2014,

osimertinib demonstrated high efficacy in cell lines with exon 19 deletion, L858R, and T790M mutations, with an IC50 of <15 nM. In contrast, its efficacy was significantly lower in cell lines with wild-type EGFR, where the IC50 ranged from 480 nM to 1865 nM (11,77). Therefore, osimertinib exhibits greater selectivity for mutant EGFR compared to both first- and second-generation EGFR-TKIs (37,80).

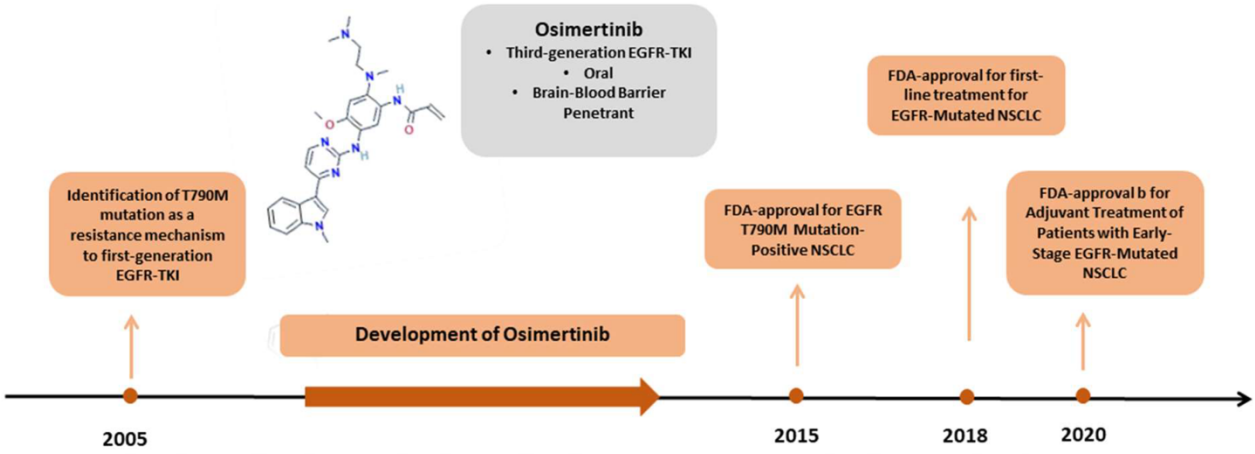

Figure 5: The timeline for the development of osimertinib (81).

Osimertinib is associated with less severe gastrointestinal and skin toxicity compared to first- and second-generation EGFR-TKIs, largely due to its high selectivity for mutant EGFR (79,82). Additionally, the superiority of osimertinib over prior generation EGFR-TKIs is showcased by its ability to penetrate the blood-brain barrier and affect the central nervous system (83). In the AURA3 clinical trial, osimertinib demonstrated a significant improvement in progression-free survival (PFS) in patients with the EGFR-T790M mutation, showing a PFS of 10.1 months compared to 4.4 months with platinum-pemetrexed treatment. This trial also revealed that osimertinib prolonged PFS in NSCLC patients with central nervous system metastases (Figure 5) (84). Following these findings, osimertinib was approved for treating patients with the T790M mutation. Further establishing its clinical advantage, the FLAURA3 trial, completed in 2018, showed that osimertinib provided superior overall survival compared to first-generation EGFR-TKIs

(Figure 5) (85). This evidence further supported the approval of osimertinib as a first-line treatment for EGFR-mutated NSCLC. Additionally, the ADAURA clinical trial demonstrated that adjuvant treatment with osimertinib in NSCLC patients whose tumors had been surgically removed improved PFS by extending the time to cancer recurrence (Figure 5) (86).

2.6. Osimertinib Resistance Mechanisms

Despite its potent efficacy in treating NSCLC, acquired resistance to osimertinib is an inevitable challenge. Resistance mechanisms to osimertinib are generally classified into two categories: EGFR-dependent and EGFR-independent.

2.6.1. EGFR-dependent Osimertinib Resistance Mechanisms

EGFR-dependent resistance mechanisms involve defects or abnormalities in EGFR itself, such as missense mutations, amino acid substitutions, insertions, gene amplifications, and back mutations. The most prevalent of these is the C797X mutation, found in approximately 40% of resistant cases, which represents an escape mechanism from osimertinib pressure (87). This mutation involves a substitution of the cysteine residue at codon 797 in exon 20, which disrupts the covalent interaction between osimertinib and the ATP binding site, thereby reducing the drug's ability to inhibit EGFR (80,88,89). Other atypical mutations, including G719A, L792X, G796X, and G724S, create steric hindrance that interfere with osimertinib binding. EGFR gene amplification is another identified mechanism of resistance, as it can increase the amount of EGFR available for binding and contribute to resistance (87,90,91). Additionally, since osimertinib targets the T790M mutation specifically, the loss of this mutation, or back mutation, during tumor evolution is considered a strategy to evade the drug's effects (87). A study of 143 patients published in 2018 found that loss of T790M indeed often occurs in conjunction with other resistance mechanisms in patients who do not respond to osimertinib (87,92).

2.6.2. EGFR-independent Osimertinib Resistance Mechanisms

EGFR-independent osimertinib resistance mechanisms include histological transformations, epithelial-to-mesenchymal transition, and aberrant activation of bypass signaling pathways and downstream pathways (11,37). The most well-known mechanisms are MET gene amplifications, HER2 alterations, oncogenic fusions with ALK and RET genes, aberrant FGFR, IGF1R and AXL signaling, small-cell transformation and epithelial and mesenchymal transitions (11,87).

3. MATERIALS AND METHODS

3.1. Type of the Research

This research study is descriptive and experimental.

3.2. Place and Time of the Research

The study was conducted in Senturk Functional Cancer Genomics Laboratory at Izmir Biomedicine and Genome Center between January 2022 and July 2024.

3.3. Research Material

3.3.1. Cell Lines and Cell Culture Consumables

H1975 cell line was kindly gifted from Prof. Dr. Stefan Dimitrov. PC9 cell line was kindly gifted from Prof. Dr. Tamer Yağcı (Gebze Technical University, Turkey). HEK293T Cell Line was kindly provided by Prof. Dr. Nuri Öztürk (Department of Molecular Biology and Genetics, Gebze Technical University). Cell culture consumables that were utilized in this study are detailed in Table 1. Additionally, other consumables including cell culture dishes, plates, falcon tubes, serological pipettes were purchased from suppliers such as Sarstedt, Greiner, SPL and Cornomics Life Sciences.

Table 1: List of cell culture consumables.

Product Name	Catalog #	Vendor
RPMI-1640	21875034	Gibco
DMEM, high glucose	41965039	Gibco
Fetal Bovine Serum (FBS)	10500-064	Gibco
Penicilin-Streptomycin (10,000 U/ml) (P/S)	15140-122	Thermo Fisher
Phosphate-buffered Saline (PBS) pH 7.4 (10X)	70011036	Gibco
DMSO	PA.A3672.0250	Panreac Applichem
0.25% Trypsin-EDTA (1X), phenol red	25200-056	Gibco
Hexadimethrine bromide (Polybrene)	H9268-5G	Sigma
PEI	23966	Polyscience
Blasticidin	ant-bl-05	Invivogen

3.3.2. PCR Reagents

Conventional Polymerase Chain Reaction (PCR), colony PCR, quantitative reverse transcription PCR (qRT-PCR) and cDNA synthesis reagents that were utilized in this study are detailed in Table 2.

Table 2: List of PCR and cDNA synthesis reagents.

Product Name	Catalog #	Vendor
DreamTaq™ Hot Start DNA Polymerase	EP1701	Thermo Scientific

10X DreamTaq Buffer		
dNTP Solution mix (10 mM each dNTP)	N0447S	NEB
Q5 High-Fidelity DNA Polymerase	M0491S	NEB
Q5 Reaction Buffer	B9027S	NEB
iScript™ cDNA Synthesis Kit	1708891	Biorad
BlasTaq Green 2X qPCR Master mix (w/ROX)	G892	ABM

3.3.3. Primers

Primers that were used in conventional PCR and qRT-PCR are shown in Table 3 and Table 4 respectively.

Table 3: Primer sequences that are used in conventional PCR.

Gene Name	Sequence (5'-3')
EGFR Exon 19_F	AGCATGTGGCACCATCTCAC
EGFR Exon 19_R	ATGAGAAAAGGTGGGCCTGA
EGFR Exon 20_F	AGCCACACTGACGTGCCTCT
EGFR Exon 20_R	CCTTATCTCCCCTCCCCGTA
EGFR Exon 21_F	TGCAGAGCTTCTTCCCATGA
EGFR Exon 21_R	GCATGTGTTAAACAATACAGC
EGFR Exon19_Intron18_F	CCAGATCACTGGGCAGCATGTGGCACC
EGFR Exon19_Intron19_R	AGCAGGGTCTAGAGCAGAGCAGCTGCC
EGFR_ Exon19_Intron19_Nested_R	TGGACCCCCACACAGC
EGFR WT_F	CCGTCGCTATCAAGGAATTAAG
EGFR Mutant_F	TCCCGTCGCTATCAAAACATC

EGFR WT_Mutant_F	ATGTGGCACCATCTCACAATTGCC
EGFR_R	CCACACAGCAAAGCAGAAACTCAC
hU6_F	GAGGGCCTATTTCCCATGATT

Table 4: Primer sequences that are used in qRT-PCR.

Gene Name	Sequence (5'-3')
CDH1_F	CGAGAGCTACACGTTCACGG
CDH1_R	GGCCTTTTGACTGTAATCACACC
VIM_F	CGTCACCTTCGTGAATACCA
VIM_R	CCAGAGGGAGTGAATCCAGA
GAPDH_F	GGCTGAGAACGGGAAGCTTGTCAT
GAPDH_R	CAGCCTTCTCCATGGTGGTGAAGA

3.3.4. Oligonucleotides

Oligonucleotides that were used in CRISPR/Cas9 knockout experiments are shown in Table 5. Renilla luciferase gene that is not present in human genome, was utilized as a negative (non-targeting) control.

Table 5: gRNA sequences that are used in CRISPR/Cas9 knockout.

Gene Name	Sequence (5'-3')
EGFR g10_F	GCTGCCCCGGCCGTCCCGGA
EGFR g10_R	TCCGGGACGGCCGGGGCAGC
EGFR g60_F	TCCTCCAGAGCCCGACTCGC

EGFR g60_R	GCGAGTCGGGCTCTGGAGGA
Renilla_F	GGTATAATACACCGCGCTAC
Renilla_R	GTAGCGCGGTGTATTATACC

3.3.5. Plasmids

gRNA sequences were cloned into the lentiviral backbone called lentiCRISPR v2-Blast (LCV2-Blast) (Addgene, #83480), the map and the restriction sites of which are detailed below in Figure 8. In addition, helper plasmids' (psPAX2 (Addgene, #12260) and pMD2.G (Addgene, #12259)) maps which were used in virus production are given below in Figure 6 and 7.

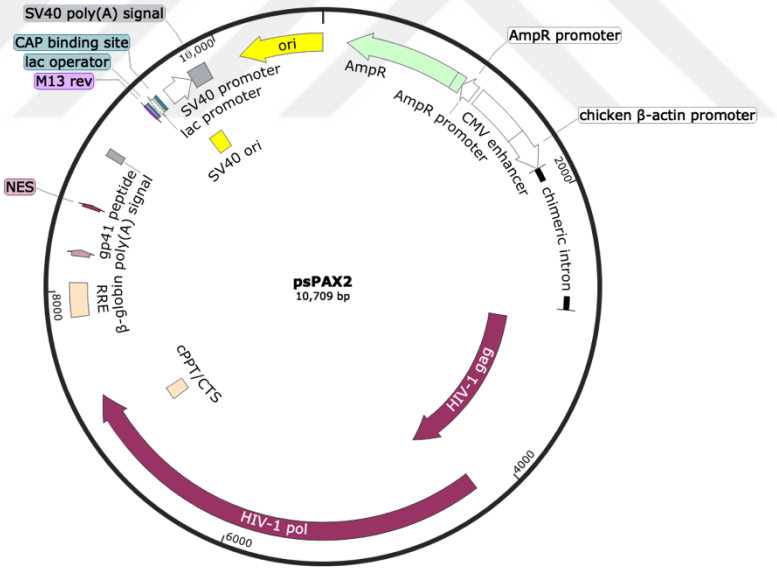

Figure 6: psPAX2 plasmid map. (Obtained from Addgene, visualized using SnapGene software)

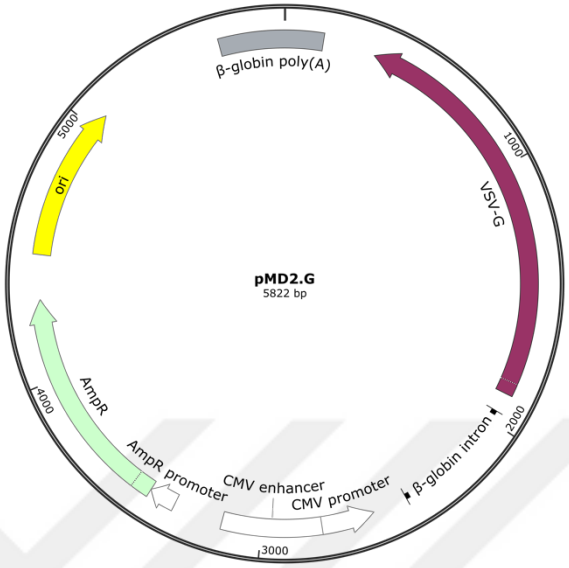

Figure 7: pMD2.G plasmid map. (Obtained from Addgene, visualized using SnapGene software)

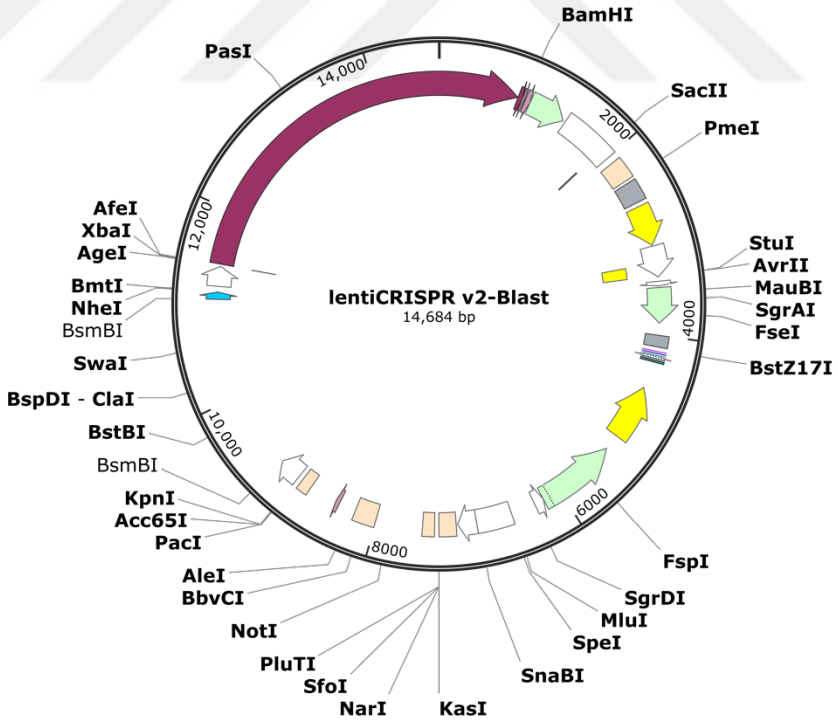

Figure 8: lentiCRISPR v2-Blast plasmid map. (Obtained from Addgene, visualized using SnapGene software)

3.3.6. Enzymes and Buffers for Molecular Cloning

Molecular cloning reagents that were utilized in this study are detailed in Table 6.

Table 6: List of reagents used for molecular cloning.

Product Name	Catalog #	Vendor
FastDigest BsmBI	FD0454	Thermo Scientific
10X FastDigest Buffer		
Fast AP (Alkalyne phosphatase)	EF0651	Thermo Scientific
10X T4 ligation buffer	B0202L	NEB
T4 Polynucleotide Kinase (3' phosphate minus)	M0236L	NEB
T4 DNA ligase	M0202L	NEB

3.3.7. Bacterial Strain and Reagents

The bacterial strain used and required reagents for the bacterial transformation step in molecular cloning experiments are listed in Table 7.

Table 7: List of reagents used for bacterial transformation.

Product Name	Catalog #	Vendor
One ShotTM Stbl3TM Chemically Competent Cells	737303	Thermo Scientific
Yeast Extract	MB16401	Nzytech
LB Broth with Agar	L2897	Sigma
Tryptone	1553.03	AppliChem
Ampicillin	A0166	Sigma
NaCl	M106404.1000	Merck

3.3.8. Conventional Genomic DNA Isolation Reagents and Buffer Recipe

The reagents necessary for Genomic DNA isolation buffer and its recipe are detailed in Table 8 and Table 9, respectively.

Table 8: List of reagents used for preparing conventional genomic DNA isolation buffer.

Product Name	Catalog #	Vendor
Tris	T1503-1KG	Sigma Aldrich
EDTA	E5134-500G	Sigma Aldrich
SDS	8170341000	Merck
RNase A	1263MG050	Neofroxx
Monarch Proteinase K	T2002	NEB

Table 9: DNA lysis buffer recipe.

Reagent Name	Stock Concentration	Working Concentration	Volume
Tris-Cl pH 8	0.8 M	10 mM	312.5 µL
EDTA pH 8	0.5 M	0.1 M	5 mL
SDS	125 mg	0.5%	25 µL
Proteinase K	20 mg/mL	100 µg/mL	250 µL
RNase A	50 mg/mL	20 µg/mL	150 µL
dH_2O			Up to 25 mL

3.3.9. Western Blot Reagents, Buffer Recipes, and Antibodies

In this study, proteins were isolated using a modified Radioimmunoprecipitation Assay (RIPA) buffer with detailed reagents and recipes provided in Tables X and X, respectively.

Table 10: List of RIPA buffer reagents.

Product Name	Catalog #	Vendor
EDTA	E5134-500G	Sigma Aldrich
EGTA	E3889-10G	Sigma Aldrich
SDS	8170341000	Merck
Tris	T1503-1KG	Sigma Aldrich
PMSF	LSG36978-5G	Sigma Aldrich
Triton X-100	T8787-100ml	Sigma Aldrich
Leupeptin	1273-25mg	Neofroxx
Aprotinin	1278-25mg	Neofroxx
Pepstatin	P5318-5MG	Sigma Aldrich
β-glycerolphosphate	50020-100G	Sigma Aldrich
Na deoxycholate	30970-25G	Sigma Aldrich
NaF	S6776-100G	Sigma Aldrich

Table 11: RIPA buffer recipe.

Reagent	Stock Concentration	Working Concentration	Volume
EDTA pH 8	0.5 M	1 mM	50 µL

EGTA	0.1 M	1 mM	50 µL
SDS	20%	0.1% (mild)	25 µL
Tris-Cl pH 7.4	1 M	50 mM	250 µL
PMSF	0.1 M	1 mM	50 µL
Triton X-100	10%	1%	500 µL
Leupeptin	5 mg/mL	10 µg/mL	10 µL
Aprotinin	5 mg/mL	10 µg/mL	10 µL
Pepstatin	1 mg/mL	10 µg/mL	50 µL
β-glycerolphosphate	0.5 M	10 mM	100 µL
Na deoxycholate	10%	0.5%	250 µL
NaF	0.5 M	10 mM	200 µL
Na Vanadate	0.1 M	1 mM	50 µL
NaCl	5 M	150 mM	150 µL
dH_2O			Up to 5 mL

In this study, proteins are separated using SDS-PAGE gel electrophoresis, with the compositions of the separating and stacking gels, along with the corresponding reagents, detailed in Tables 12, 13, and 14, respectively.

Table 12: List of reagents for SDS-PAGE gel.

Product Name	Catalog #	Vendor
Protogel (30%)	EC-890	National Diagnostics
Protogel stacking buffer	EC-893	National Diagnostics

APS	1610GR100	BioFroxx
TEMED	T22500-100	Sigma Aldrich

Table 13: Separating gel recipe.

Component	6%	8%	10%	12%	15%
Protogel (mL)	1	1.35	1.65	2	2.5
dH_2O (mL)	3.375	3.025	2.725	2.375	1.875
Main gel buffer (mL)	0.625				
10% APS (µL)	25				
TEMED (µL)	5				

Table 14: Stacking gel recipe.

Component	2 ml	3 ml	4 ml	5 ml	6 ml	7 ml	8 ml	9 ml	10 ml
Protogel (mL)	0.25	0.375	0.5	0.625	0.75	0.875	1	1.125	1.25
dH_2O (mL)	1.25	1.875	2.5	3.125	3.75	4.375	5	5.625	6.25
Protogel stacking buffer	0.5	0.75	1	1.25	1.5	1.75	2	2.25	2.5
10% APS (µL)	12.5	18.75	25	31.25	37.5	43.75	50	56.25	62.5
TEMED (µL)	2.5	3.75	5	6.25	7.5	8.75	10	11.25	12.5

Buffer recipes, reagents and consumables that are required for western blot are outlined in Table 15 and 16.

Table 15: Buffer recipes that are used in western blot.

Buffer Name	Component	Amount
Main gel buffer	Tris	72.684 g
	SDS 10%	16 mL
	dH_2O	Up to 200 mL
	pH	8.8
Running buffer (10X)	Tris	250 mM
	SDS	1%
	Glycine	1.9 M
	dH_2O	Up to 1 L
	pH	~8.3
Transfer buffer (10X)	Tris	250 mM
	Glycine	1.9 M
	dH_2O	Up to 1 L
	pH	~8.3
	Methanol	20%
TBS (10X)	Tris	24 g
	NaCl	88 g

	dH_2O	Up to 1 L
	pH	7.6

Table 16: Other reagents and consumables that are used in western blot.

Product	Catalog #	Vendor
BLUeye Prestained Protein Ladder	PM007-0500	GeneDirex
Skim Milk Powder	70166-500G	Sigma Aldrich
Albumin Fraction V (pH 7.0)	1126GR100	BioFroxx
Tween-20	BP337-100	Fisher BioReagents
Ponceau S	P3504-10G	Sigma Aldrich
Acetic acid	27225-2.5L-R	Sigma Aldrich
Nitrocellulose membrane (0.2 µL)	GE10600004	GE Healthcare

Antibodies used in this study along with their working dilutions, are detailed in Table 17.

Table 17: List of antibodies and their working dilutions.

Product Name	Working Dilution	Catalog #	Vendor
EGF Receptor (D38B1) XP (R) Rabbit mAb	1/1000	4267T	Cell Signaling Technology
Phospho-EGF Receptor (Tyr1068) pAb	1/1000	2234	Cell Signaling Technology

p44/42 MAPK (Erk1/2) (137F5) Rabbit mAb	1/1000	4695T	Cell Signaling Technology
p-p44/42 MAPK XP (R) Rabbit mAb	1/1000	4370T	Cell Signaling Technology
E-Cadherin (24E10) Rabbit mAb	1/1000	3195	Cell Signaling Technology
Vimentin (D21H3) XP® Rabbit mAb	1/1000	5741	Cell Signaling Technology
Stat3 (79D7) Rabbit mAb	1/1000	4904T	Cell Signaling Technology
Phospho-Stat3 (Tyr705) (D3A7) XP® Rabbit mAb	1/1000	9145T	Cell Signaling Technology
AKT (C67E7) Rabbit mAb	1/1000	4691T	Cell Signaling Technology
p-AKT (S473) XP (R) Rabbit mAb	1/1000	4060T	Cell Signaling Technology
β-Actin (8H10D10) Mouse mAb	1/1000	3700S	Cell Signaling Technology
α-Tubulin (DMIA) Mouse monoclonal IgG1	1/1000	SC-32293	SantaCruz
Anti-mouse IgG (H+L) (DyLightTM 680 Conjugate)	1/10000	5470P	Cell Signaling Technology
Anti-rabbit IgG (H+L) (DyLightTM 800 4X PEG Conjugate)	1/20000	5151P	Cell Signaling Technology

3.3.10. Bromodeoxyuridine (BrdU) Incorporation Assay Reagents

Antibodies and reagents that were utilized in the BrdU assay are outlined in Table 18.

Table 18: List of reagents and antibodies used in BrdU assay.

Product Name	Cat #	Vendor
Absolute Ethanol	920.026	ISOLAB
Hydrocloric acid fuming 37%	1003172500	Merck
DAPI for mb	28718-90-3	Neofroxx
5'-Bromo-2'-deoxyuridine	B5002	Sigma
BrdU (Bu20a) Mouse mAb	5292	Cell Signaling Technology
Dnk pAb to Ms IgG AlexaFluor 488	ab150105	Abcam
Microscope Cover Glasses 12 mm	111520	Marienfield

3.3.11. Immunofluorescence (IF) Staining Reagents

Antibodies that were utilized in the IF staining are outlined in Table 19 with their working dilutions.

Table 19: List of antibodies used in the IF assay and their corresponding working dilutions.

Product Name	Working Dilution	Cat #	Vendor
Vimentin (D21H3) XP® Rabbit mAb)	1/200	5741	Cell Signaling Technology
Purified Mouse Anti-E-cadherin	1/200	610181	BD Transduction Laboratories™
Alexa Fluor™ 647 Phalloidin	1/200	A22287	Invitrogen

Dnk pAb to Ms IgG Alexa Fluor 488	1/500	ab150105	Abcam
Dnk pAb to Rb IgG Alexa Fluor 568	1/500	ab175470	Abcam

3.3.12. Other Chemicals, Consumables and Commercial Kits

The consumables, kits, and chemicals utilized in the experiments are listed in Table 20 below.

Table 20: List of chemicals, consumables and kits used in the study.

Product Name	Catalog #	Vendor
Formaldehyde solution	F1635	Honeywell
Crystal Violet powder	S6158	Sigma
Methanol	32213	Sigma
Matrigel® Basement Membrane Matrix, LDEV-free, 5 mL	356234	Corning
SPLInsert™ Hanging	35212	SPL
Propidium Iodide	81845	Sigma
Gel Loading Dye, Purple (6X)	B7024S	NEB
1 kb DNA Ladder	N3232S	New England Biolabs
100 bp DNA Ladder	G193	ABM
Thiazoly blue tetrazolium bromide (MTT)	1334GR001	Neofroxx
Noble Agar, Ultrapure, Thermo Scientific	10907-100gr	Alfa Aesar

NucleoSpin Gel and PCR Clean-up	740609.50	Macherey-Nagel
NucleoSpin Plasmid, Mini kit for plasmid DNA	740588.50	Macherey-Nagel
Monarch Total RNA Miniprep Kit	T2010S	NEB
EZ-10 Spin Column Genomic DNA Minipreps Kit (blood)	SK8253	Biobasic
Ultrapure Distilled Water 500 ml	10977-035	Invitrogen
5 ml Polystyrene Round Bottom Tube	352055	Falcon
28 mm Syringe Filter 0,45 µm SFCA membrane (sterile)	431220	Corning
Mycoplasma PCR Detection Kit	G238	Abm
Dacomitinib	PZ0330	Sigma
Erlotinib	SML2156	Sigma
Paclitaxel	S1150	Selleckchem

3.3.13. Devices and Softwares

Devices and softwares that were utilized in the study are detailed in Table 21.

Table 21: List of devices and softwares.

Device/Software Name	Vendor
BD LSRFortessa™ flow cytometer	BD Biosciences
FlowJo v10.8.0 software	BD Biosciences

CKX41 Inverted microscope	Olympus
BX61 Fully Motorized Fluorescence Microscope	Olympus
ImageJ 1.53k software	NIH
GraphPad Prism 8.0 software	Dotmatics
Multiskan™ GO Microplate Spectrophotometer	Thermo Fisher
LI-COR Odyssey Imaging System	LI-COR Biosciences
Nanodrop 2000	Thermo Fisher
pH Meter	Hanna Instruments
MicroCL 17 Microcentrifuge (Ventilated) 230V with Hematocrit rotor	Thermo Fisher
Toploader Balance 820 g x 0.01g	Sartorius
SimpliAmp™ Thermal Cycler	Applied Biosystems
OwlTM EasyCast™ B1A Mini Gel Electrophoresis Systems	Thermo Fisher
mySPIN™ 6 Mini Benchtop Centrifuge	Thermo Fisher
Incubator MaxQ 4000	Thermo Fisher
Confocal Microscopy LSM880	Zeiss
Gel Doc XR+ System with Image Lab Software	BioRad
Centrifuge 5810R	Eppendorf
ABI 7500 Fast Thermal Cycler	Thermo Fisher
SnapGene	Dotmatics

3.4. Methods

3.4.1. Cell Culture

All cells, except HEK293T, were cultured in RPMI-1640 medium containing 10% FBS and %1 P/S and maintained in incubator at 37°C with 5% CO_2. HEK293T was cultured in DMEM medium containing 10% FBS and %1 P/S and maintained in incubator at 37°C with 5% CO_2. Cells were regularly screened for negative mycoplasma with Mycoplasma PCR Detection Kit.

3.4.2. Generation of Resistant Cell Line

Osimertinib-resistant cell lines named PC9-OsiR and H1975-OsiR were established using the dose-escalation method. Cells were seeded to 10 cm cell culture dishes as $1x10^6$ cells per dish. The day after seeding, osimertinib exposure was started at sub-IC50 dose (for PC9: 1 nM; for H1975: 2 nM). After 3 days of osimertinib exposure cells passaged and seeded with drug-free medium to promote survival. This recovery period lasted for 3-4 days according to the cells' response to osimertinib. The dose of osimertinib was doubled for each iterative cycle of treatment. Between each osimertinib exposure, cells were cultured with drug-free medium as well. Osimertinib dose escalation cycle continued until the final dose has reached to 1.5 μM. After reaching the final dose, cells were cultured with 1.5 μM of osimertinib continuously for one more month. Following this period, osimertinib exposure ended and cells were cultured with drug-free medium for additional two weeks. The whole generation process lasted approximately six months. While culturing of resistant cells, cells were treated with drug solvent DMSO in another dish as a control group (PC9-Veh and H1975-Veh) and cultured continuously.

3.4.3. Calculating IC50 Dose

To determine the IC50 doses against different small molecule inhibitors (osimertinib, Dacomitinib, Erlotinib) and chemotherapeutic drug (Paclitaxel) MTT (3-(4, 5-

dimethylthiazolyl-2)-2, 5-diphenyltetrazolium bromide) assay and cell viability assay with crystal violet staining were utilized.

3.4.3.1. MTT Assay

IC50 doses against Osimertinib was calculated using MTT rapid colorimetric assay, which assesses cellular viability based on live cells' mitochondria activity (93). Cells were seeded to 96-well cell culture plates as six replicates and as 1000 cells/well in 100 µL. The day after seeding, cells were treated with osimertinib at 100 µL per well at predefined dose ranges for 72 hours. As drug control, inhibitor solvent was used, and its dilution was made equal to the highest dose inhibitor concentration. After 72 hours of inhibitor exposure, medium was removed and 200 µL of MTT solution (5 mg/mL in 1X PBS, final concentration: 0.5 mg/mL in medium) was added to the cells. After 4 hours of incubation at 37°C, MTT solution containing medium were aspirated. 100 µL DMSO added to each well to dissolve formazan crystals and plates were shaken using orbital shaker with 100-120 rpm for 30 minutes. The absorbances of dissolved formazan crystals at 570 and 720 nm were measured using a Multiskan GO Microplate Spectrophotometer and subsequent analyses were carried out according to these measurements. For blank absorbance subtraction, medium was added to separate wells without cells as triplicates and the entire MTT assay procedure and analysis were applied to these wells as well.

3.4.3.2. Cell Viability Assay with Crystal Violet Staining

IC50 doses against other generation EGFR-TKIs (Dacomitinib and Erlotinib) and Paclitaxel were calculated using crystal violet staining, which assesses cellular viability based on indirect quantification of cell death (94). Cells were seeded to 96-well cell culture plates as six replicates and as 1000 cells/well in 100 µL. The day after seeding, cells were treated with drugs at 100 µL per well at predefined dose ranges for 72 hours. As drug control, the inhibitor's solvent was used, and its dilution was made equal to the highest dose inhibitor concentration. After 72 hours of inhibitor exposure, the medium was

removed, and cells were washed 1X PBS. Then, cells were fixed by adding 75 µL of 3.7% formaldehyde solution to each well and incubating for 20 minutes. Following the incubation, cells were washed with 1X PBS again. Crystal violet staining was performed by adding 100 µL of 0.1% crystal violet (dissolved in 10% ethanol) to each well and incubating the plates for 40 min in the dark. After staining, the plates were rinsed with tap water and left to dry overnight. The plates were scanned LI-COR Odyssey CLx Imaging System (LI-COR Biosciences), and analysis was performed using LI-COR Image Studio and/or ImageJ software. For background subtraction, empty wells were stained and scanned as well.

3.4.4. Construction of gRNA Vectors

A multi-step molecular cloning protocol was followed to construct gRNA vectors. First, the backbone plasmid (LCV2-Blast) was digested and dephosphorylated with the protocol detailed in Table 22.

Table 22: Digestion and dephosphorylation protocol

Component Name	Volume
Backbone plasmid	5 µg
FastDigest BsmBI	3 µL
Fast AP	3 µL
10X FastDigest Buffer	6 µL
dH_2O	Up to 50 µL

Thermal cycler Steps
Incubate at 37°C for 2 hours

Digested product was loaded onto a 0.8% agarose gel and run for 1 hr at 100 V. Digested plasmid was isolated from the gel by the NucleoSpin Gel and PCR Clean-up kit according to manufacturer's protocol.

After acquiring the digested plasmid, to phosphorylate and anneal each pair of oligos reactions were carried out as described in Table 23 to prepare the gRNA sequences for the ligation step.

Table 23 Phosphorylation and anneal protocol for oligo pairs.

Component Name	Volume	Thermal cycler Steps
Oligo_F (100 µM)	1 µL	37°C for 2 hours
Oligo_R (100 µM)	1 µL	95°C for 5min and ramp down to 25°C at 5°C/min
10X T4 ligation buffer	1 µL	
T4 PNK	0.5 µL	
dH_2O	Up to 10 µL	

Annealed oligoduplexes were diluted 1:20 in dH_2O. The reaction for ligation of oligo duplexes and digested backbone was performed as detailed in Table 24.

Table 24: Ligation protocol

Component Name	Volume	Thermal cycler Steps
Digested plasmid	50 ng	Incubate at 25°C for 2 hours
Oligoduplex	2 µL	
10X T4 ligation buffer	1 µL	
T4 ligase	0.5 µL	
dH_2O	Up to10 µL	

For the amplification of ligated product, bacterial transformation was performed. First, bacteria aliquot was split into 25 µl for each sample. Sample resulting from the ligation was transferred into the bacteria. Then the mix was put on ice for 30 min. After incubation on ice, mix incubated at 42°C for 1 min. Immediately, mix was put on ice for 2 min. Then 950 µl LB was added to mix and incubated at 37°C for 1 hr. Following the incubation, mix was centrifuged at 11000 rpm for 1 min and the pellet was spread to agar plate supplemented with Ampicillin. Finally, the plate was incubated at 37°C for 16 hrs.

For vector verification, colony PCR were set up as detailed in Table 25. Then the resulting product was run on 2% agarose gel at 100 V for 1 hr.

Table 25: Colony PCR protocol

Component Name	Volume
DreamTaq Buffer	1 µL
dNTP	0.2 µL
Forward Primer (hU6_F)	0.4 µL
Reverse Primer	0.4 µL
DreamTaq DNA Polymerase	0.05 µL
dH_2O	Up to 10 µL

Thermal cycler Steps		
Initial Denaturation	5 min at 94°C	1 cycle
Denaturation	30 sec at 94°C	30 cycles
Annealing	30 sec at 60°C	
Extension	2 min at 72°C	
Final Extension	5 min at 72°C	1 cycle

After verification by colony PCR, positive colonies carrying the plasmid of interest were grown in a mini culture by adding colonies to 5 mL of LB medium supplemented with

ampicillin for 18-20 hrs at 37°C and 225 rpm. Finally, plasmids were isolated using the NucleoSpin Plasmid Mini Kit (Macherey-Nagel) according to the manufacturer's protocol.

3.4.5. Virus Production

For transient transfection, HEK293T cells were seeded at $1x10^6$ cells/well. Following the day of seeding, transfection was performed. Helper and target vectors were mixed in a 1:2:4 (pMD2.G:psPAX2:Target) ratio in 1X PBS. Separately, in another tube, a PEI and 1X PBS mixture were prepared in a 1:5 ratio. The DNA and PEI mixtures were then combined and vortexed vigorously. After vortexing, the mixture was incubated at room temperature for 30 min. Following the incubation, HEK293T cells were washed with 1X PBS, and 1.3 mL of DMEM was added. The PEI-DNA mixture was then added to the plate drop by drop in a counterclockwise direction, and the plate was rotated clockwise to distribute the transfection mix evenly. After 48 hrs of incubation, the medium from the HEK293T cells was collected and filtered through a 0.45 µm SFCA filter into a 1.5 mL microcentrifuge tube. The viruses were stored at -80°C.

3.4.6. Infection

250,000 cells/well for PC9-Veh and PC9-OsiR, 300,000 cells/well for H1975-Veh and H1975-OsiR were seeded to 6-well plates. After the virus was diluted 1:10 in the medium, polybrene transduction (main stock: 8 mg/mL) enhancer was added to the same medium to give a final concentration of 8 µg. The medium containing virus and polybrene was added to the cells to be infected. For the negative control, a well that was not infected was cultured. The cells were exposed to the virus for 48 hours. At the end of 48 hours, the cells were washed twice with 1X PBS, and the cells were trypsinized and transferred to a 10 cm cell culture dish. The day after seeding, selection medium containing 10 µg/mL Blasticidin was added to the PC9-Veh, PC9-OsiR and H1975-Veh groups and 20 µg/mL Blasticidin was added to the H1975-OsiR group. After 72 hours, the selection medium was

removed, and complete medium was added. The resulting Blasticidin-resistant cells (knockout clones) were cultured.

3.4.7. DNA Isolation

Cells were collected by trypsinization and then centrifuged at 1500 rpm for 2.5 min. The supernatant was aspirated and the pellets either were stored at -80°C or processed immediately for DNA isolation using EZ-10 Spin Column Genomic DNA Minipreps Kit (blood) according to the manufacturer's protocol. After elution, DNA concentration was measured by NanoDrop 2000 Spectrophotometer. Isolated DNAs were stored at -80°C.

3.4.8. Protein Isolation

Cell dishes were placed on ice and washed with ice-cold 1X PBS. After discarding the PBS, RIPA buffer was added to the cell dishes according to the cell confluency (60-100 µL). Cells were then scraped while on ice and transferred to chilled 1.5 mL microcentrifuge tubes. The tubes were incubated on ice for 30 min, vortexing every 10 min. Samples were centrifuged at 11000 g, at 4°C for 30 min. Following the centrifugation, the supernatants were transferred to new 1.5 mL microcentrifuge tubes and stored at -80°C.

3.4.9. Determination of Protein Concentration

The protein concentrations were determined using the Pierce™ BCA Protein Assay Kit. Albumin standards were serially diluted with RIPA from a starting concentration of 1000 ng/mL to a final concentration of 31.25 ng/mL, using a 1:2 dilution factor. Standards and samples were distributed as 2 µL to each well and in triplicate. 50 µL of the working reagent, made by mixing solution B and solution A in a 1:50 ratio, was added to each sample in the dark. After adding the working reagent, plate was incubated at 37°C for 30 min and absorbance was measured at 562 nm by Multiskan™ GO Microplate Spectrophotometer. With measured absorbances using the Varioskan software standard

curve was generated, and protein concentrations were determined. As blanks, wells that containing only RIPA buffer were used. Samples' concentrations that will be compared were adjusted to the same concentrations using RIPA buffer and each sample was mixed with 5X Laemmli buffer containing 30% β-Mercaptoethanol. The samples were then boiled at 95°C for 5 minutes.

3.4.10. SDS Gel Preparation

For western blot, SDS gel was prepared. After assembling the gel cast, the separating gel was prepared according to the recipe detailed in Table 10, based on the target protein's kDa. Once the gel was poured, 60% isopropanol was immediately added to ensure a flat surface. After 20 min, the isopropanol was removed and rinsed with dH_2O, and the western glasses were thoroughly dried with a napkin. Next, stacking gel was prepared according to the recipe detailed in Table 11 and poured onto glasses. The comb was then placed between the plates. After the stacking gel polymerized for 30 minutes, the comb was removed, and the running system was set up to run the samples.

3.4.11. Western Blot

Denatured protein samples were loaded into gel lanes as 20 µg. The protein ladder was prepared with 1X Laemmli buffer based on the volume of loaded samples. Loaded samples were run at 90V for 20-30 min as the protein left the stacking gel, and then the voltage was increased to 120V for separating the proteins. After electrophoresis, wet transfer to a nitrocellulose membrane with sandwich assembly was applied following the protocol (95). The transfer was performed at 350 mA for 90 min. Following the transfer, Ponceau S staining was performed to check the success of the transfer and to facilitate the membrane cutting. After staining, membranes were quickly rinsed with 1X TBS, and then for blocking, they were incubated in %5 milk powder (dissolved in 1X TBS) for 1 hour at room temperature by rocking at 20 rpm. After blocking, membranes were rinsed with 1X TBS-T. The primary antibody was prepared at dilution detailed in Table 17 in 1% BSA

and 1X TBS-T and incubated overnight at 4˚C by rocking at 20 rpm to detect the protein of interest. Following the primary antibody incubation, the membranes were washed with 1X TBS-T 3 times for 10 minutes by rocking at 50 rpm. Then, membranes were incubated in the dark with the proper host's secondary antibodies prepared at dilution detailed in Table 17 in 1% BSA and 1X TBS-T and incubated at room temperature for 1 hour. Finally, the membrane was washed three times with 1X TBS-T for 10 minutes by rocking at 50 rpm, and 1X TBS was added for storage and scanned at 700 and/or 800 channels LI-COR Odyssey CLx Imaging System (LI-COR Biosciences).

3.4.12. Bromodeoxyuridine (BrdU) Incorporation Assay

15,000 cells/well for PC9-Veh, 12,000 cells/well for PC9-OsiR, 15,000 cells/well for H1975-Veh, 15,000 cells/well for H1975-OsiR were seeded on 12 mm round glass slides in 24-well plates. The day after seeding, cells were treated with osimertinib at predefined doses for 48 hrs. After 48 hrs, for BrdU labeling, drug-containing medium was replaced with medium containing both drug and 30 μM BrdU and the cells were treated for additional 24 hrs. After 72 hrs osimertinib treatment, medium was aspirated, and cells were rinsed with 1X PBS. For fixation, 500 μL %70 ice-cold ethanol was added to each well while plate was on ice and incubated for 10 min. Then ethanol was removed and for DNA denaturation 500 μL 2N HCl added to each well and incubated for 30 min at room temperature. After HCl was discarded, slides were washed 3 times with 1X PBS-T for 5 min by orbital shaker at 100 rpm. BrdU monoclonal antibody was prepared in %1 BSA in 1X PBS-T with 1:1000 dilution. 15-20 μL antibody was added to slides carefully and incubated at room temperature for 2 hrs. After primary antibody incubation, slides were washed 3 times with 1X PBS-T for 5 min by orbital shaker at 100 rpm. For detection, anti-mouse Alexa Fluor 488 secondary antibody was prepared in %1 BSA in 1X PBS-T with 1:500 dilution. Secondary antibody added to each well and incubated for 1 hr at room temperature. Slides were washed 3 times with 1X PBS-T for 5 min by orbital shaker at 100 rpm. Lastly, slides were stained with DAPI for 1 min to counterstain nuclei. Coverslips were mounted onto glass slides. Slide images were taken by BX61 Fully Motorized

Fluorescence Microscope (Olympus). The percentage of proliferative cells was calculated as the number of BrdU labeled cells over the total number of DAPI-positive nuclei in at least 8 fields randomly counted in the microscope field (magnification, 200X).

3.4.13. Wound Healing Assay

Cells were seeded into 6-well plates the next day at approximately 90% confluence. The day after seeding, cells were treated with osimertinib for 24 h. After 24 h, since the cells were almost 100% confluent, a 200 µL pipette tip was used to create a straight-line scratch on the cell monolayer. After the cell monolayer was wounded, cells were carefully washed with 1X PBS, followed by replenishment of the cell medium with medium supplemented with 2% FBS. Wound scratches were visualized using a CKX41 Inverted microscope (Olympus) at time points T0, T24, and T48. Scratch areas were quantified using ImageJ 1.53e software with the Wound Healing Assay plugin.

3.4.14. Transwell Invasion Assay

Matrigel matrix, diluted 1:40 in serum-free medium, was added to boyden chambers in a final volume of 50 µl per well placed in 24-well plate. The plate containing boyden chambers was incubated for 2 hrs at 37°C. After incubation, the excessive medium was discarded carefully without disturbing the Matrigel matrix layer on the chamber membrane. Then cells were seeded as 50,000 cells/200 µL in duplicates in serum-free medium. The lower well was filled with 10% FBS supplemented medium, and cells were incubated for 48 hrs. After 48 hrs of incubation, medium was aspirated, and chambers were washed with 1X PBS twice. Then cells were fixed with 3.7% formaldehyde solution for 2 min. After fixation, chambers were washed with 1X PBS twice and permeabilized with 100% methanol incubation for 20 min. Lastly, chambers were washed with 1X PBS twice and then stained with 0.5% crystal violet for 15 min. After staining was completed, chambers were washed with 1X PBS twice. Non-invasive cells were scraped off with cotton swabs. Migrated cells were counted under CKX41 Inverted microscope (Olympus).

3.4.15. 2D Colony Formation Assay

Cells were seeded 1000 cells/well to 12-well plate or 1500 cells/well to 6-well plate in triplicates. Medium was replenished every 3-4 days during clonal growth for 10-12 days. If osimertinib application present in experiment setup, drug-containing medium applied continuously and replenished every 3-4 days as well. After clonal growth enough to finish the experiment, cells were washed with 1X PBS and fixed by incubating with 3.7% formaldehyde solution for 20 min. Then cells were washed with 1X PBS and stained with 0.5% crystal violet for 40 min. After staining, plates were thoroughly washed with tap water. High-resolution images of the plates were obtained by using the Odyssey CLx Imaging System (LI-COR) and signal intensities were quantified using ImageJ 1.53e software. For background subtraction, wells that did not have cells in them were stained with crystal violet and used as blank.

3.4.16. Cell Cycle Assay

70,000 cells/well for PC9-Veh and PC9-OsiR, 35,000 cells/well for H1975-Veh and H1975-OsiR were seeded to 6-well plates and the day after seeding, medium was replaced with osimertinib-containing medium in predefined concentrations. Cells were treated with osimertinib for 72 hrs. After treatment is done, cells were trypsinized and then centrifuged at 1500 rpm for 2.5 min. Then cells were resuspended with 1.5 mL cold 1X PBS and incubated on ice for 10 min. While the cells were vortexed briefly, 3.5 mL 100% ethanol was added drop by drop and let the cells fixed for 15 min on ice. Fixed cells were centrifuged at 1200 rpm for 15 min at 4°C and resuspend with 70 µL PI solution (50 µg/mL propidium iodide, 0.1 mg/mL RNase A and 0.05% Triton X-100 in 1X PBS) and incubated for 40 min at 37°C by briefly vortexing every 10 min. After PI staining is done, stained cells were centrifuged at 6000 rpm for 5 min at 4°C and transferred to polystyrene tubes in 100-200 µl cold 1X PBS and analyzed using BD LSRFortessa™ flow cytometer. Cell cycle phases were analyzed by using FlowJo v10.8.0 software. This experiment was performed three times, each as a biological replicate.

3.4.17. Immunofluorescence Staining Assay

70,000 cells/well for PC9-Veh, 50,000 cells/well for PC9-OsiR, 50,000 cells/well for H1975-Veh, 70,000 cells/well for H1975-OsiR were seeded on 12 mm round glass slides in 24-well plates. When the cells were reached to 60-65% confluency, medium was aspirated, and cells were rinsed with 1X PBS. For fixation, 500 µL 3.7% formaldehyde solution was added to each well and incubated for 10 min. Then formaldehyde solution was removed and for permeabilization, 0.5 % Triton-X100 added to each well and incubated for 5 min at room temperature with orbital shaking. After permeabilization, cells were washed three times with 1 X PBS for 5 min orbital shaking and blocked with 5% BSA in 1X PBS for 1 hr in room temperature. Following the blocking, the slides were rinsed with 1X PBS-T and the area around the slides was thoroughly dried to prevent the primary antibody from leaking into wells. Primary antibody was prepared in %1 BSA and 0.3% Triton X-100 in 1X PBS-T with working dilution detailed in Table 19. 15-20 µL antibody was added to slides carefully and incubated at room temperature for 1 hr. After primary antibody incubation, slides were washed 3 times with 1X PBS-T for 5 min by orbital shaker at 100 rpm. For detection, anti-mouse Alexa Fluor 488 or anti-rabbit Alexa Fluor 568 secondary antibody was prepared in %1 BSA and 0.3% Triton X-100 in 1X PBS-T with 1:500 dilution. Secondary antibody added to each well and incubated for 1 hr at room temperature. Slides were washed 3 times with 1X PBS-T for 5 min by orbital shaker at 100 rpm. Lastly, slides were stained with DAPI for 1 min to counterstain nuclei. Coverslips were mounted onto glass slides. Slide images were taken by Confocal Microscopy LSM880 (Zeiss).

3.4.18. RNA Isolation

Cells were trypsinized and collected into 1.5 mL microcentrifuge tubes and centrifuged at 1500 rpm for 2.5 minutes. After the supernatant was removed and rinsing the pellet with cold 1X PBS, the centrifugation step was repeated. RNA isolation was performed using the Monarch Total RNA Miniprep Kit according to the manufacturer's protocol. Isolated RNA concentrations were determined using NanoDrop Spectrophotometer.

For RNA sequencing, cells were seeded into separate 10 cm cell culture dishes, with three technical replicates per condition. After 3 days of culturing, RNA was isolated using the same procedure as described above and stored at -80°C.

3.4.19. cDNA Synthesis

cDNA synthesis was performed using iScript™ cDNA synthesis kit according to the manufacturer's protocol. For each reaction, protocol detailed in Table 26 performed. Samples were diluted 4.2X by nuclease-free water and stored at -20°C.

Table 26: cDNA synthesis reaction protocol

Component Name	Volume
iScript reaction mix (5X)	4 µL
iScript reverse transcriptase	1 µL
Nuclease-free water	Variable
RNA template	1 µg
Total	Up to 20 µL

Thermal cycler Steps	
Priming	5 min at 25°C
Reverse Transcription	20 min at 46°C
RT Inactivation	1 min at 95°C
Optional step	Hold at 4°C

3.4.20. Quantitative Real-Time PCR (qRT-PCR)

Reaction mixes were prepared using BlasTaq Green 2X qPCR Master mix (abm) kit according to the manufacturer's protocol as detailed in Table 27.

Table 27: qPCR reaction mix recipe for single sample.

Component Name	Volume
BlasTaq™ 2X qPCR MM	5 µL
Forward Primer (10 µM)	0.4 µL
Reverse Primer (10 µM)	0.4 µL
Template DNA (1 µg)	4.2 µL
ddH_2O	Up to 10 µL

The prepared reaction mixtures were loaded into the MicroAmp Fast 96 well Reaction Plate as triplicate technical replicates for each sample in the dark and then the reaction plate was centrifuged at max speed for 30 sec to reduce the reaction mixture to the bottom of the plate. The qRT-PCR experiment was performed using Applied Biosystems 7500 Real-Time PCR System. Relative gene expression of genes of interest to endogenous control (GAPDH) was calculated using the following equation.

$$\text{Relative gene expression} = 2^{-\Delta\Delta C_t}$$

3.4.21. Analysis of Global Transcriptomics Data

Paired-end raw sequencing data were obtained as fastq files from company that performed NGS. For analysis of global transcriptomics data multi-step pipeline was used. Quality control of raw RNA sequencing libraries was performed using FASTQC (v0.11.7) and low-quality reads and adapter sequences were removed from libraries using Cutadapt (v1.18) software (96). The remaining reads were analyzed using the current human reference genome (GRCh38) and annotation (version 34) data obtained from the Gencode database (97). In order to align the reads to the reference genome, the genome index was created with the subread software using `subread-buildindex` command and then the reads were aligned to the reference genome with this index and the

`subread-align -t 0 -T 28 -a gencode.v39.primary_assembly.annotation.gtf -i grch38-index -o ${file}.bam -r ./${file}_1.fastq.gz -R ./${file}_2.fastq.gz` command (98). In the determination of gene expression levels, gene-level expression data were measured with the featureCounts software using `featureCounts -p -T 4 -F -f -M -s 2 -a /gencode.v39.primary_assembly.annotation.gtf -t exon -g gene_id -o /${file}_counts.txt /${file}_.bam 2> /${file}_featurecounts.screen-output.log` command and converted to CPM (Counts per million) (99). Statistical significance of differences in gene expression levels between two groups was performed with the edgeR package (v3.24.3) in the R computing environment (v4.1.1) (100). CPM values were used in the visualization of gene expression data. The ggplot2 package in the R environment was used to visualize the expression data. Genes with statistically significant increases and decreases in gene expression levels were listed according to the adj-pvalue, and various visuals representing gene clusters showing significant changes were created.

3.4.21.1. Gene Set Enrichment Analysis

The gene expression list file (.gct) was generated using counts per million (CPM) values derived from RNA sequencing for each sample. Since there were 3 samples per group, the permutation type was set to gene set. As for GSEA (v4.2.3), a list of differentially expressed genes with phenotype labels “PC9” and “PC9-OsiR” (and “H1975” and “H1975-OsiR”) was loaded into the GSEA tool, and “false discovery rate” (FDR), nominal p-values (p), and “negative enrichment scores” (NES) were calculated after 1000 random permutations of the gene set. FDR<0.25 and p<0.05 were considered statistically significant. C2, C5 and Hallmarks gene sets were used as gene sets in GSEA (101).

3.5. Study Plan and Calendar

Plan	Date
Literature Search	January 2022 – March 2022
Generating osimertinib resistant PC9 cell line	March 2022 – September 2022
Characterizing osimertinib resistant PC9 cell line	September 2022 – January 2024
Generating osimertinib resistant H1975 cell line	September 2023 – February 2024
Characterizing osimertinib resistant H1975 cell line	February 2024 – July 2024

3.6. Data Evaluation

All statistical analysis were performed utilizing GraphPad Prism 8 software and R programming language. Student's t-test was applied for comparisons between two independent groups, while ANOVA was employed for comparing multiple groups. Significance was denoted as following: p-value < 0.05 (*), p-value < 0.01 (**), and p-value < 0.001 (***).

3.7. Limitations of the Study

Despite all our results being reproducible, resistant cells were not developed from a single-cell clone, so the resistance of the cells was dynamic. As resistant cells were passaged in culture, some response to the drug was observed, although not as much as in the sensitive state.

3.8. Ethics Committee Approval

This study was approved by the IBG Local Ethics Committee with protocol number 2022-043.

4. RESULTS

4.1. Generation of Osimertinib-resistant PC9 Cell Line

The PC9 cell line, characterized by an E746-A750 deletion (ex19del) in the EGFR gene, was the primary cell line used in this study to model osimertinib resistance. To determine the initial dose for resistance induction, the IC50 of osimertinib was calculated in the parental PC9 cell line. For this purpose, 2500 cells were seeded into a 96-well, and osimertinib was applied at doses ranging from 4 µM to 0.0002 µM with a 1:4 dilution factor. After 72 hrs of incubation with osimertinib, crystal violet staining was performed to measure cell viability relative to the control group, which was treated with DMSO. The IC50 of osimertinib, representing the dose that resulted in 50% inhibition of cell viability, was determined to be 0.5 nM (Figure 9).

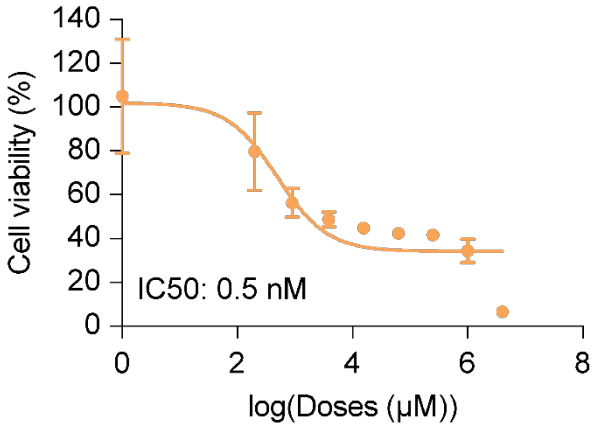

Figure 9: IC50 graph of osimertinib in PC9 (parental) cell line. The half-maximal inhibitory dose of osimertinib on PC9 was shown in the graph. (n=6, as technical replicates), calculated using GraphPad Prism 8 software, n=6.

The osimertinib-resistant PC9 clone, dubbed as PC9-OsiR, was developed using a dose escalation method, as outlined in the workflow shown in Figure 10. This method involved progressively increasing the concentration of osimertinib, thereby simulating the gradual acquisition of resistance typically observed in clinical settings. This dynamic and realistic model facilitates the development of cellular and molecular adaptations that occur as cells are exposed to increasing levels of the drug, effectively mimicking the resistance development process seen in patients (102).

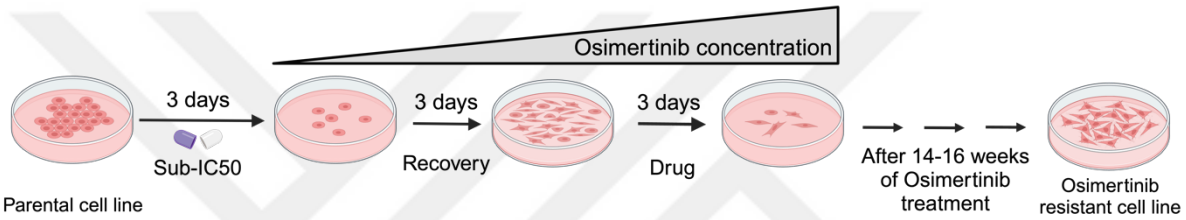

Figure 10: Schematic representation of the dose escalation method used in the development of osimertinib resistant cells. Created with BioRender.com

The process for developing osimertinib-resistant cells followed these general steps. Osimertinib treatment commenced with a sub-IC50 concentration. During the resistance development phase, cells were exposed to the inhibitor for up to 72 hours. Following this exposure, cells were cultured in drug-free medium for 3–4 days to allow the growth of surviving cells, though this period was adjusted based on cell viability. Osimertinib was then reapplied at twice the IC50 dose for 3 days, after which the cells were again cultured in drug-free medium. This cycle of drug administration was repeated, with each drug-free growth cycle involving a dose twice the previous dose, until a maximum concentration of 1.5 μM was reached. After achieving the 1.5 μM dose, cells were maintained continuously in 1.5 μM osimertinib for an additional month. The drug resistance development process took approximately 6 months. Of particular importance, PC9 cells were maintained in culture with DMSO vehicle (PC9-Veh) throughout the process,

Having successfully established an osimertinib-resistant clone with a polyclonal nature, we proceeded to characterize phenotypic and functional hallmarks of both treatment-naïve and osimertinib-resistant states. Notably, as the drug treatment progressed through cycles with increasing doses of osimertinib, phenotypic changes in the PC9 cells were observed. Compared to the control group (PC9-Veh), osimertinib-resistant cells displayed enlarged cytoplasm and alterations in membrane structure, including subtle cell protrusions (Figure 11).

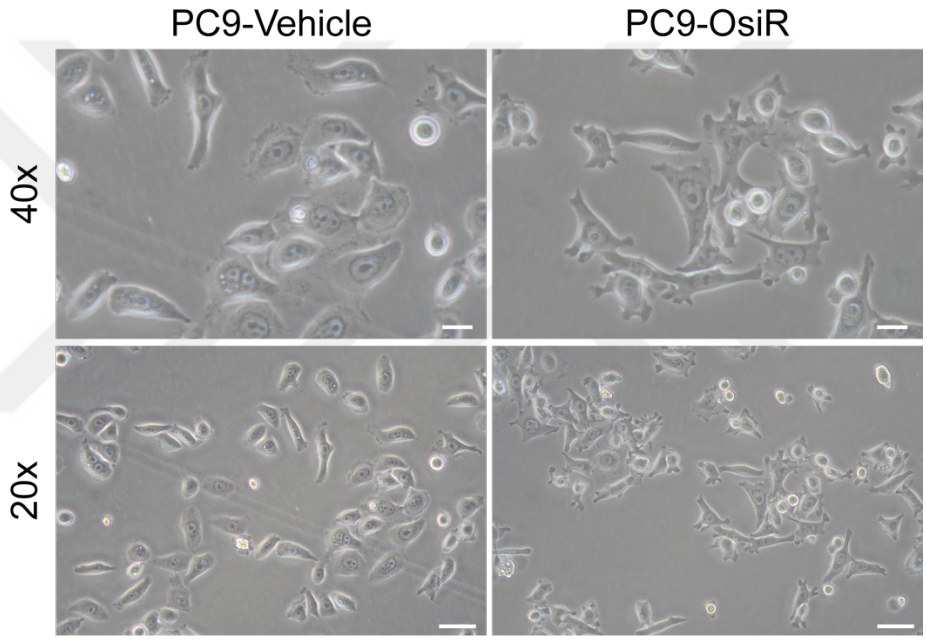

Figure 11: Light microscope images depicting the morphological changes in control cells (PC9-Veh) and osimertinib-resistant cells (PC9-OsiR). (Scale for 20x: 50 µm, scale for 40x: 20 µm)

To evaluate cell viability across a range of osimertinib concentrations and to determine the IC50 values for both PC9-Veh and PC9-OsiR cell lines, an MTT assay was performed. The IC50 values were observed to be around 1 nM for PC9 cells and 3.5 µM for PC9-OsiR cells (Figure 12). The drug resistance index (DRI) was calculated to be approximately 3200.

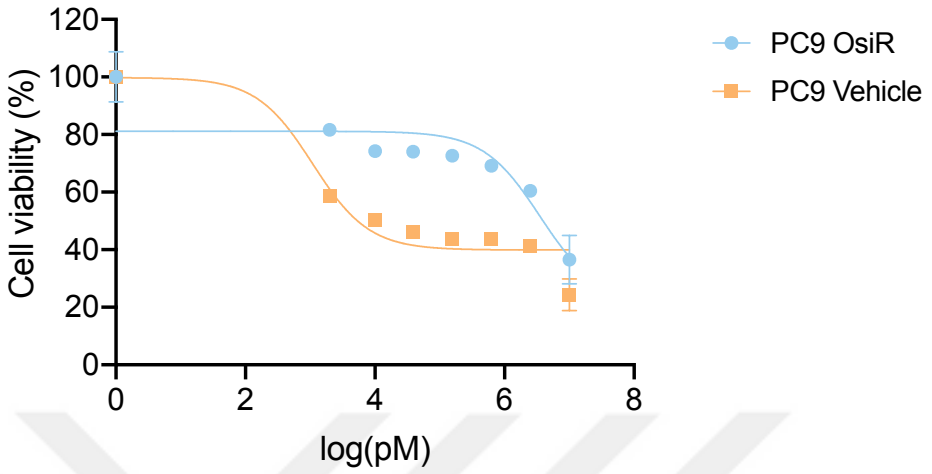

Figure 12: Cell viability graph after 72 hours of Osimertinib treatment in PC9-Veh and PC9-OsiR cells. Treatments were normalized to DMSO (vehicle) control n=6.

4.2. EGFR dependency in PC9-Veh and PC9-OsiR cells

PC9 cells, which harbor constitutively active EGFR, rely on EGFR for their survival. Since osimertinib inhibits EGFR signaling and resistant cells are desensitized to drug challenge, we hypothesized that osimertinib-resistant cells might no longer rely on EGFR for survival. To test this hypothesis, we used an orthogonal approach and performed genetic depletion of *EGFR* gene in both PC9-Veh and PC9-OsiR cell lines. The Renilla, EGFR g10, and EGFR g60 sequences were cloned into the LentiCRISPR-v2 Blasticidin vector, and cells were infected with the resulting viral particles. To confirm successful knockout, protein extracts were collected 10 days post-infection and analyzed using Western blotting (Figure 13).

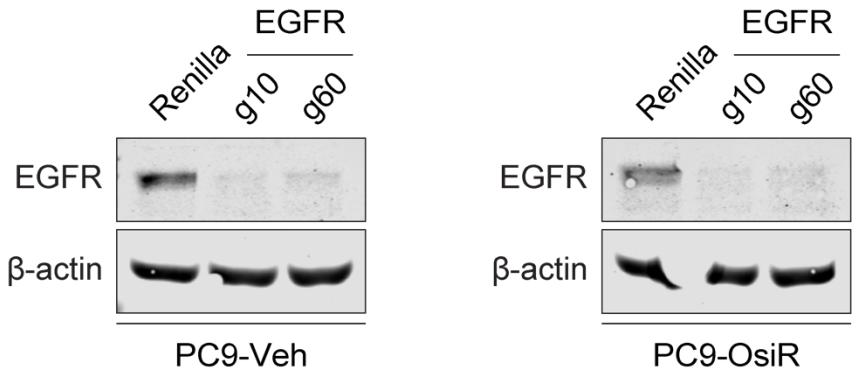

Figure 13: Western blot results of Renilla and EGFR knockout PC9-Veh and PC9-OsiR cell lines. B-actin is used as loading control.

After verifying the knockout, cells were seeded into 6-well plates to assess their EGFR dependency using a long-term 2D colony formation assay. The cells were incubated for 10 days, with medium changes every 3 days. As expected, the EGFR knockout PC9-Veh clones exhibited a markedly reduced colony-forming capacity (Figure 14). In contrast, EGFR knockout PC9-OsiR clones were largely unaffected by EGFR loss, compared to Renilla clone. These findings indicate that PC9-Veh cells are highly dependent on EGFR for their survival and proliferation, whereas PC9-OsiR cells exhibit a significant reduction in EGFR dependency (Figure 14).

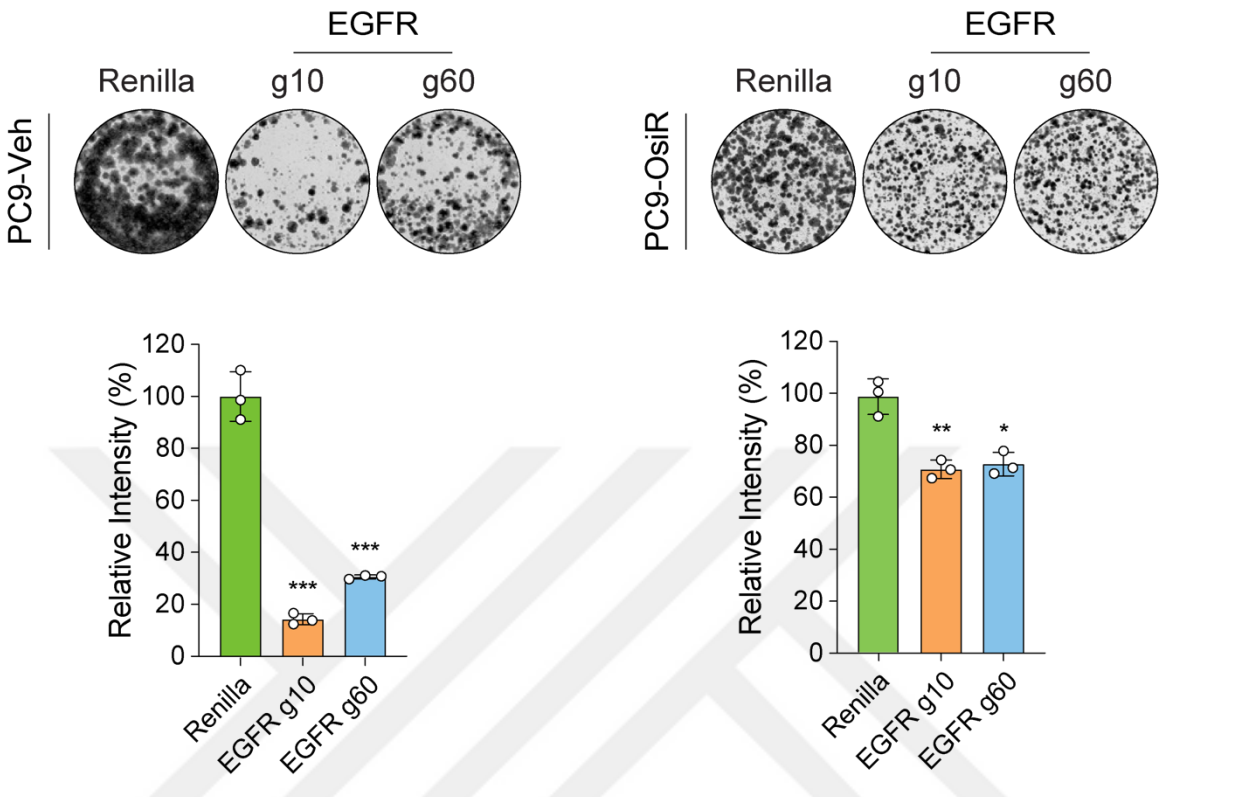

Figure 14: Colony formation assay results of Renilla and EGFR knockout PC9-Veh and PC9-OsiR cell lines. The relative intensity was determined by normalizing the intensities of the EGFR knockout group against those of the Renilla group. Representative images are given. Mean ±SD, n=3.

4.3. Investigating the Mutation Profile of Osimertinib-resistant PC9 Cells

To obtain a preliminary estimate of whether known genetic mechanisms associated with EGFR mutations contribute to drug resistance, we assessed the EGFR mutation status by Sanger sequencing.

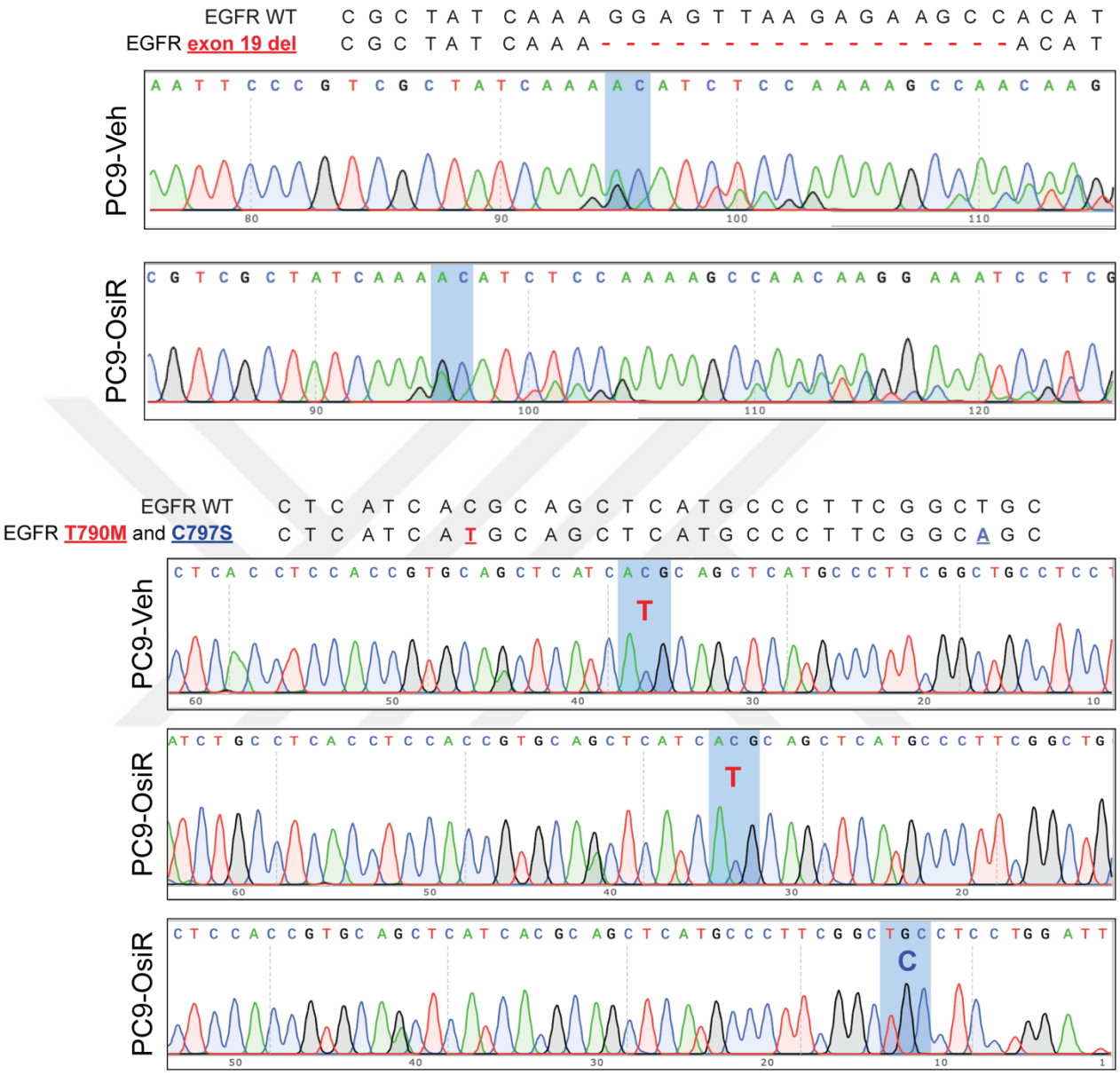

Figure 15: Sanger sequencing results for PC9-Veh and PC9-OsiR cells.

As shown in Figure 15, both PC9-Veh and PC9-OsiR cell lines carry the known 15-nt deletion in EGFR. However, PC9-OsiR cells did not show an additional mutation in the analyzed region, suggesting that resistance is not mediated by secondary EGFR mutations.

PC9 cells are reported to harbor exon 19 deletions in heteroduplexes (103), implying the presence of wild-type EGFR in their genome. To verify this argument, we performed a

genomic PCR with exon 19 primers for to detect wild-type EGFR (Figure 16). Our results indicate that both treatment naive and resistant cells harbor heterozygous mutant EGFR. This finding helps explain why PC9-OsiR cells remain somewhat affected by *EGFR* knockout, despite exhibiting insensitivity to the inhibitor.

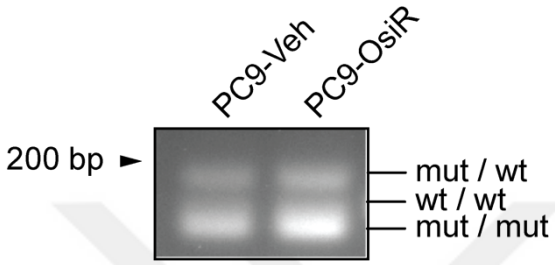

Figure 16: PCR results showing proportions of EGFR homoduplexes (mut/mut and wt/wt) and heteroduplexes (mut/wt).

4.4. Impact of the Osimertinib-resistant State on Cell Proliferation and 2D Colony Formation Capacities in PC9 Cells

After confirming osimertinib resistance through the MTT assay, we measured growth kinetics relative to the control group (Veh) in two separate assays. First, we assessed cell proliferation capacity using a cell count assay. PC9-Veh and PC9-OsiR cells were seeded into 6-well plates at equal densities. Cells proliferation was estimated using a hemocytometer every 2 days, starting 24 hr after seeding. After reaching confluency, the experiment was concluded on day 5. As shown in Figure 17, PC9-OsiR cells exhibited reduced proliferation capacity compared to PC9-Veh cells.

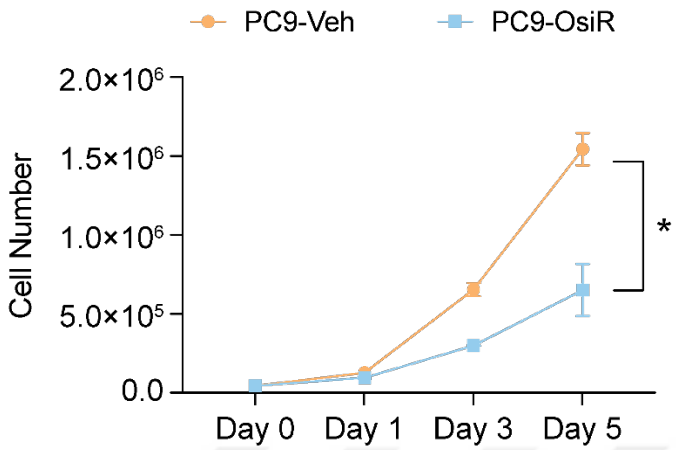

*Figure 17: Cell proliferation rates of PC9-Veh and PC9-OsiR cell lines. Cell counts were measured every 2 days starting 1 day after cell seeding. Mean±SD, n=2, ***p<0.001,*

To determine how the osimertinib-resistant cell state affects colony-forming capacity, we performed a long-term 2D colony formation assay with PC9-OsiR cells. For this, 1000 cells were seeded into each well of 12-well plates and allowed to form colonies over a period of 10 days. After the incubation period, the plates were scanned, and colony intensities were measured. The results revealed that PC9-OsiR cells exhibited a slightly lower, but not significantly different, 2D colony formation capacity compared to PC9-Veh cells (Figure 18).

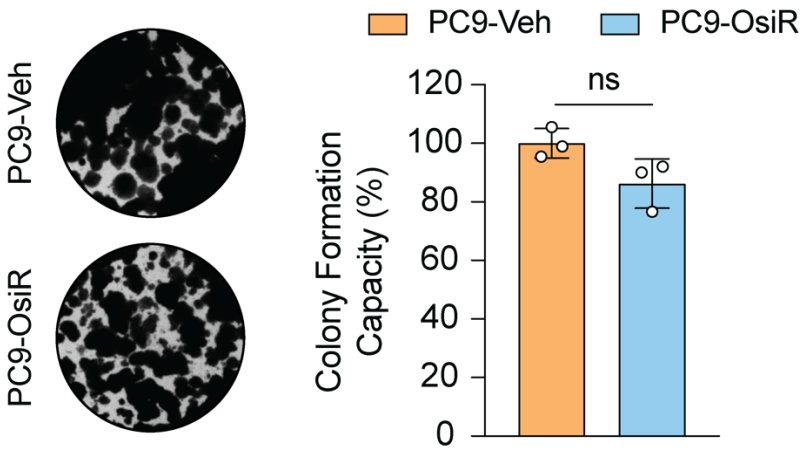

Figure 18: Clonogenic capacity of PC9-Veh and PC9-OsiR cell lines. Colony formation capacity was

measured by normalizing the intensities of PC9-OsiR cells to PC9-Veh cells. Pixel intensities were calculated with ImageJ software. Representative images are given. Mean±SD, n=3, p=0.0718.

4.5. Effect of the Osimertinib-resistant State on Cell Invasion Capacity in PC9 Cells

Given that PC9-OsiR cells displayed morphological hallmarks reminiscent of a mesenchymal phenotype, a trait often associated with EGFR-TKI resistance (104), we investigated their phenotypic characteristics using a transwell invasion assay. Cells were seeded into Matrigel-coated Boyden chambers, which were then filled with FBS-reduced medium. To induce cell invasion, complete medium was added to the wells. After 48 hr, the assay was terminated with crystal violet staining. Images of the Boyden chambers were captured with a light microscope, and the number of invaded cells per field was quantified using ImageJ software. Contrary to our expectations, the results revealed that PC9-OsiR cells exhibited significantly reduced invasion capacity compared to PC9-Veh cells (Figure 19).

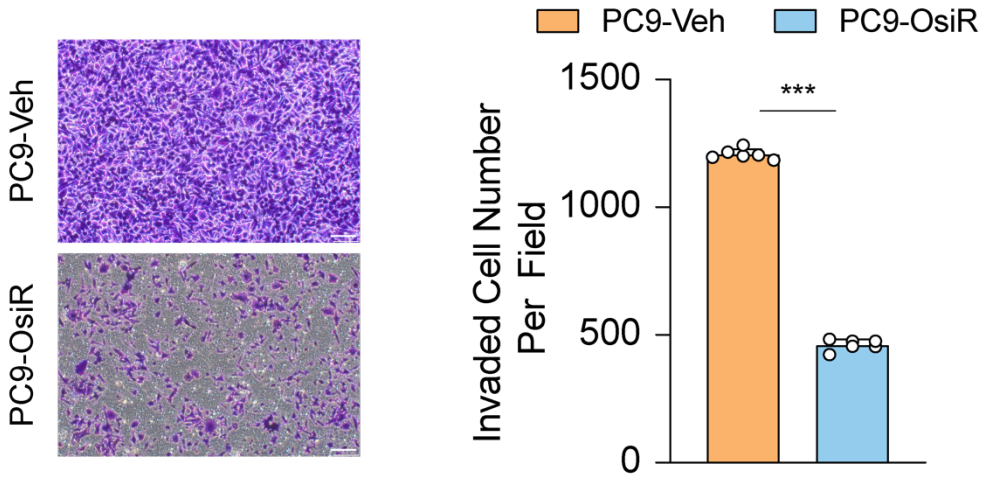

Figure 19: Representative images (left) and invasion capacity graph (right) of PC9-Veh and PC9-OsiR cells. Invaded cells were counted from randomly selected 6 areas. 10X magnification, scale bar represents 100 µm.

4.6. Investigating the Response of the other generation and cytotoxic inhibitors

It is well-established that osimertinib-resistant NSCLC cells can develop cross-resistance to earlier-generation EGFR-TKIs (105,106). To explore this phenomenon, we assessed the responses of PC9-Veh and PC9-OsiR cells to first-generation (Erlotinib) and second-generation (Dacomitinib) EGFR-TKIs. Our results demonstrated that while PC9-Veh cells were sensitive to both Erlotinib and Dacomitinib at comparable doses, PC9-OsiR cells exhibited significant insensitivity to these inhibitors (Figure 20). This indicates that cells resistant to osimertinib can also develop resistance to prior EGFR-TKIs. Additionally, we evaluated the response of these cells to Paclitaxel, a cytotoxic chemotherapy agent (Figure 20). PC9-OsiR cells showed slightly reduced sensitivity to Paclitaxel compared to PC9-Veh cells. However, the low nanomolar IC50 values for Paclitaxel suggest that osimertinib resistance primarily affects the EGFR pathway and does not lead to significant cross-resistance to chemotherapeutic agents.

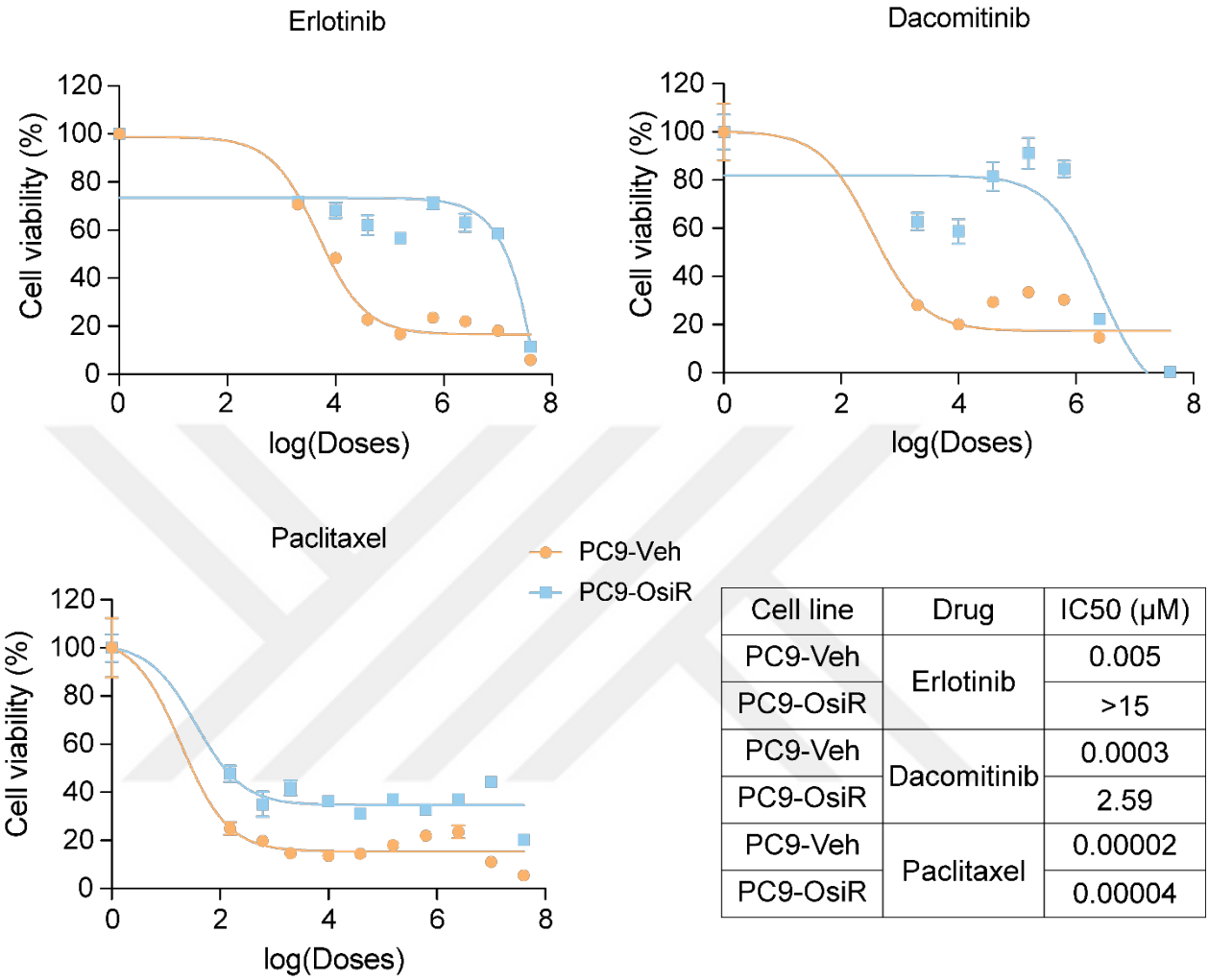

Cell line	Drug	IC50 (μM)
PC9-Veh	Erlotinib	0.005
PC9-OsiR		>15
PC9-Veh	Dacomitinib	0.0003
PC9-OsiR		2.59
PC9-Veh	Paclitaxel	0.00002
PC9-OsiR		0.00004

Figure 20: Cell viability graphs and IC50 values after 72 hours of Erlotinib, Dacomitinib and. Paclitaxel treatment in PC9-Veh and PC9-OsiR cells. Treatments were normalized to DMSO (vehicle) control, n=6.

4.7. Characterizing Morphological Changes in Osimertinib-Resistant PC9 Cells

As previously noted, osimertinib-resistant PC9 cells displayed morphological changes. Initially, this phenotype was attributed to epithelial-to-mesenchymal transition (EMT) (37,107). To investigate this phenotype, we conducted three assays focusing on well-known EMT markers: E-cadherin (E-cad) as an epithelial marker and Vimentin (Vim) as a mesenchymal marker. First, we measured the relative expression levels of these genes using qRT-PCR. Our results indicated that while the expression of the CDH1 gene, which

encodes E-cadherin, remained unchanged, there was a significant increase in the expression of Vimentin (Figure 21).

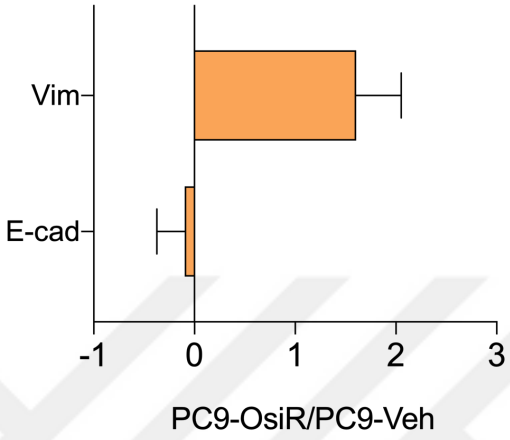

Figure 21: qPCR results for EMT marker genes in PC9-Veh and PC9-OsiR cells

Secondly, changes in EMT markers in cells were examined by western blot method. As shown in Figure 22, E-cadherin expression remained unchanged in the PC9 cell line. More importantly, Vimentin expression was not detectable at the protein level.

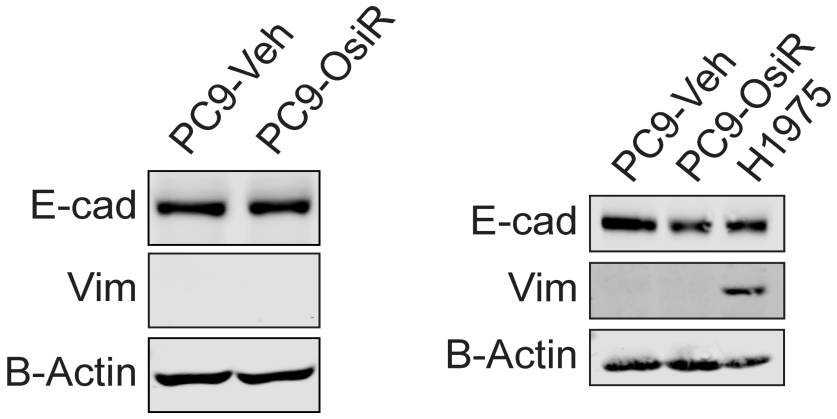

Figure 22: Western blot results for E-cadherin and Vimentin in PC9-Veh and PC9-OsiR cells. The result at the right is for positive control to validate vimentin antibody. H1975 cell line used as positive control. B-actin used as loading control.

To further investigate the cellular distribution of E-cadherin and Vimentin, immunofluorescence staining was conducted, with Phalloidin used to visualize F-actin proteins and assess morphological changes (Figure 23).

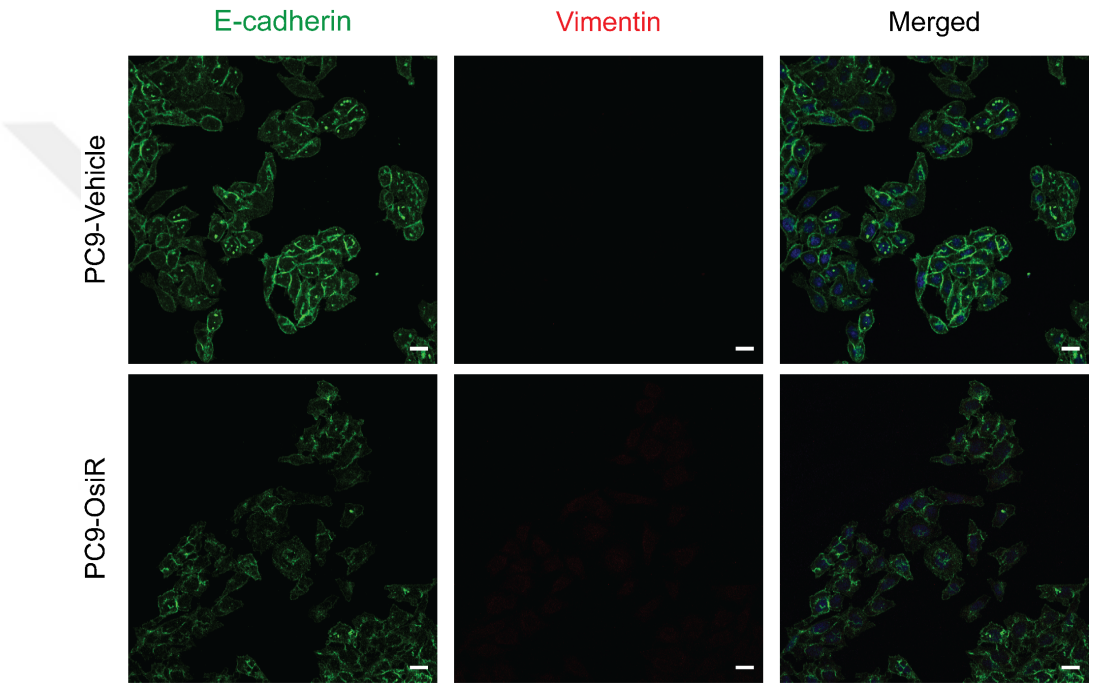

Figure 23: E-cadherin and Vimentin staining in PC9-Veh and PC9-OsiR cells. DAPI is used as a counterstain dye.

As shown in Figure 24, Phalloidin staining revealed cell protrusions and alterations in cell morphology. These findings suggest that while morphological changes in the PC9 cell line may indicate an epithelial-to-mesenchymal transition (EMT) but are not directly regulated by E-cadherin and Vimentin.

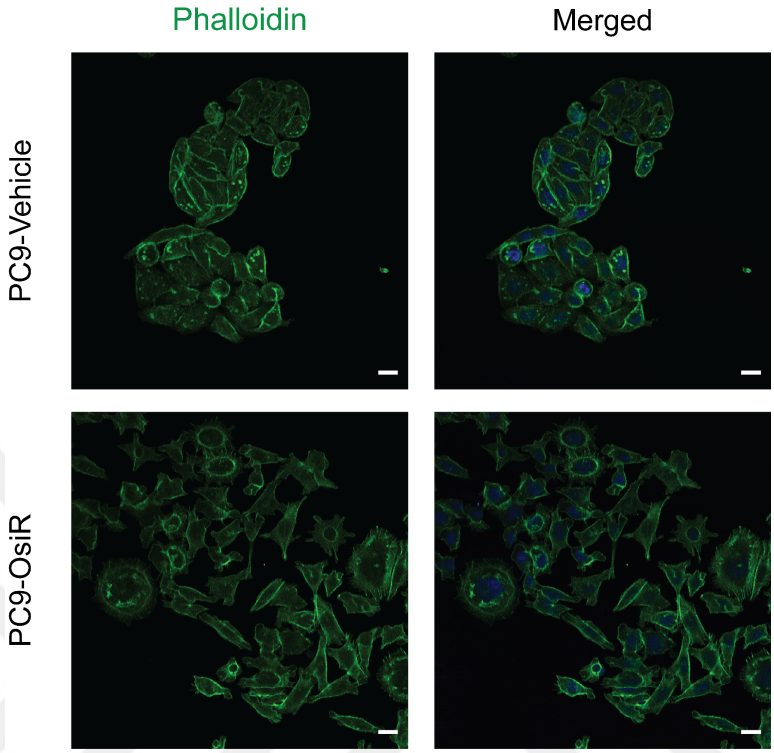

Figure 24: Phalloidin staining depicting cellular morphology in PC9-Veh and PC9-OsiR cells. DAPI is used as a counterstain dye.

4.8. Exploring Alterations in Bypass Signaling Pathways in Resistant Cells

In the subsequent characterization of PC9-OsiR cells, alterations in the EGFR signaling pathway were examined. Specifically, activation markers for the EGFR (p-EGFR, Y1068) and its downstream components (p-AKT, S473; p-ERK, T202/Y204; and p-STAT3, Y705) were assessed using Western blotting. Cells from both groups were seeded in 6 cm plates and grown to approximately 75% confluency. Once sufficient confluency was achieved, proteins were extracted, and western blotting was performed to detect changes in the EGFR signaling pathway.

Compared to PC9-Veh cells, PC9-OsiR cells exhibited a significant decrease in phosphorylation of EGFR at Tyrosine 1068, consistent with previous findings (108). Compared to PC9-Veh cells, PC9-OsiR cells exhibited a significant decrease in

phosphorylation of EGFR at Tyrosine 1068, consistent with previous findings (Figure 25). These results show that endogenous EGFR activity significantly decreases with the development of osimertinib resistance, whereas AKT signaling activity from the downstream pathway increases. There was a decrease in STAT3 signaling activity. This suggested that the dependency of the PC9-OsiR on EGFR activity may have shifted to the AKT axis via an alternative bypass signaling pathway.

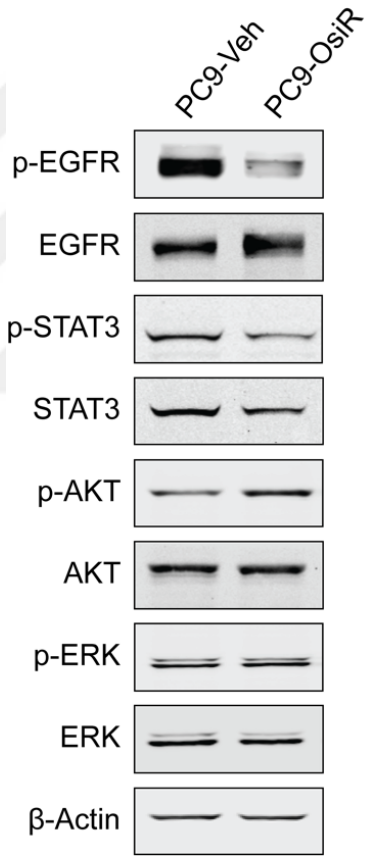

Figure 25: Western blot result showing alterations in bypass signaling pathways in PC9-Veh and PC9-OsiR cells. B-actin used as loading control.

4.9. Effect of Increasing Osimertinib Doses on Colony Formation Capacity in PC9-OsiR and PC9-Veh Cells

Next, a 2D colony formation assay was performed with increasing doses of osimertinib. Cells were seeded in 12-well plates in triplicate. The following day, osimertinib was administered at doses of 5 μM, 1 μM, 200 nM, 100 nM, 50 nM, 10 nM and 2 nM. The drug-containing medium was refreshed every three days. After 10 days, the experiment was concluded with crystal violet staining. Images were captured using the LI-COR Odyssey CLX system, and the colonies were analyzed using ImageJ software. As expected, PC9-Veh cells exhibited high sensitivity to increasing doses of osimertinib. In contrast, PC9-OsiR cells showed no significant reduction in colony, demonstrating their resistance to the drug (Figure 26).

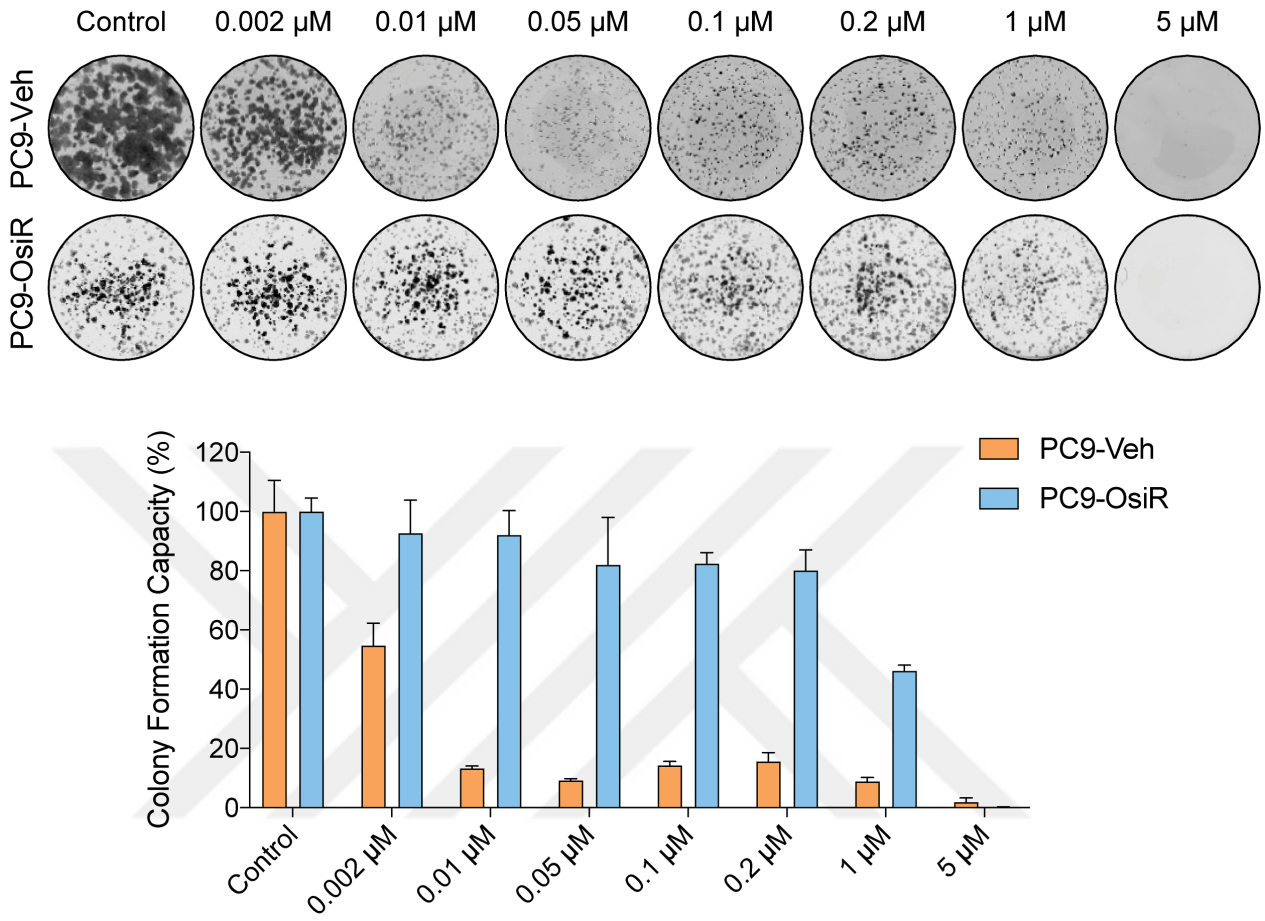

Figure 26: Colony formation capacity of PC9-Veh and PC9-OsiR cells at different drug doses after the development of resistance. Representative images are given. Mean ±SD, n=3, technical replicates.

4.10. Impact of Increasing Osimertinib Doses on Proliferation Index and Growth Kinetics in PC9-OsiR and PC9-Veh Cells

We next evaluated the impact of osimertinib challenge on cell proliferation in resistant cells. To this end, cells were seeded into 24-well plates. The next day of seeding, osimertinib was administered at doses of 1 µM, 500 nM and 100 nM. After 48 hours, BrdU labeling was performed to identify actively proliferating cells. The results revealed that osimertinib significantly reduced the proliferation rate in PC9-Veh cells compared to untreated controls. In contrast, PC9-OsiR cells showed minimal change in proliferation

rates under the same osimertinib treatment conditions (Figure 27). This confirms that PC9-OsiR cells are less affected by osimertinib-induced inhibition of proliferation compared to the sensitive PC9-Veh cells.

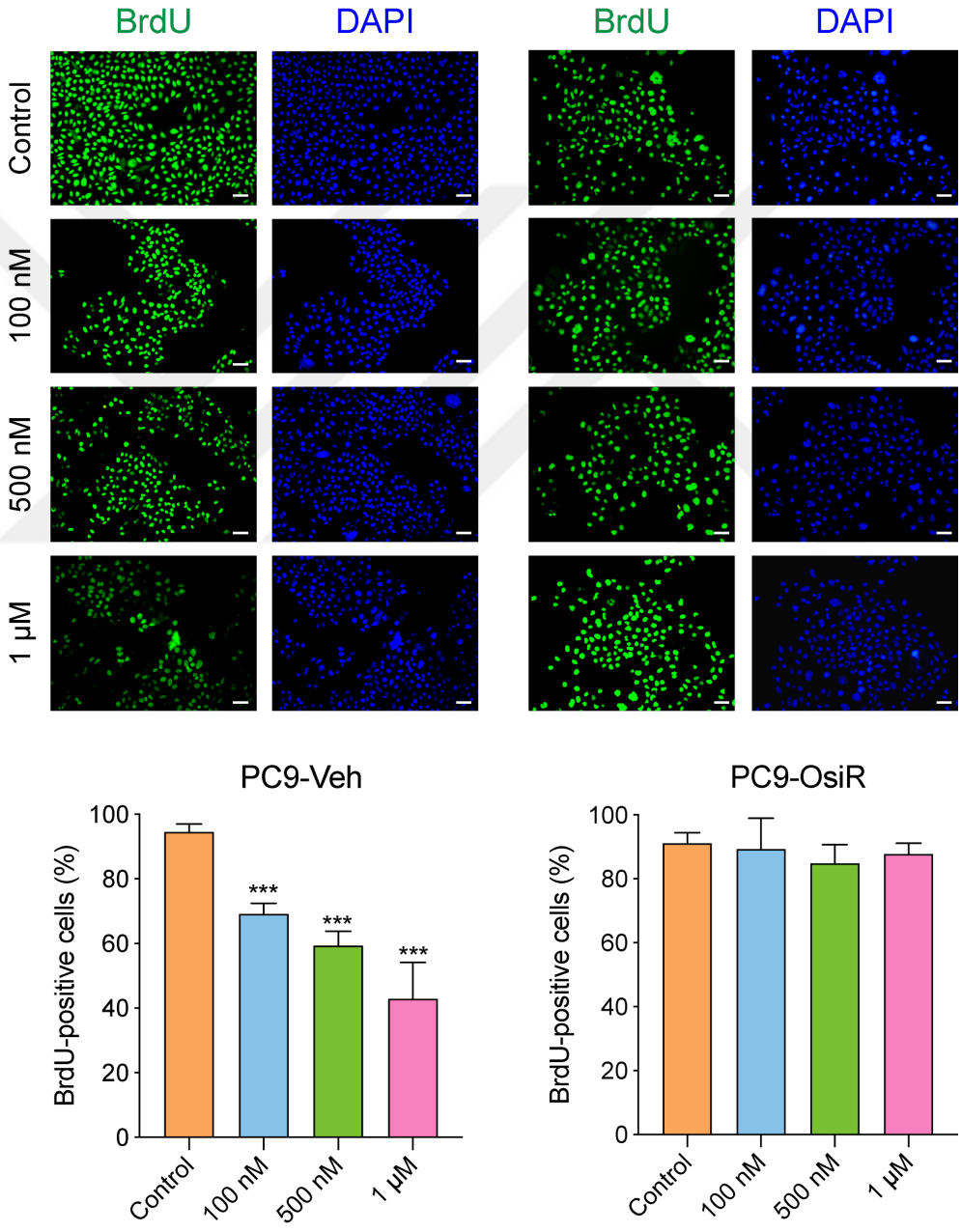

Figure 27: BrdU labeling results of PC9-Veh and PC9-OsiR cells with increasing doses of osimertinib. Mean ± SD, n=8.

To corroborate the observations with proliferation index, cell cycle profiles were analyzed under the same experimental conditions. Cells were seeded into 6-well plates and treated with increasing doses of osimertinib for 72 hours. Cell cycle analysis was performed using PI staining. Notably, PC9-Veh cells exhibited G1 phase arrest in a dose-dependent manner. Conversely, PC9-OsiR cells showed no significant changes in their cell cycle profiles, regardless of osimertinib concentration (Figure 28).

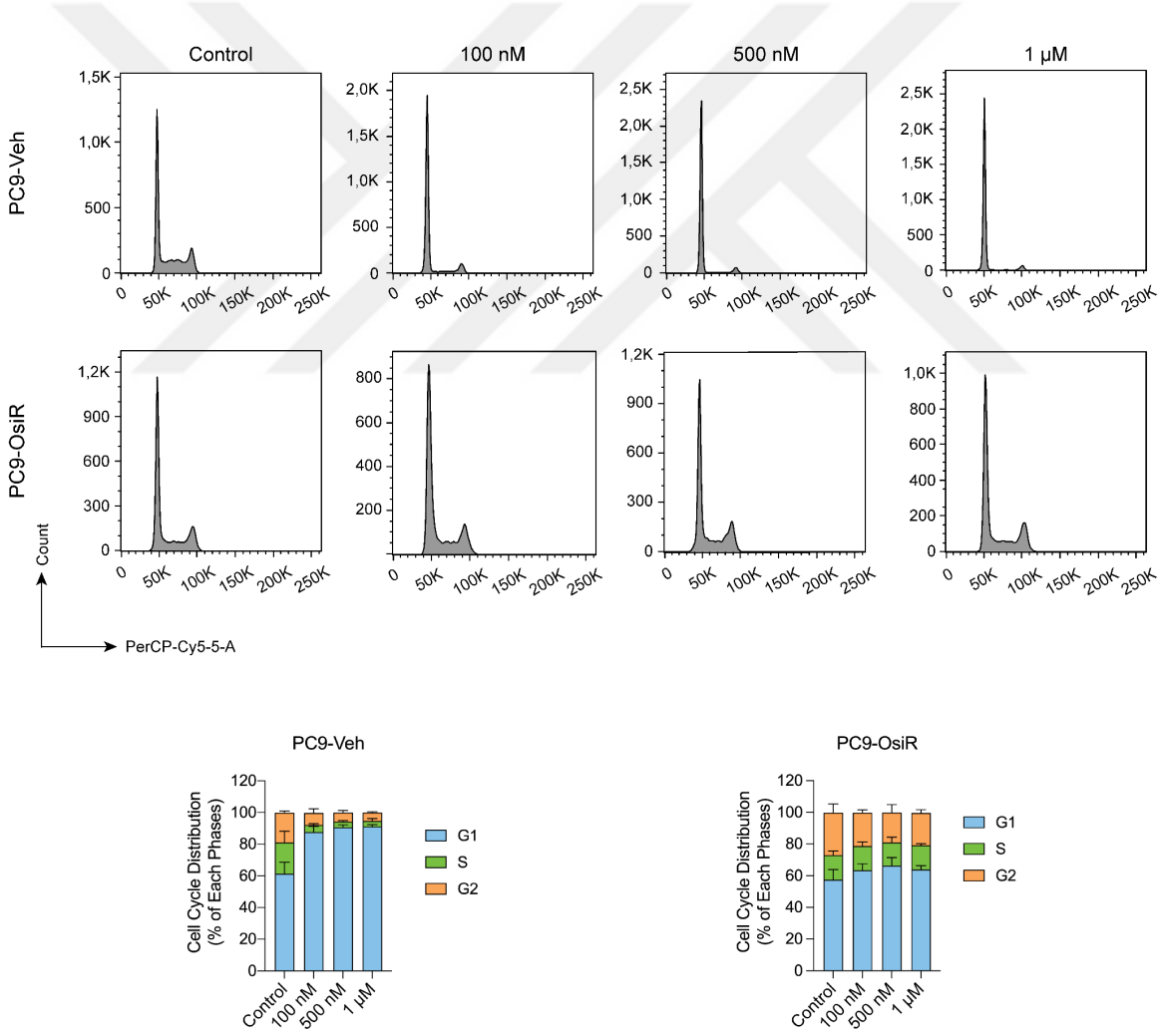

Figure 28: Cell cycle distribution of PC9-Veh and PC9-OsiR cells with increasing osimertinib concentrations. n=3, biological replicates.

4.11. Effect of Increasing Osimertinib Doses on Motility in PC9-OsiR and PC9-Veh Cells

To assess the impact of osimertinib on phenotypic hallmarks, cell motility was evaluated using a wound healing assay under osimertinib treatment. Cells were seeded into a 6-well plate, and the following day, they were exposed to increasing concentrations of osimertinib for 24 hours. A scratch was then created using a 200 µL pipette tip, and the medium was replaced with drug-supplemented 2% FBS medium. The scratch areas were measured at T0, T24, and T48, and the percentage of closure was calculated relative to T0. As shown in Figure 29, PC9-Veh cells exhibited a significant reduction in motility with increasing osimertinib doses. However, the motility of PC9-OsiR cells remained unaffected by osimertinib. Consistent with the invasion experiments, the motility rate of PC9-Veh cells was higher than PC9-OsiR cells.

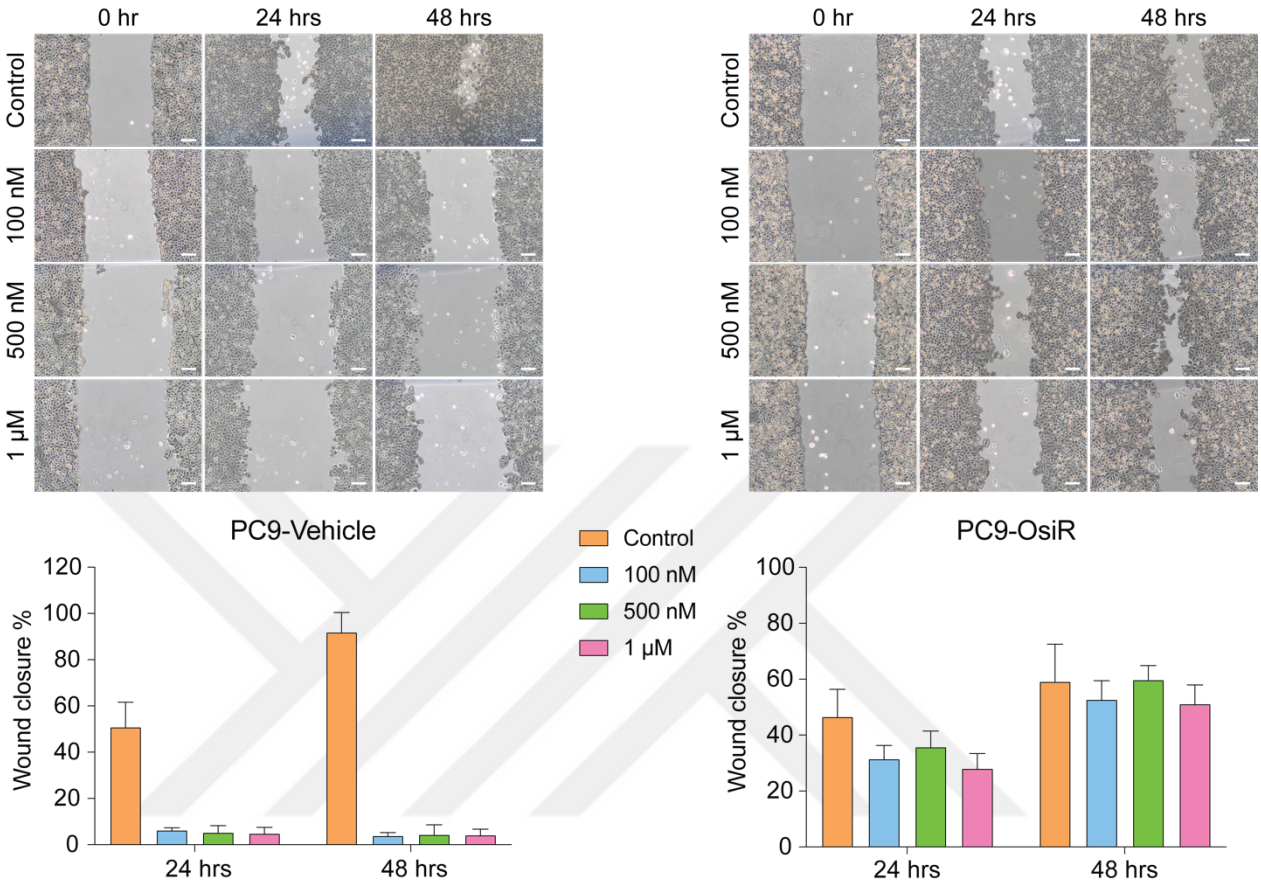

Figure 29: Wound healing assay of PC9-Veh and PC9-OsiR cells. n=8.

4.12. Bypass Signaling Pathways Changes in PC9-OsiR and PC9-Veh Cells in Response to Escalating Osimertinib Doses

We next investigated the effect of osimertinib treatment on the EGFR signaling pathway, Cells were treated with osimertinib for 5 hr and western blot analysis was performed. As expected, increasing osimertinib doses significantly inhibited p-EGFR, p-AKT and p-ERK in PC9-Veh cells. In contrast, in PC9-OsiR cells, phosphorylation of p-EGFR and p-ERK decreased, but no significant change was observed in AKT pathway activity with increased osimertinib doses. These findings suggest that while endogenous EGFR activity was substantially reduced in PC9-OsiR cells with higher osimertinib doses, AKT signaling remained unaffected (Figure 30). This finding aligns with earlier results,

indicating that the survival dependency on EGFR signaling has shifted to an alternative bypass mechanism involving AKT activity.

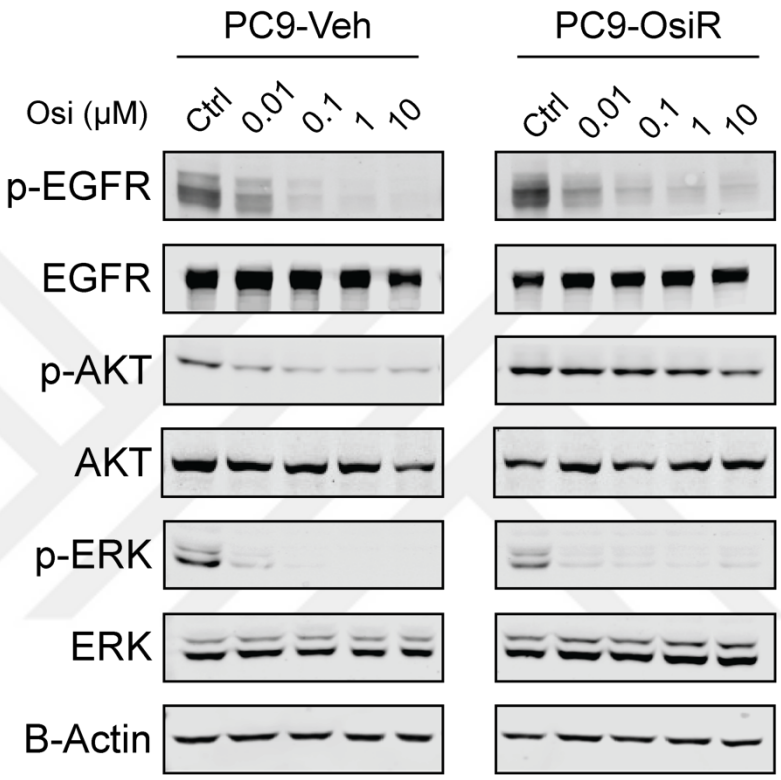

Figure 30: Western blot analysis showing alterations in EGFR pathway components in accordance with increased doses of osimertinib in PC9 group. β-actin was used as a loading control.

4.13. Transcriptomic Profiling of Osimertinib-Resistant PC9 Cells

To explore the molecular mechanisms associated with resistance and identify factors potentially contributing to its development, a comparative whole-genome transcriptome analysis (RNA sequencing) was conducted on PC9-Veh and PC9-OsiR cells. The initial step in RNA sequencing analysis involved assessing the overall similarity/distinction between the samples in this context, our data were analyzed using principal component analysis (PCA). A distinct biological separation between the two groups was evident along the PC1 axis (Figure 31). The technical variance between replicates was minimal, as indicated by the limited separation along the PC2 axis. Additionally, the separation

between the groups and the consistency among the triplicate replicates were further illustrated through a correlation heatmap (Figure 31).

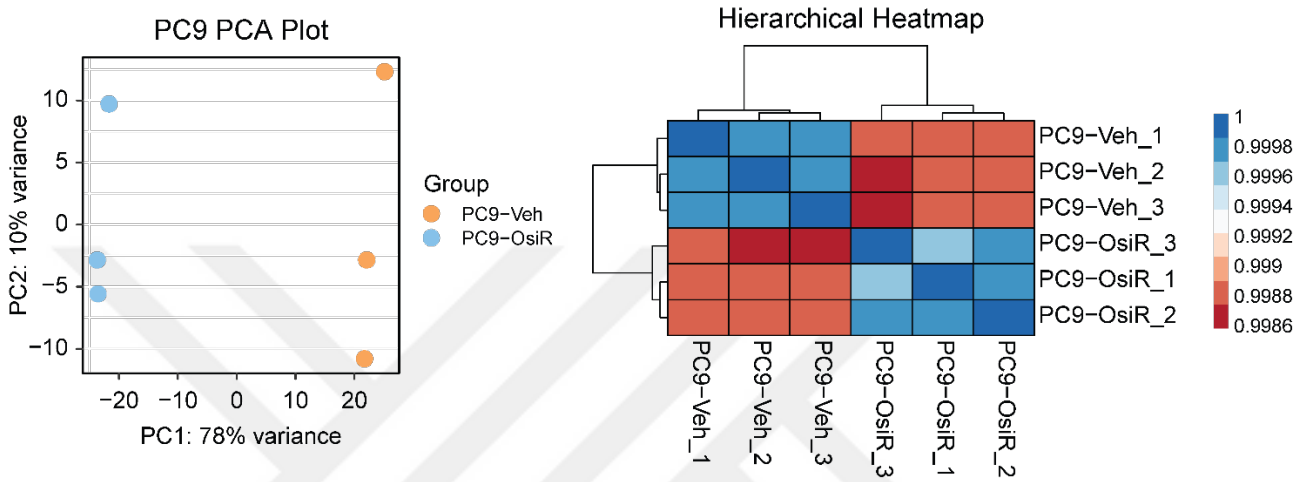

Figure 31: Principal Component Analysis (PCA) plot (left) and correlation heatmap (log2(CPM+1)) (right) of PC9-Veh and PC9-OsiR triplet repeats.

Next, the statistical significance of the differences in gene expression levels between the PC9 and PC9-OsiR groups was determined. Genes exhibiting statistically significant differential expression were identified and ranked according to the corrected p-value (FDR). Various visualizations were generated to represent the gene clusters with significant changes. Specifically, a heatmap displaying a total of 13,403 transcripts with CPM values of 1 or higher was created using triplicate samples from both groups Figure 32.

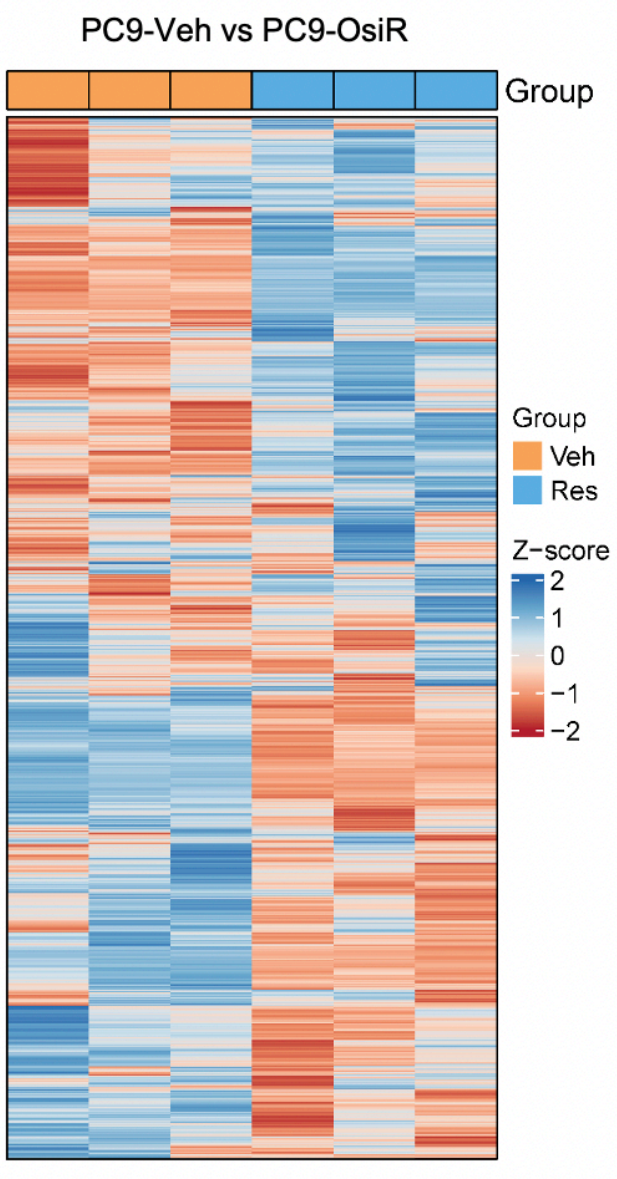

Figure 32: Heatmap of all transcripts that passed the log_2(CPM+1) filter in PC9 group , n=3 for each sample. A total of 13403 transcripts passed.

An MA plot was generated to visualize gene expression changes between PC9-Veh and PC9-OsiR cells (Figure 33). In this plot, the X-axis represents the mean expression level

(A, logCPM) of each gene, while the Y-axis depicts the log2 fold change (M, logFC) between the two conditions.

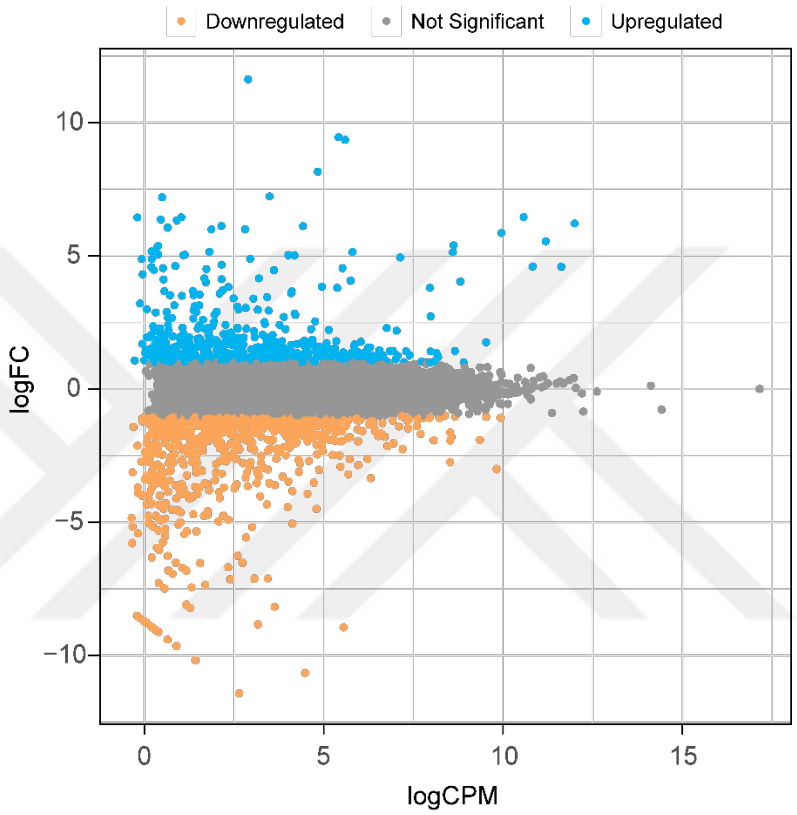

Figure 33: MA plot showing the alterations in gene expression profile for PC9 group. Log_2FC threshold value is <-1 and >1. The number of genes with increased expression (blue) exceeding this threshold is 557, while the number of genes with decreased expression (orange) is 852. The genes shown in gray dots are genes with insignificant expression.

As an additional method for representing gene expression changes between PC9-Veh and PC9-OsiR cells, a volcano plot was created (Figure 34). This plot visualizes genes with large fold changes and statistical significance, combining both the magnitude of change and the significance level in a single graphical representation.

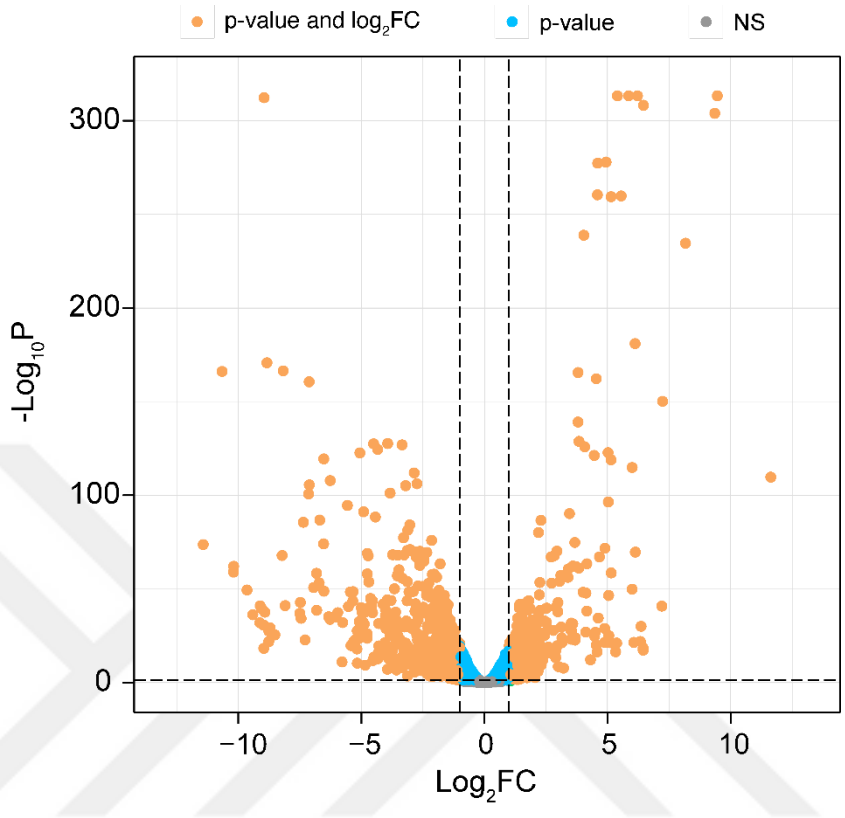

Figure 34: Volcano plot demonstrating the changes in gene expression profile for PC9 group. Log_2FC threshold value is <-1 and >1. p-value threshold is <0.05. The number of genes with altered expression exceeding these thresholds (orange) is 1406, while the number of genes with only a significant p-value (blue) is 852. Genes shown in gray dots are genes with insignificant expression.

4.14. Functional Insights from Transcriptomic Analysis of Osimertinib-Resistant PC9 Cells

After revealing the changes in the global transcriptome, gene ontology (GO), pathway enrichment and Gene Set Enrichment Analysis (GSEA) were performed to better understand which pathways and/or phenotypes these changes affect. For gene ontology and pathway enrichment analyses, gene lists were divided into two different gene list groups as “up” and “down” using an absolute value threshold of 1. The genes in these lists were analyzed using GO, KEGG and ReactomePA databases. The terms showing significant changes as a result of these analyses are presented with dot plots in Figures 35 and 36.

The enrichment analysis shown in Figure 35 revealed processes that demonstrate the presence of the EMT phenotype observed in PC9-OsiR cells. In particular, biological processes such as extracellular structure organization, axon guidance, and external capsule structure organization stand out as terms explaining this phenotype. In addition, AKT activation emerged as an alternative bypass signaling pathway in PC9-OsiR cells. Supporting this conclusion, the PI3K-AKT signaling pathway stood out as a significant term in the enrichment analysis with up-regulated genes. On the other hand, other essential pathways for cell survival such MAPK signaling pathway and TNF signaling pathway had appeared as a hit in the enrichment analysis of upregulated genes. Interestingly, interleukin signaling which is highly related to immune system also emerged as enriched terms.

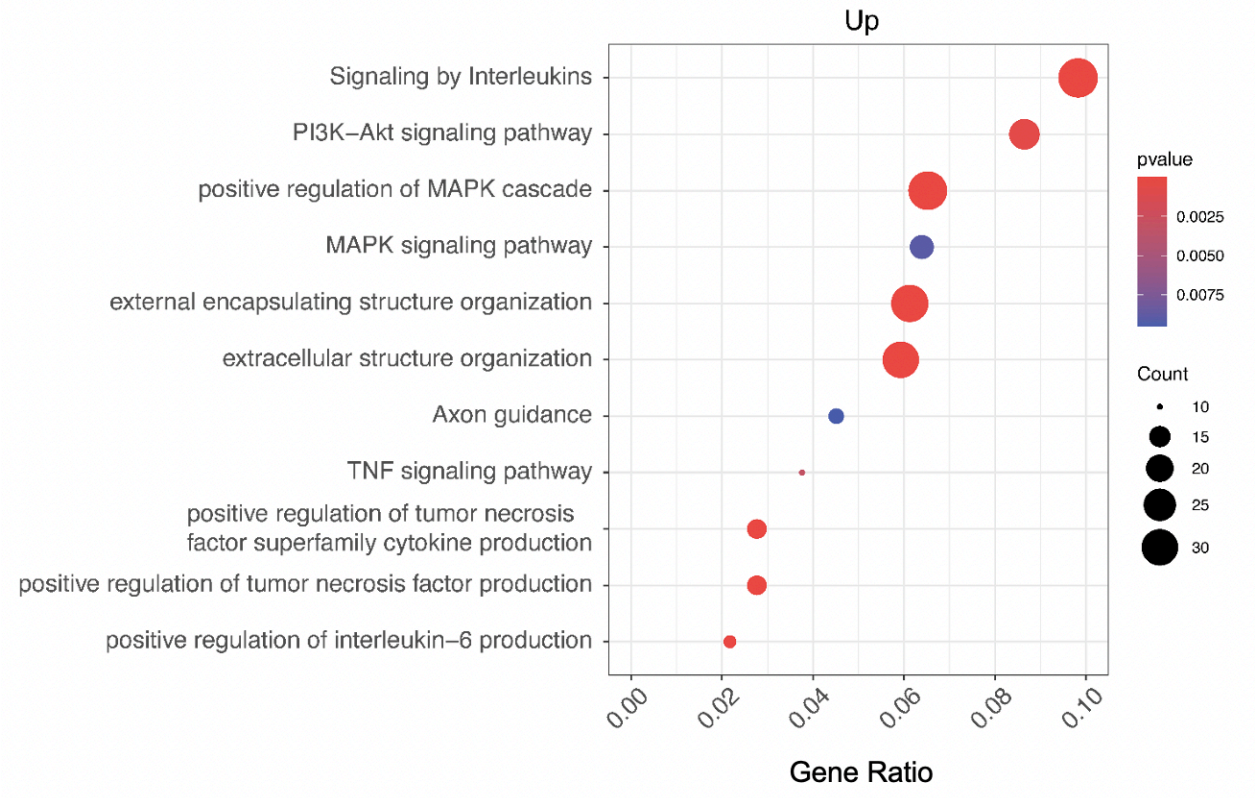

Figure 35: Enrichment analysis for upregulated genes in PC9-OsiR.

Enrichment analysis on downregulated genes shown in Figure 36 revealed the epithelial cell morphology of PC9-Veh cells. In addition, EGFR signaling activation was enriched in the analysis of downregulated genes and revealed as a significant term. This finding indicates as a result confirming the mutation specific EGFR activation known in the literature in PC9 cells. As in the analysis of upregulated genes, other essential pathways for cell survival, such as the MAPK signaling pathway, also emerged as a hit in the enrichment analysis of downregulated genes.

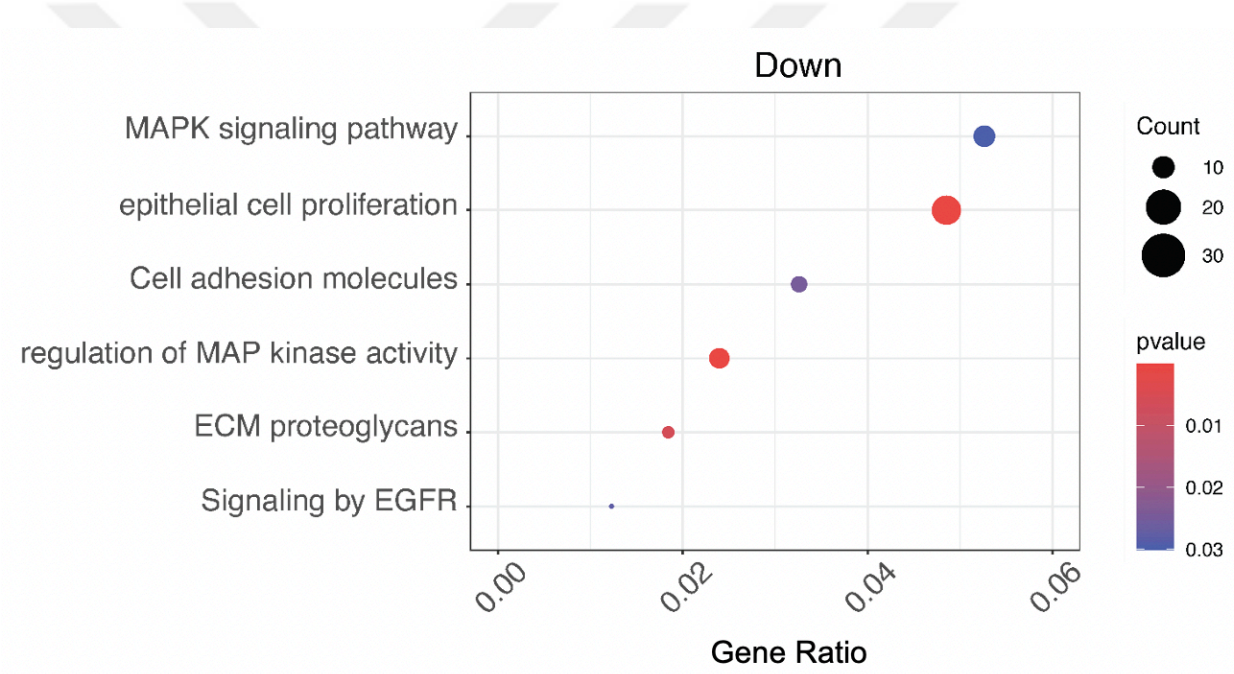

Figure 36: Enrichment analysis for downregulated genes in PC9-OsiR.

GO and pathway enrichment analysis provided insights to unveil the differences between the two cells (PC9-Veh and PC9-OsiR). GSEA was also performed to better understand the distinction between the two biological states. In PC9-OsiR cells, the gene set named extracellular matrix organization which is characterized by the EMT phenotype was at the top of the list and showed a significant difference. As shown in Figure 37, in line with previous result described above gene sets enriched in the resistant state includes inflammatory response, TNF signaling via NFKB, IL6/JAK/STAT3 signaling, and insulin

secretion gene sets were significantly enriched. These findings indicate a significant change in the secretome of PC9-OsiR cells and a change in the intercellular communication system. As depicted in Figure 37, gene sets indicating increased migration capacity and increased cell survival were enriched in PC9-Veh cells with high EGFR activity. These findings are consistent with data in the literature and results from characterization experiments. These results suggested that the top-ranked gene sets are consistent with the characterization experiment results of sensitive cells and are also consistent with the biology of the cell.

Enriched in resistant state:

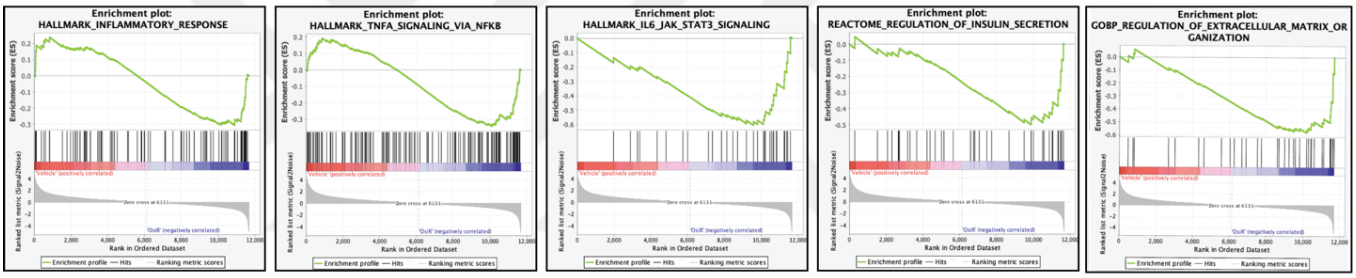

Enriched in sensitive state:

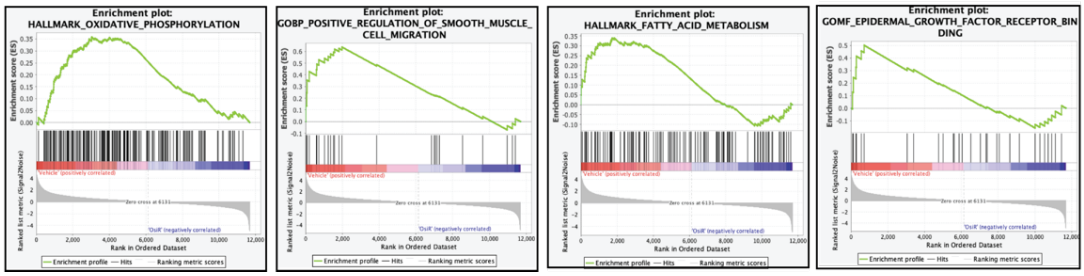

Figure 37: Selected gene sets from GSEA of PC9 cell line

4.15. Generation of Osimertinib-resistant H1975 Cell Line

The H1975 cell line, which carries the L858R mutation in exon 21 and the T790M mutation in exon 20 of the EGFR gene, was also used in this study to model osimertinib resistance. To determine the initial dose for generating resistance, the IC50 of osimertinib was

calculated for the parental H1975 cell line. For this, 2,500 cells were seeded into a 96-well plate, and osimertinib was applied at doses ranging from 16 µM to 0.001 µM (1:4 dilution factor) the following day. After 72 hrs of incubation with osimertinib, crystal violet staining was performed to assess cell viability relative to the control group (DMSO). The IC50 value of osimertinib was calculated to be 2.5 nM (Figure 38).

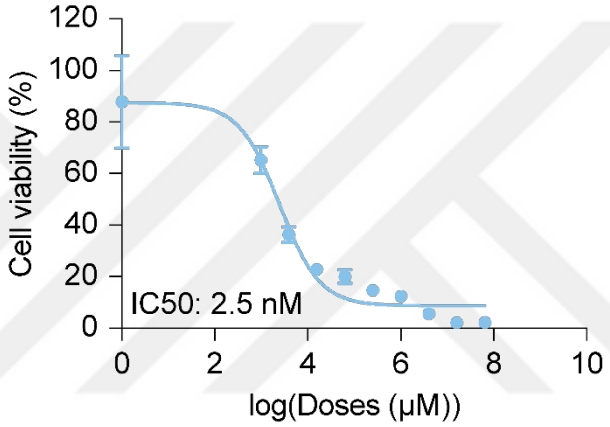

Figure 38: IC50 graph of osimertinib in H1975 (parental) cell line. The half-maximal inhibitory dose of osimertinib on H1975 was shown in the graph. (n=6, as technical replicates), calculated using GraphPad Prism 8 software, n=6.

The same dose escalation methodology was employed to generate the osimertinib-resistant H1975 cell line (H1975-OsiR). Similar to PC9-OsiR cells, the H1975-OsiR cells displayed significant cellular protrusions, which were among the initial morphological changes observed following the acquisition of resistance (Figure 39).

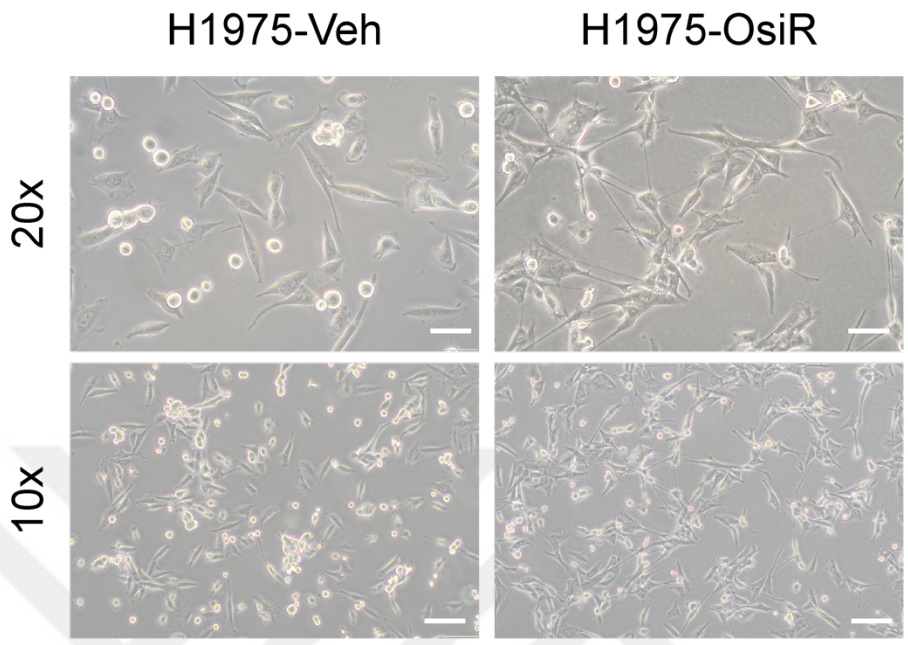

Figure 39: Light microscope images depicting the morphological changes in control cells (H1975-Veh) and osimertinib-resistant cells (H1975-OsiR). (Scale for 20x: 50 µm, scale for 40x: 20 µm)

As previously described in the PC9 section, an MTT assay was conducted to assess cell viability and to calculate the IC50 values for H1975-Veh and H1975-OsiR cell lines in response to varying concentrations of osimertinib. The IC50 values for osimertinib were determined to be 6.18 nM for H1975-Veh cells and 2.24 µM for H1975-OsiR cells (Figure 40). The drug resistance index (DRI) was calculated as 362.46.

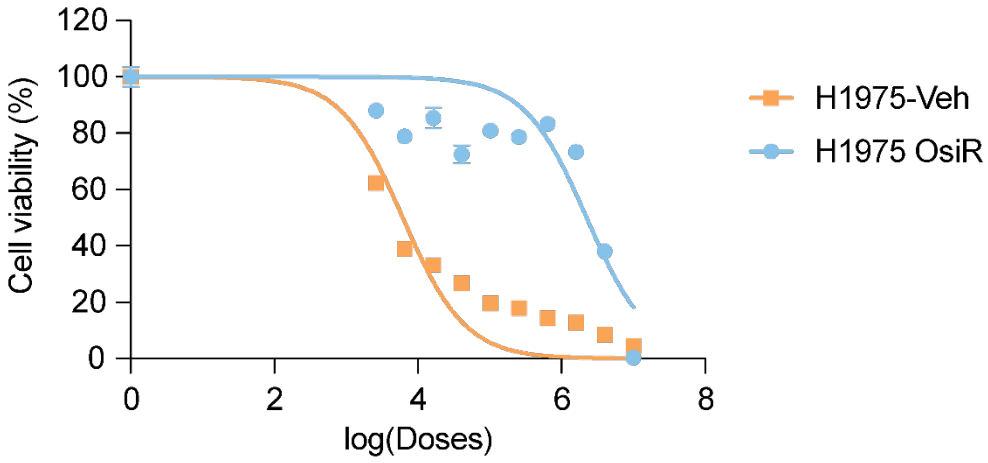

Figure 40: Cell viability graph after 72 hours of Osimertinib treatment in H1975-Veh and H1975-OsiR cells. Treatments were normalized to DMSO (vehicle) control n=6.

4.16. EGFR dependency in H1975-Veh and H1975-OsiR cells

H1975 cells, which rely on constitutively active EGFR for survival, were investigated for their dependency on EGFR following the acquisition osimertinib resistance. To test this, we used CRISPR/Cas9 to knock out EGFR in both H1975-Veh and H1975-OsiR cell lines. EGFR knockout clones were generated as described previously (Figure 41).

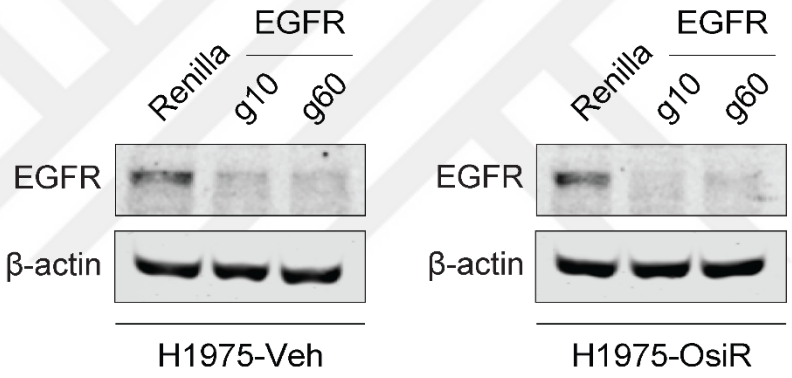

Figure 41: Western blot results of Renilla and EGFR knockout H1975-Veh and H1975-OsiR cell lines. B-actin is used as loading control.

After verifying the knockout, cells were seeded into a 6-well plate to assess their response to EGFR knockout using a colony formation assay, as described earlier. As anticipated, *EGFR*-depleted H1975-Veh clones exhibited a significantly reduced colony-forming capacity (Figure 42). In contrast, EGFR knockout H1975-OsiR clones demonstrated a colony formation capability similar to that of the Renilla clone (Figure 42). These results indicate that H1975-Veh cells are dependent on EGFR for survival and proliferation, whereas H1975-OsiR cells have significantly lost their vulnerability against EGFR inhibition.

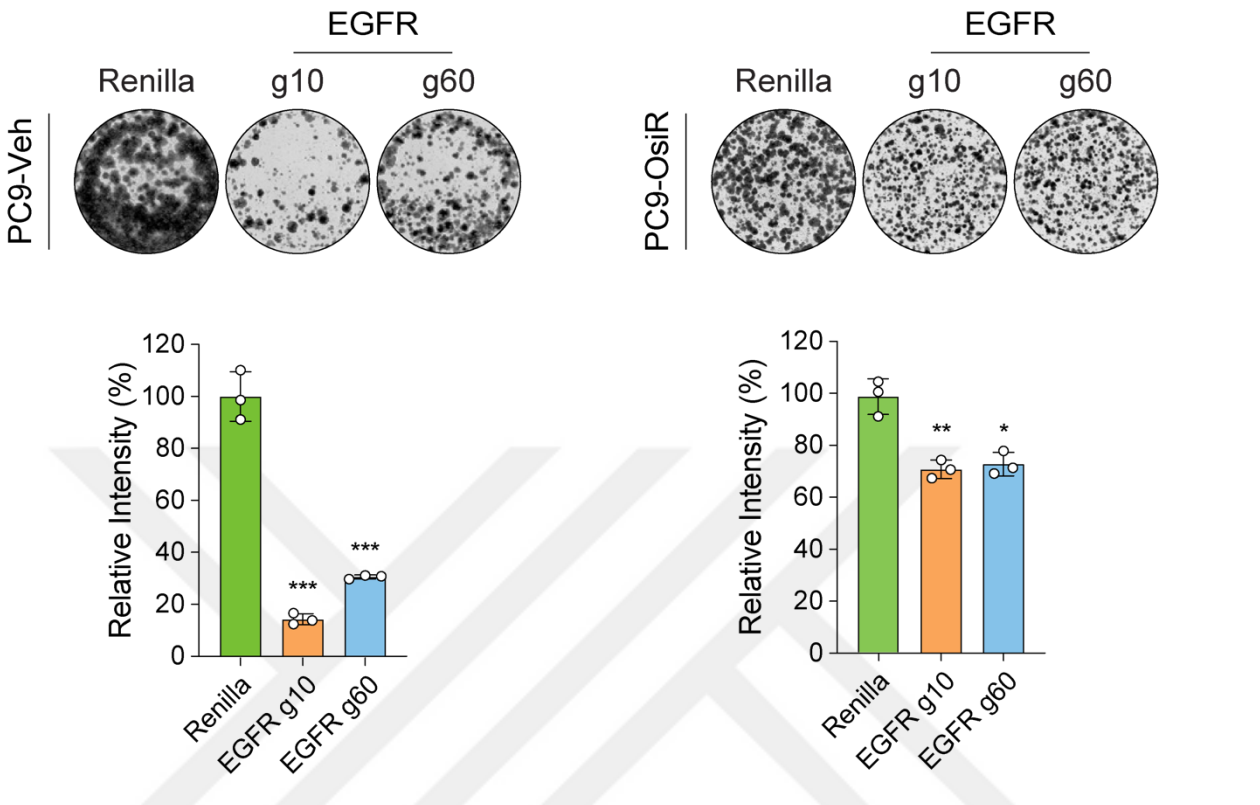

Figure 42: Colony formation assay results of Renilla and EGFR knockout H1975-Veh and H1975-OsiR cell lines. The relative intensity was determined by normalizing the intensities of the EGFR knockout group against those of the Renilla group. Mean ±SD, n=3.

4.17. Investigating the Mutation Profile of Osimertinib-resistant H1975 Cells

We then examined for secondary mutations that might contribute to osimertinib resistance using Sanger sequencing. Both H1975-Veh and H1975-OsiR cell lines were found to harbor the reported L858R and T790M mutations (Figure 43), with no additional mutations identified in the H1975-OsiR cells (Figure 43).

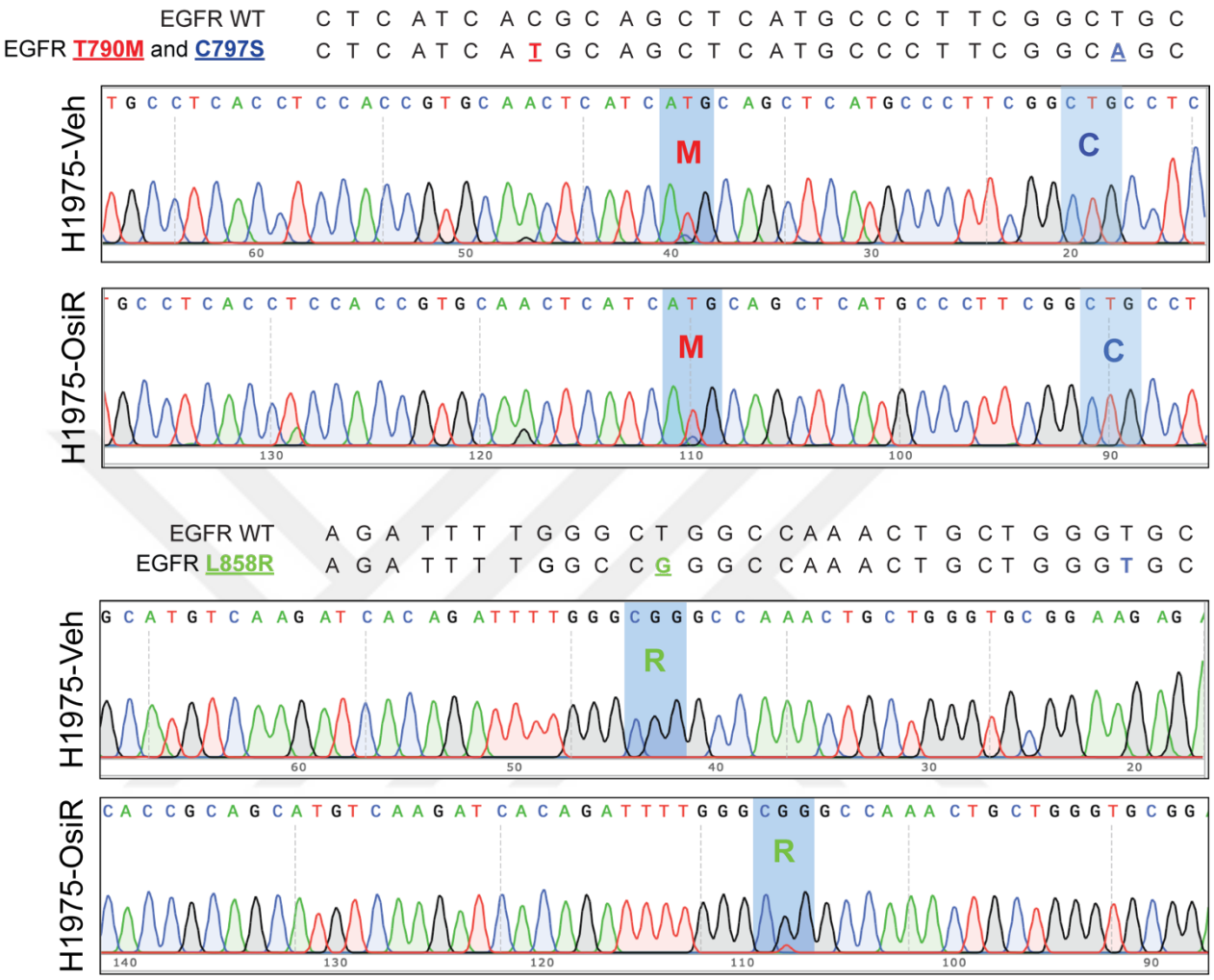

Figure 43: Sanger sequencing results for exon 20 and 21 depicting the T790M, L858R and C797X status in H1975-Veh and H1975-OsiR cells.

4.18. Impact of the Osimertinib-resistant State on Cell Proliferation and 2D Colony Formation Capacities in H1975 Cells

After confirming that the cells were resistant to osimertinib by IC50 calculation, growth kinetics were measured relative to the control group (Veh) in two separate assays as detailed previously. H1975-OsiR cells showed similar proliferation capacity compared to H1975-Veh cells (Figure 44).

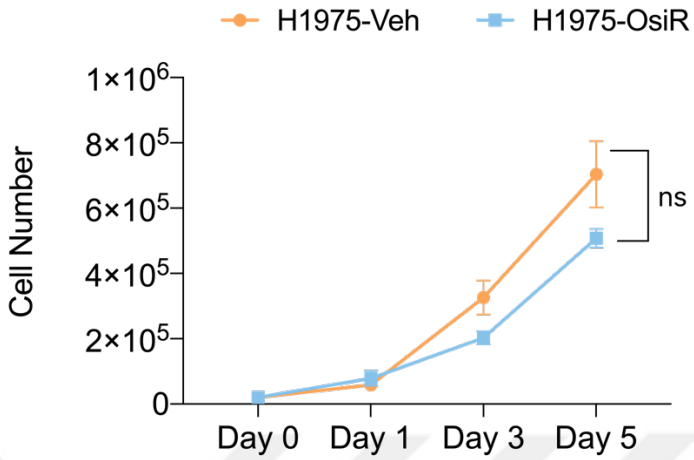

*Figure 44: Cell proliferation rates of H1975-Veh and H1975-OsiR cell lines. Cell counts were measured every 2 days starting 1 day after cell seeding. Mean±SD, n=2, ***p<0.001,*

2D colony formation assay was performed to determine how osimertinib resistant cell state affects colony-forming capacity the H1975-OsiR cell as indicated earlier. As a result, H1975-OsiR had slightly higher but not significant 2D colony formation capacity when compared to H1975-Veh cells (Figure 45). These findings indicate that H1975-OsiR cells have no effect on cell proliferation and colony-forming capacity after becoming resistant to osimertinib.

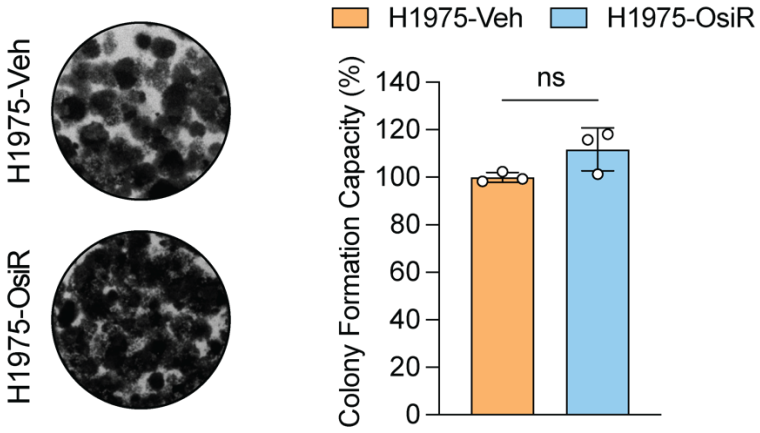

Figure 45: Clonogenic capacity of H1975-Veh and H1975-OsiR cell lines. Colony formation capacity was measured by normalizing the intensities of H1975-Veh cells to H1975-OsiR cells. Pixel intensities were

calculated with ImageJ software. Mean±SD, n=3, p=0.0936.

4.19. Effect of the Osimertinib-resistant State on Cell Invasion Capacity in H1975 Cells

After demonstrating the effects of osimertinib-resistant state to cell proliferation and colony formation rates, we sought to invasive phenotype of H1975-Veh and H1975-OsiR cells. For this purpose, invasion capacity of the cells was measured with transwell invasion assay. As a result, the analysis showed that H1975-OsiR cells have shown significantly increased invasion capacity compared to H1975-Veh cells (Figure 46). These results suggest that osimertinib-resistant cell state induced the invasive phenotype.

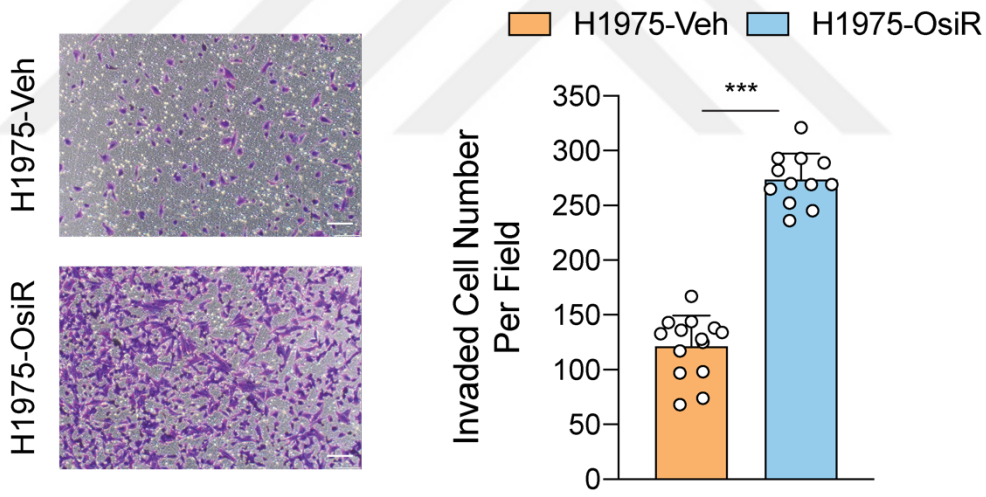

Figure 46: Representative images (left) and invasion capacity graph (right) of H1975-Veh and H1975-OsiR cells. Invaded cells were counted from randomly selected minimum 12 areas. 10X magnification, scale bar represents 100 µm.

4.20. Investigating the Response of the other generation and cytotoxic inhibitors

H1975 cells harbor the T790M mutation (Figure 43) and are resistant to first-generation EGFR-TKIs (109). In this context, MTT results showed that both H1975-Veh cells and

H1975-OsiR cells are resistant to Erlotinib. On the other hand, dacomitinib was insensitive to H1975-OsiR cells in similar dose ranges (Figure 47). These findings support the literature, indicating that H1975-Veh cells are resistant to first-generation EGFR-TKIs but sensitive to other-generation EGFR-TKIs and that H1975-OsiR cells may become resistant to other-generation EGFR-TKIs. In addition to previous-generation inhibitors, responses to Paclitaxel, a cytotoxic chemotherapy agent, were also investigated (Figure 47). When the results were evaluated, H1975-OsiR cells were observed to be slightly less sensitive to Paclitaxel than H1975-Veh. However, these low nanomolar IC50 values suggest that H1975-OsiR cells do not concomitantly develop significant resistance to chemotherapeutic agents and that Osimertinib-based resistance is primarily specific to

the EGFR pathway.

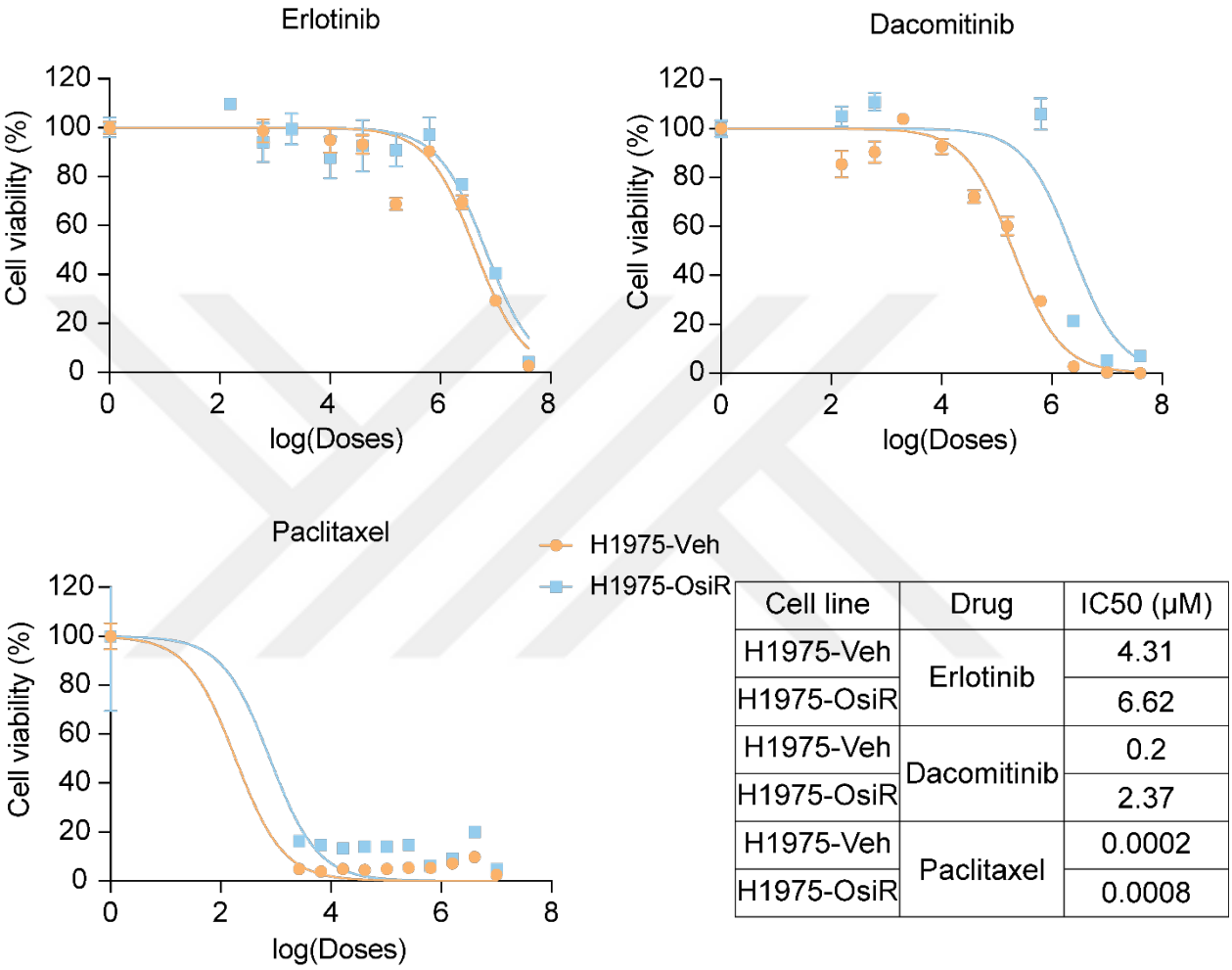

Cell line	Drug	IC50 (μM)
H1975-Veh	Erlotinib	4.31
H1975-OsiR		6.62
H1975-Veh	Dacomitinib	0.2
H1975-OsiR		2.37
H1975-Veh	Paclitaxel	0.0002
H1975-OsiR		0.0008

Figure 47: Cell viability graphs and IC50 values after 72 hours of Erlotinib, Dacomitinib and. Paclitaxel treatment in H1975-Veh and H1975-OsiR cells. Treatments were normalized to DMSO (vehicle) control, n=6.

4.21. Characterizing Morphological Changes in Osimertinib-resistant H1975 Cells

In H1975-OsiR cells, axon-like cell protrusions are to investigate this phenotype, we performed three different assays using the most well-known EMT markers, E-cadherin (E-cad) as an epithelial marker and Vimentin (Vim) as a mesenchymal marker gene. Firstly, the relative expression levels of these genes with qRT-PCR. The results suggested that

the expression of the CDH1 gene encoding E-cadherin significantly reduced in the H1975-OsiR, while the expression of Vimentin increases approximately 2-fold (Figure 48).

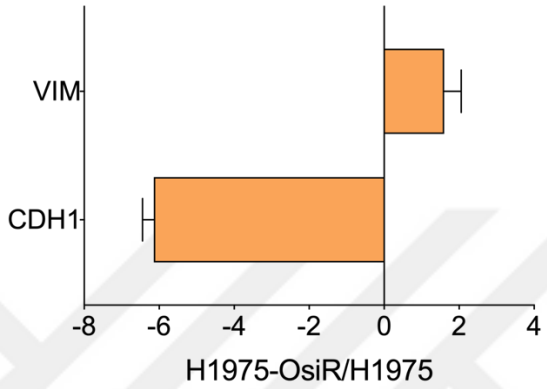

Figure 48: qPCR results for EMT marker genes in H1975-Veh and H1975-OsiR cells.

Secondly, changes in EMT markers in cells were investigated by western blot method. As shown in Figure 49, significant reduction observed in E-cadherin expression in H1975-OsiR cell line, however Vimentin increased significantly when shifting to osimertinib-resistant cell state.

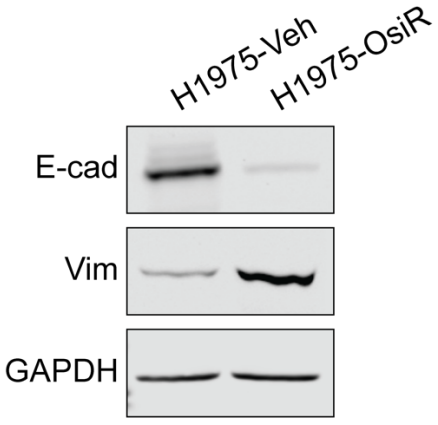

Figure 49: Western blot results for E-cadherin and Vimentin in H1975-Veh and H1975-OsiR cells. B-actin used as loading control.

Finally, IF staining was performed in the cells. As shown in Figure 50, consistent with previous qPCR and western blot results, H1975-Veh cells expressed high levels of E-cadherin while H1975-OsiR cells showed decreased E-cadherin expression, while H1975-Veh cells expressed low levels of Vimentin while H1975-OsiR cells expressed high levels of Vimentin. These results indicated that H1975-OsiR cell line shows EMT phenotype.

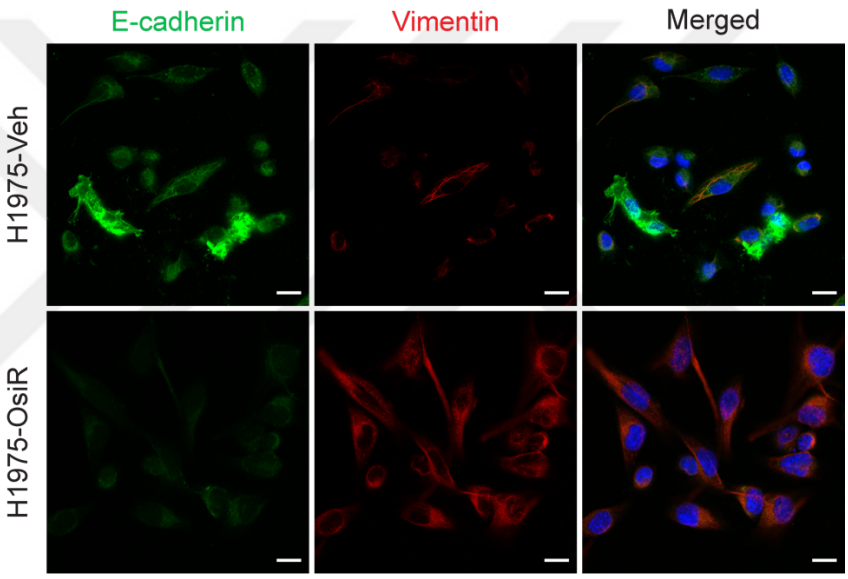

Figure 50: E-cadherin and Vimentin staining in H1975-Veh and H1975-OsiR cells. DAPI is used as a counterstain dye.

4.22. Exploring Alterations in Bypass Signaling Pathways in Resistant Cells

Next, alterations in EGFR signaling pathway were investigated as described previously. In comparison to H1975-Veh cells, a significant decrease was detected in the endogenous phosphorylation rates of EGFR at the Tyrosine 1068 position in the H1975-OsiR cells as well. However, an increase was observed in the phosphorylation of AKT at the Serine 473 position, one of the downstream signals of EGFR and slight increase was found in the activity of the ERK pathway. On the other hand, no change was observed in the p-STAT protein, which is also contribute to bypass signaling pathways (Figure 51). This data

reveals that endogenous EGFR activity is significantly reduced with the of osimertinib resistant state of the cell, whereas AKT signaling activity from the downstream pathway is significantly increased and ERK signaling is slightly increased. This suggests that the dependence on EGFR activity in H1975-OsiR cells shifts to the AKT axis via an alternative upstream pathway, while there is also increased activity in the ERK axis.

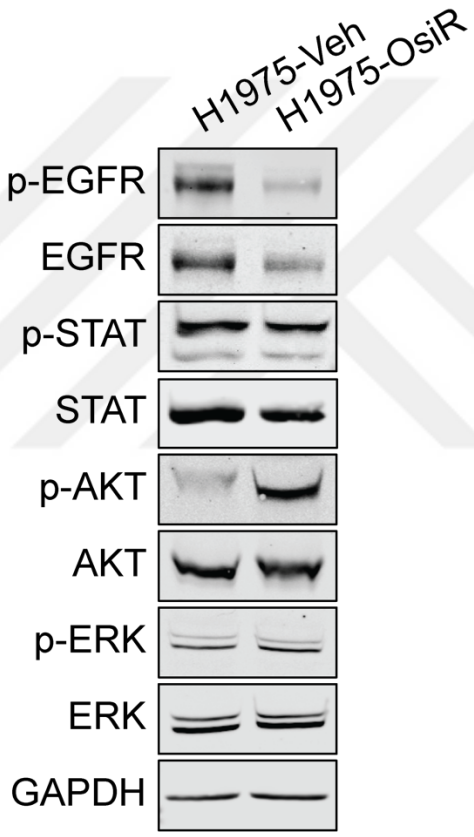

Figure 51: Western blot result showing alterations in bypass signaling pathways in H1975-Veh and H1975-OsiR cells. B-actin used as loading control.

4.23. Effect of Increasing Osimertinib Doses on Colony Formation Capacity in H1975-OsiR and H1975-Veh Cells

Long-term osimertinib responses were investigated in H1975-Veh and H1975-OsiR cell line by 2D colony formation assay with the same experimental setup detailed above.

These results show that, as expected, H1975-Veh cells responded strongly with a significant decrease in colony formation capacity with increasing osimertinib doses, while H1975-OsiR cells were not affected by the different osimertinib doses (Figure 52).

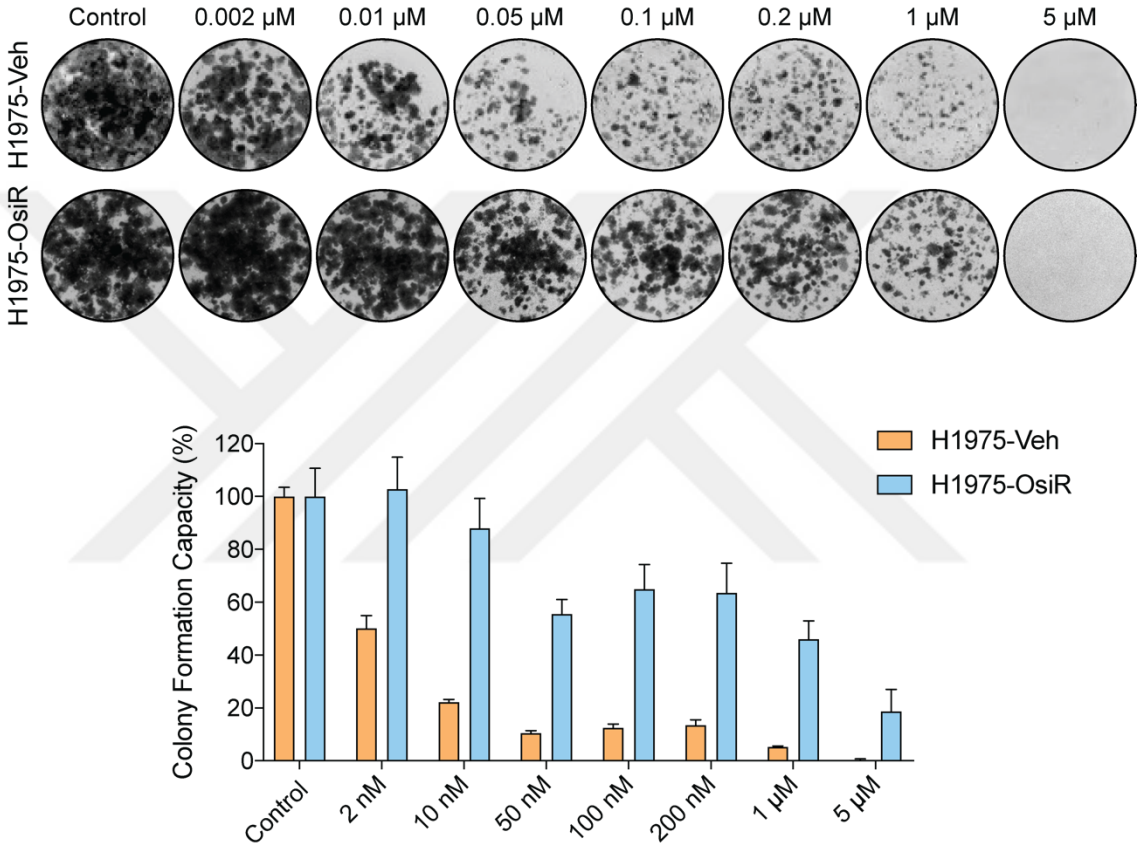

Figure 52: Colony formation capacity of H1975-Veh and H1975-OsiR cells at different drug doses after the development of resistance. Representative images are given. Mean ±SD, n=3, technical replicates.

4.24. Impact of Increasing Osimertinib Doses on Proliferation Index and Growth Kinetics in H1975-OsiR and H1975-Veh Cells

The effect of increasing osimertinib dose on proliferation and growth pattern BrdU labeling and cell cycle assays were performed with same experimental setups in PC9 group. Our findings showed that the proliferation index of H1975-Veh cells decreased significantly in

the presence of increasing osimertinib doses, while it did not cause any change in H1975-OsiR cells (Figure 53).

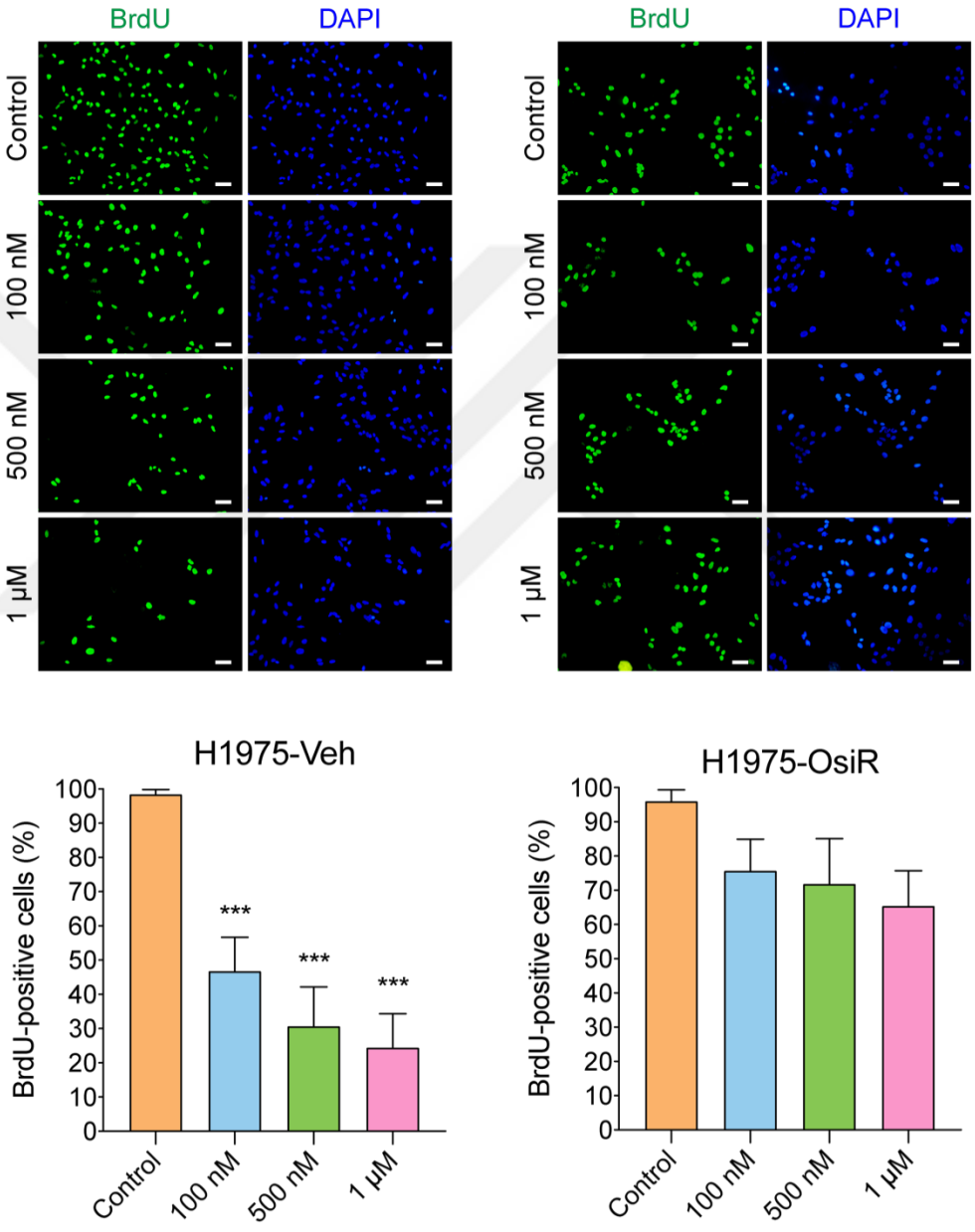

Figure 53: BrdU labeling results of H1975-Veh and H1975-OsiR cells with increasing doses of osimertinib. Mean ± SD, n=8.

Next, cell cycle profiles were examined. As shown in Figure 54, while G1 phase arrest was observed in H1975-Veh cells with increasing osimertinib dose, no change in cell cycle profile was observed in H1975-OsiR. The findings indicate that H1975-OsiR cells was unresponsive to different doses of osimertinib. On the other hand, H1975-Veh cells were very responsive to osimertinib.

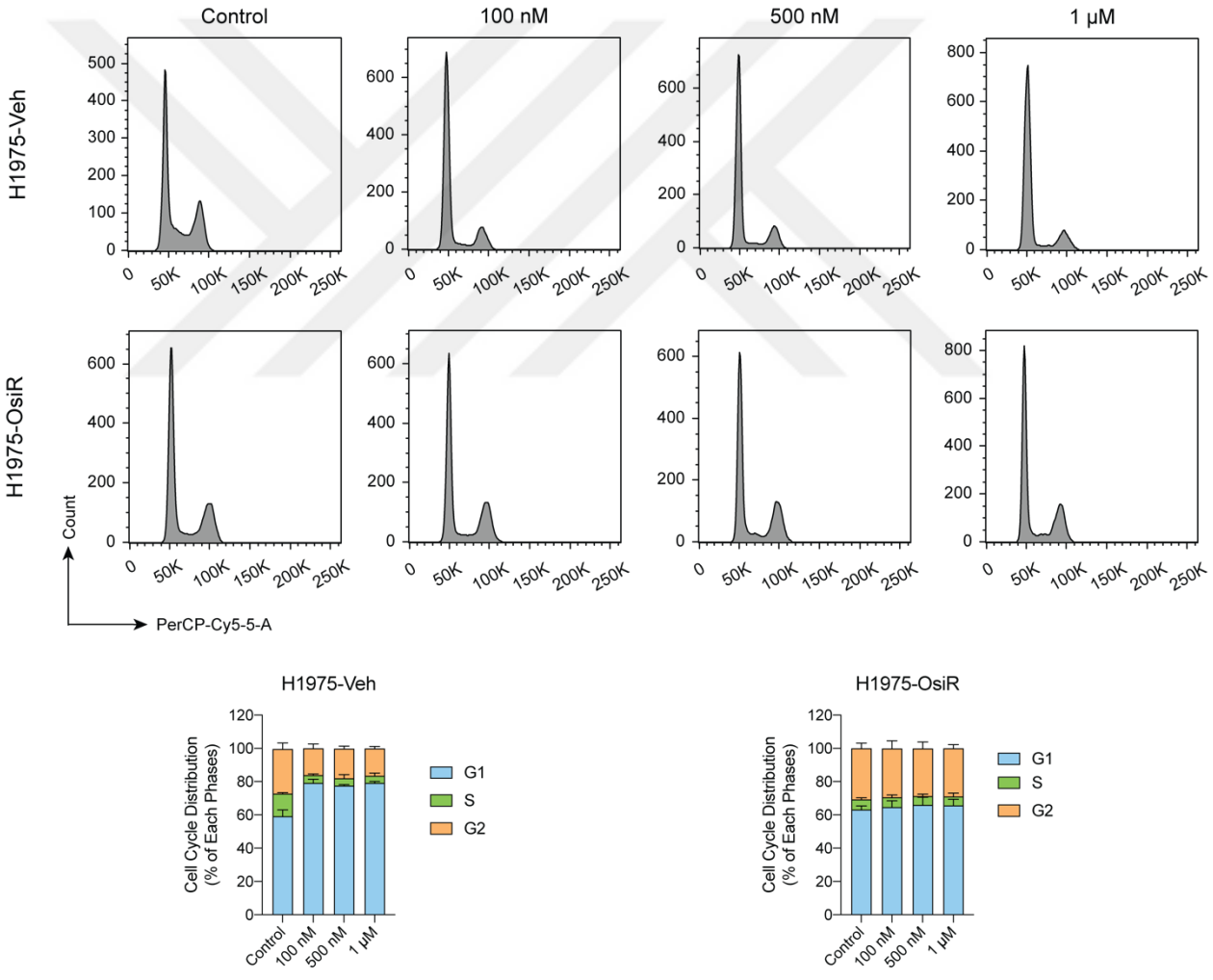

Figure 54: Cell cycle distribution of H1975-Veh and H1975-OsiR cells with increasing osimertinib concentrations. n=3, biological replicates.

4.25. Bypass Signaling Pathways Changes in H1975-OsiR and H1975-Veh Cells in Response to Escalating Osimertinib Doses

To investigate the effect of increasing osimertinib doses on the EGFR signaling pathway, same experimental procedure described previously was followed. As expected, increasing osimertinib doses significantly inhibited p-EGFR, p-AKT and p-ERK in PC9-Veh cells. On the other hand, a decrease in phosphorylation signals in p-EGFR and pERK was observed in PC9-OsiR, but no significant change was found in the activity of the AKT pathway when osimertinib doses were increased. These results indicate that endogenous EGFR activity was significantly reduced by increasing osimertinib doses in PC9-OsiR cells, whereas AKT signaling activity from the downstream pathway did not change (Figure 55). This indicated that AKT axis activity did not change with increasing doses confirms the results given in 4.22 and shows that the cell's dependence on EGFR has shifted to AKT. Finally, it is suggested that the dependence on EGFR activity of the PC9-OsiR persisted, but this had no effect on resistance.

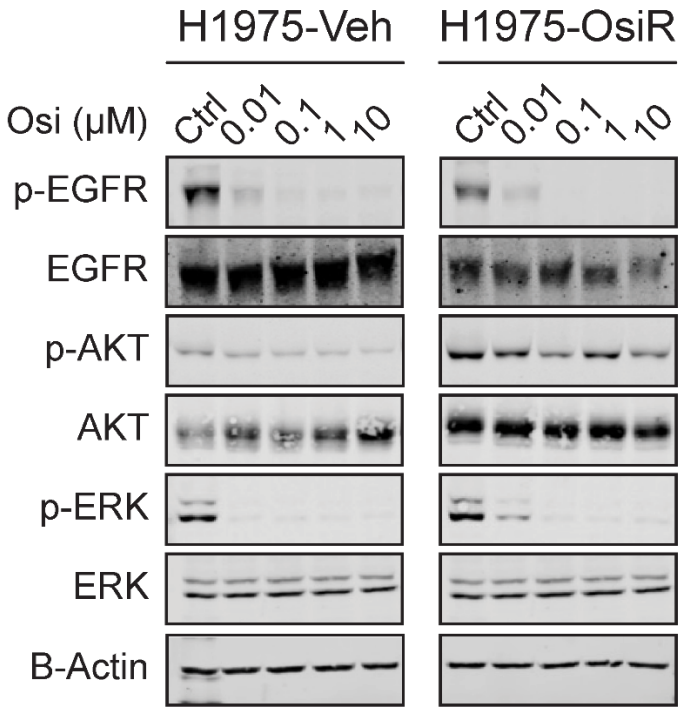

Figure 55: Western blot analysis showing alterations in EGFR pathway components in accordance with

increased doses of osimertinib in H1975 group , β-actin was used as a loading control.

4.26. Transcriptomic Profiling of Osimertinib-Resistant H1975 Cells

Whole-genome transcriptome analysis was conducted on H1975-Veh and H1975-OsiR cells. The initial step in RNA sequencing analysis involved assessing the overall similarity/distinction between the samples in this context, our data were analyzed using principal component analysis (PCA). A distinct biological separation between the two groups was evident along the PC1 axis (Figure 56). The technical variance between replicates was minimal, as indicated by the limited separation along the PC2 axis. Additionally, the separation between the groups and the consistency among the triplicate replicates were further illustrated through a correlation heatmap (Figure 56).

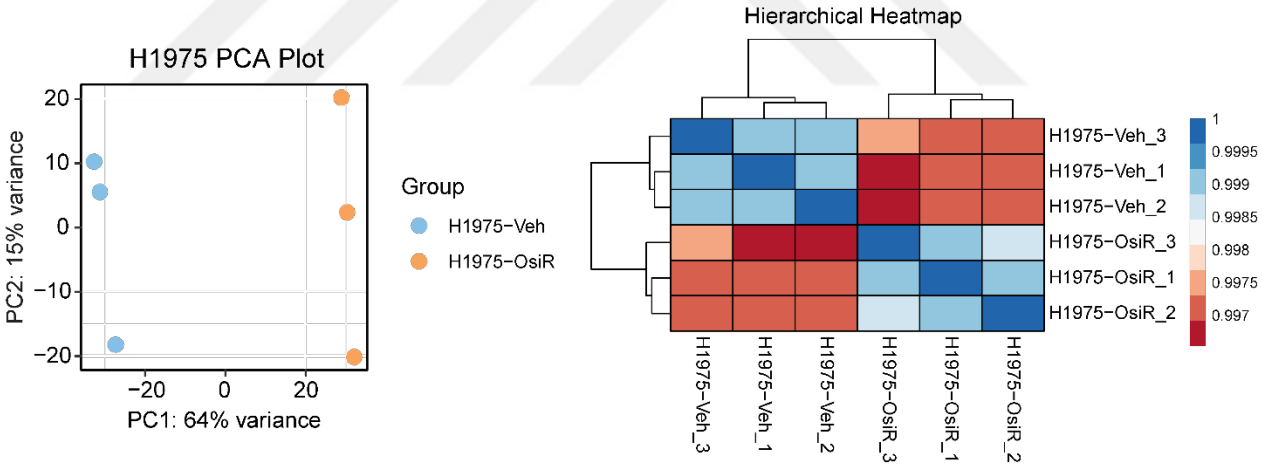

Figure 56: Principal Component Analysis (PCA) plot (left) and correlation heatmap (log2(CPM+1)) (right) of H1975-Veh and H1975-OsiR triplet repeats.

Next, the statistical significance of the differences in gene expression levels between the H1975-Veh and H1975-OsiR groups was determined. Genes exhibiting statistically significant differential expression were identified and ranked according to the corrected p-value (FDR). Various visualizations were generated to represent the gene clusters with significant changes. Specifically, a heatmap displaying a total of 15,005 transcripts with

CPM values of 1 or higher was created using triplicate samples from both groups Figure 57.

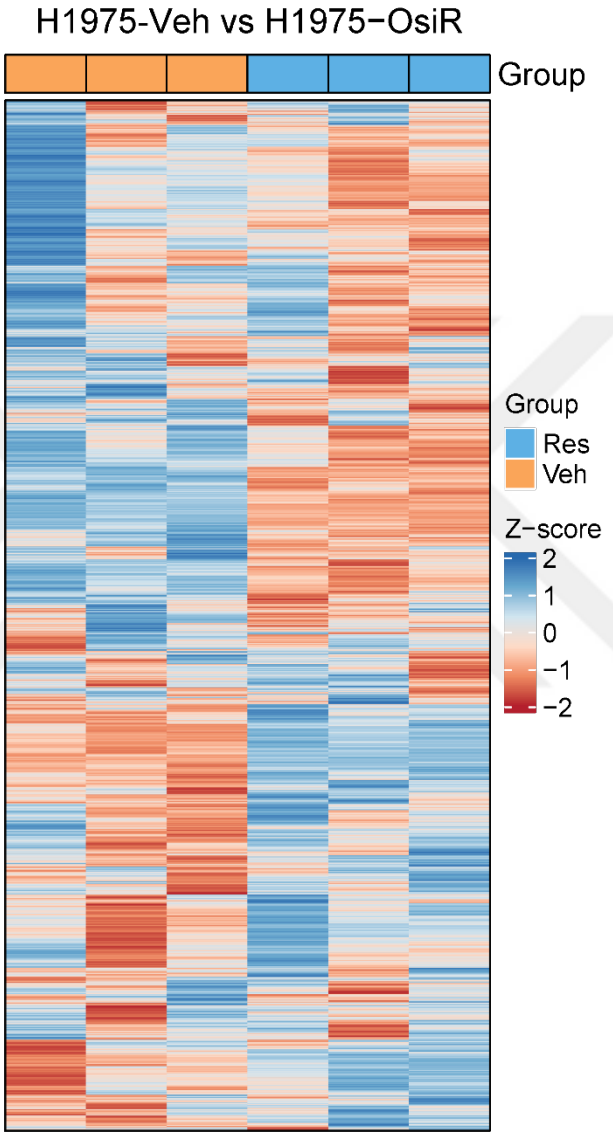

Figure 57: Heatmap of all transcripts that passed the log_2(CPM+1) filter in H1975 group , n=3 for each sample. A total of 15,005 transcripts passed.

An MA plot was generated to visualize gene expression changes between H1975-Veh and H1975-OsiR cells (Figure 58). In this plot, the X-axis represents the mean expression

level (A, logCPM) of each gene, while the Y-axis depicts the log2 fold change (M, logFC) between the two conditions.

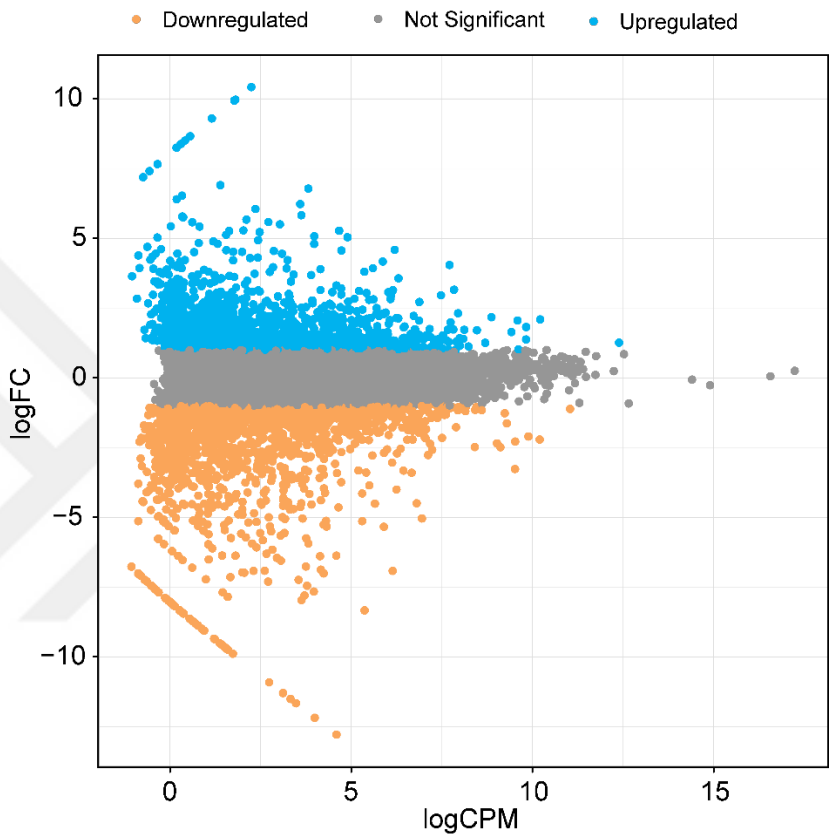

Figure 58: MA plot showing the alterations in gene expression profile for H1975 group. LogFC threshold value is <-1 and >1. The number of genes with increased expression (blue) exceeding this threshold is 1462, while the number of genes with decreased expression (orange) is 1746. The genes shown in gray dots are genes with insignificant expression.

As an additional method for representing gene expression changes between H1975-Veh and H1975-OsiR cells, a volcano plot was created (Figure 59). This plot visualizes genes with large fold changes and statistical significance, combining both the magnitude of change and the significance level in a single graphical representation.

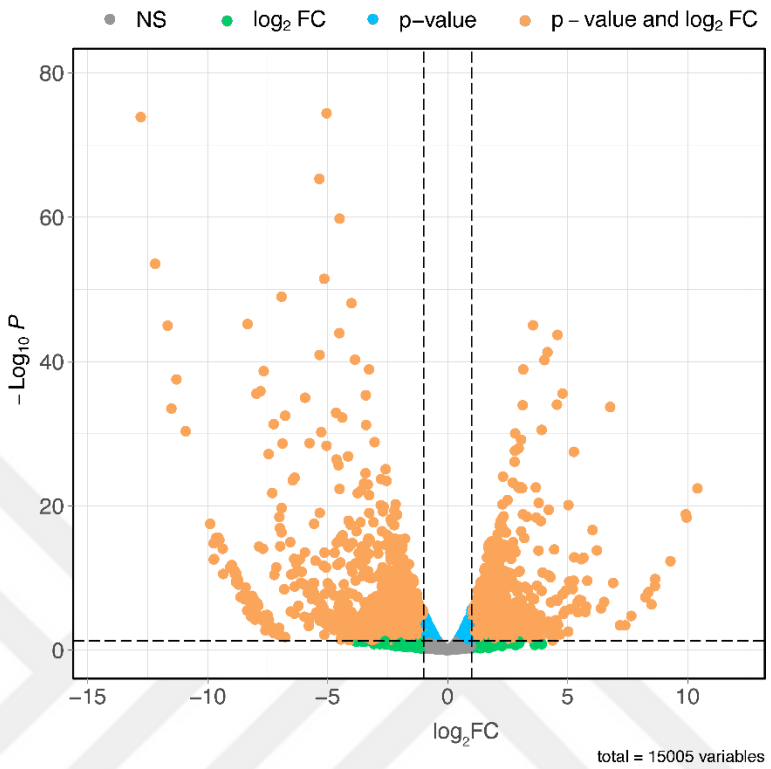

Figure 59: Volcano plot demonstrating the changes in gene expression profile for H1975 group. Log₂FC threshold value is <-1 and >1. p-value threshold is <0.05. The number of genes with altered expression exceeding these thresholds (orange) is 2528.

4.27. Functional Insights from Transcriptomic Analysis of Osimertinib-Resistant H1975 Cells

After revealing the changes in the global transcriptome, gene ontology (GO), pathway enrichment and Gene Set Enrichment Analysis (GSEA) were performed to better understand which pathways and/or phenotypes these changes affect. For gene ontology and pathway enrichment analyses, gene lists were divided into two different gene list groups as “up” and “down” using an absolute value threshold of 1. The genes in these lists were analyzed using GO, KEGG and ReactomePA databases. The terms showing significant changes as a result of these analyses are presented with dot plots in Figures X and Y.

The enrichment analysis shown in Figure 60 revealed processes that demonstrate the presence of the EMT phenotype observed in H1975-OsiR cells. In particular, biological processes such as extracellular matrix organization and external structure organization stand out as terms explaining this phenotype. In addition, ERK activation emerged as an alternative bypass signaling pathway in H1975-OsiR cells. Interestingly, although ERK phosphorylation was increased in characterization experiments compared to H1975-Veh cells, less phosphorylation was observed compared to AKT. However, AKT activation did not emerged as an enriched term. Similar to PC9-OsiR cells, IGFBP and TNF pathways were enriched in upregulated genes in H1975-OsiR cells. Also, TGF-B and NFKB signaling pathways were enriched in upregulated genes.

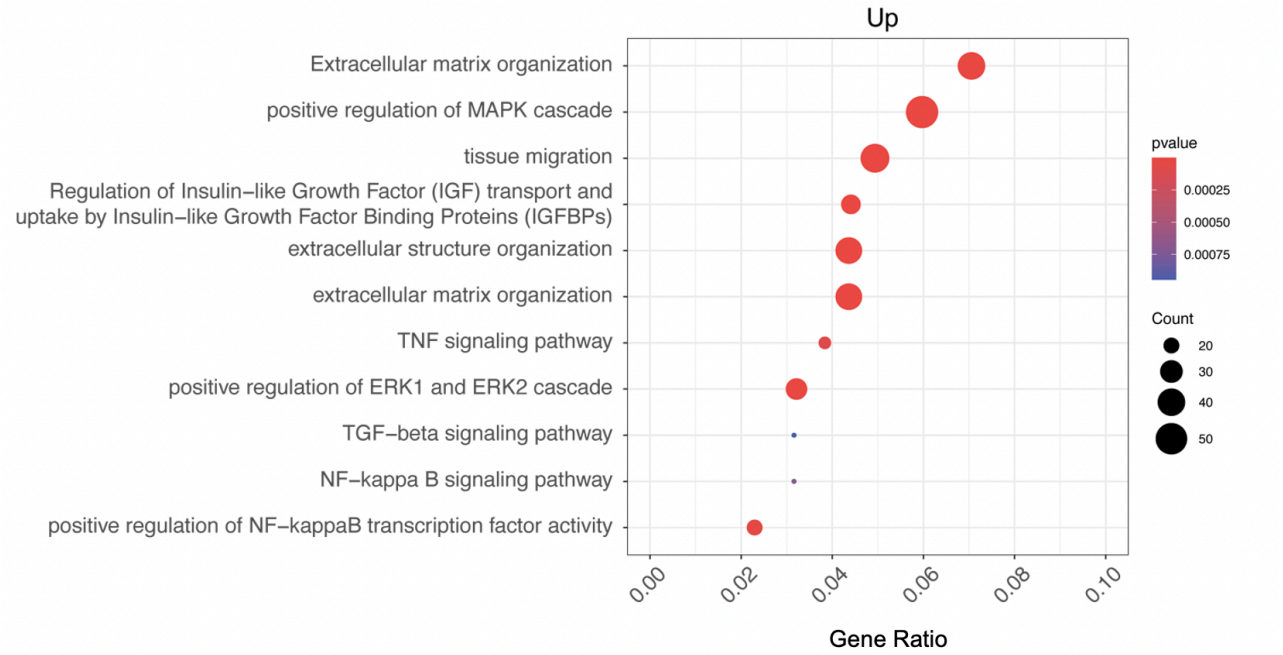

Figure 60: Enrichment analysis for upregulated genes in H1975-OsiR.

GSEA was also performed to better understand the distinction between the two biological states. In H1975-OsiR cells, the gene set characterized by the EMT phenotype was at the top of the list and showed a significant difference. As shown in Figure 61, in line with

previous result described above gene sets enriched in the resistant state includes IL6/JAK/STAT3 signaling gene set was significantly enriched. As depicted in Figure 61, gene sets indicating increased migration capacity was enriched in H1975-OsiR cells These findings are consistent with the results from characterization experiments. On the other hand, these results suggested that the top-ranked gene sets are consistent with the characterization experiment results of sensitive cells and are also consistent with the biology of the cell.

Enriched in resistant state:

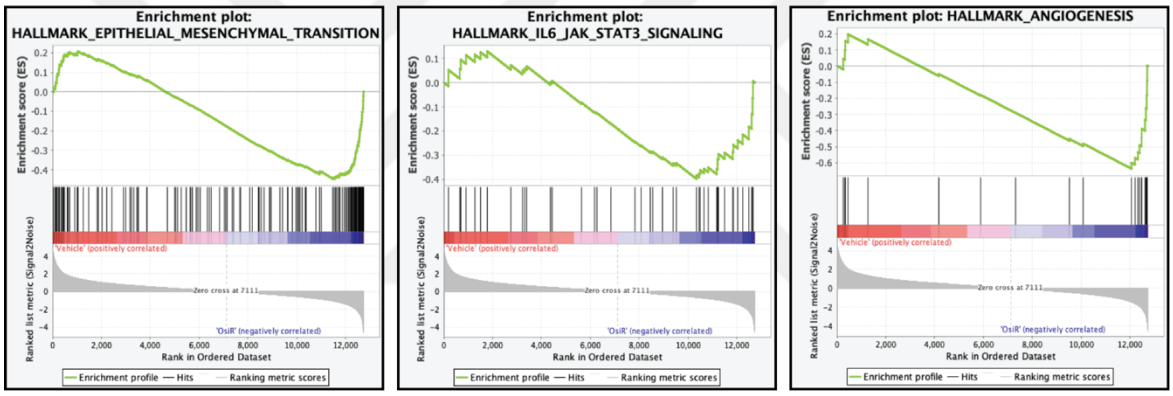

Enriched in sensitive state:

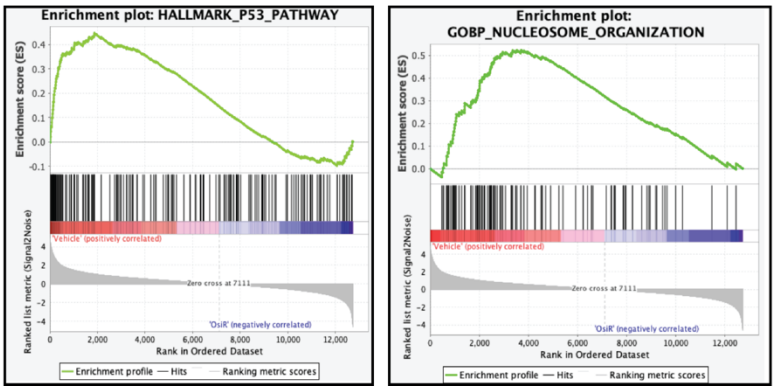

Figure 61: Selected gene sets from GSEA of H1975 cell line.

5. DISCUSSION

Lung cancer accounts for the highest number of deaths from cancer globally (110). It is also the second most diagnosed cancer type each year (3). NSCLC is the histological subtype of lung cancer, accounting for 85% of all lung cancer cases (10). NSCLC is categorized into three main histological subtypes: lung adenocarcinoma, squamous cell carcinoma, and large cell carcinoma. Lung adenocarcinoma is the most prevalent type in patients (10,37). Driving mechanisms lead to the carcinogenesis and progression of lung adenocarcinoma, and the most common mechanisms are activating mutations in the EGFR and KRAS genes (12).

The *EGFR* gene is a tyrosine kinase receptor that regulates many different signaling pathways in the cell (19). Driver mutations that increase the activity of this receptor contribute to the aggressiveness of the tumor phenotype not only in lung cancer but also in other types of cancer (34). Among these, L858R and exon 19 deletion are the most widely observed EGFR-activating mutations (38). As a result of these mutations, *EGFR* is constitutively activated in the cell and continuously activates downstream signaling pathways such as AKT, ERK and STAT (37). Consequently, upon activation, cells continue to survive, proliferate and migrate, thus acquiring an aggressive phenotype (40). Various treatment options are available for the patients however, EGFR-targeted treatments are the standard of care in EGFR-mutated NSCLC patients (92). In this context, EGFR-TKIs have been developed to inhibit constitutively active EGFR. They form covalent bonds with the ATP binding site of EGFR and block it from inducing the downstream signaling pathways (52).

Initially, first-generation EGFR-TKIs, erlotinib and gefitinib, were developed. They bind reversibly to the tyrosine kinase domain of EGFR. Although they have significantly prolonged the survival of patients in clinical use, most patients develop resistance during continued drug therapy. The most common mechanism of resistance to first-generation

EGFR-TKIs is the T790M secondary mutation, which alters the structure of the tyrosine kinase domain of EGFR, preventing the binding of small molecule inhibitors (37,53,58,68,111). Second-generation EGFR-TKIs, dacomitinib and afatinib, were developed to target this mutation and overcome resistance. Although these drugs have shown promising results in patients, side effects and irregularities in drug dosage have limited their use in the treatment of NSCLC (53,66,112,113). Therefore, third-generation EGFR-TKIs were developed. Third-generation EGFR-TKIs are inhibitors that can specifically inhibit both activating mutations and the T790M secondary resistance mutation, while having no effect on wild-type EGFR. Among these inhibitors, osimertinib is currently the only FDA-approved third-generation EGFR-TKI (72,77,79,105).

Osimertinib is the only third-generation EGFR-TKI that is approved by FDA. Osimertinib was initially approved as a second-line treatment for the T790M mutation after first-generation EGFR-TKIs and was subsequently approved for first-line treatment based on clinical results. A significant increase in progression-free survival rates is observed with line of treatments. However, as with other EGFR-TKIs, resistance to osimertinib is inevitable. Patients develop resistance to osimertinib after 11-19 months, depending on the line of treatment (11,61,87,91). The literature states that different mechanisms are involved in acquired resistance to osimertinib. These mechanisms are divided into two classes: EGFR-dependent and independent mechanisms. EGFR-dependent mechanisms involve secondary or tertiary mutations in EGFR. The most predominant one of these is the C797X missense mutation, which prevents osimertinib from covalently binding to the ATP-binding site. On the other hand, EGFR-independent mechanisms include gene fusions, amplification of other receptor kinases or genes that activate downstream signaling pathways (34,37,78,114).

In this study, we aimed to develop osimertinib-resistant cell models and characterize these models in detail, with the aim of better understanding osimertinib resistance in NSCLC. For this purpose, firstly osimertinib resistant sublines with two different EGFR mutation

profiles were developed. Then, these cell models were characterized at the cellular level to investigate changes in morphology, cell proliferation, colony formation capacity, cell cycle and invasion capacity. Then, changes in signaling pathways at the protein level were examined. Finally, high-throughput RNA sequencing was performed to reveal the transcriptomic profile associated with osimertinib resistance and to determine differential gene expression profiles.

Osimertinib resistant PC9 and H1975 cell lines were developed. Responses to osimertinib were measured in these cells using the MTT assay. As a result, IC50 values for PC9 were calculated as approximately 1 nM for PC9-Veh and 3.5 μM for PC9-OsiR cells, while for H1975, IC50 values were calculated as 6.18 nM for H1975-Veh and 2.24 μM for H1975-OsiR cells. It was then tested by CRISPR/Cas9-mediated knockout method that parental cells harboring active EGFR are dependent on EGFR for survival, while osimertinib resistant cells lose this dependency. As a result of EGFR gene knockout, the colony-forming capacity of both PC9-Veh and H1975-Veh cells was significantly reduced, whereas PC9-OsiR and H1975-OsiR cells were unaffected by this change, indicating that the EGFR dependency of osimertinib-resistant cells was significantly reduced. Then, mutation profiles in both cell lines were examined by Sanger sequencing. As a result, both cell lines were confirmed for the reported mutations and no other mutations were detected. Therefore, it was concluded that osimertinib resistance is not mediated by secondary or tertiary mutations in the EGFR.

In the characterization phase, firstly the growth kinetics of the cells were measured. In accordance with the study of Nishihara et al., PC9-Veh cells proliferated faster than PC9-OsiR cells but had similar colony formation capacity, while H1975-Veh and H1975-OsiR cells showed similar growth kinetics in both properties. The invasive capacity of the cells was investigated and PC9-OsiR cells showed decreased invasive capacity compared to the PC9-Veh group. H1975-OsiR cells showed increased invasiveness compared to the H1975-Veh group, consistent with the literature (115). To demonstrate that osimertinib-

resistant cells may also develop resistance to previous EGFR-TKIs, responses to other-generation drugs were measured. Our results showed that PC9-Veh cells were sensitive to both Erlotinib and Dacomitinib, while PC9-OsiR cells were resistant to these inhibitors. On the other hand, in line with the literature, the H1975 cell line harboring the T790M mutation has been shown to be resistant to Erlotinib in both cases (116). As for the second-generation EGFR-TKIs, our results showed that H1975-Veh cells are sensitive to Dacomitinib, while H1975-OsiR cells are resistant to this inhibitor. Additionally, we assessed the response of all cells to the cytotoxic chemotherapy agent Paclitaxel. In both cell lines, resistant cells showed slightly less sensitivity to Paclitaxel compared to control cells. However, IC50 values for Paclitaxel were measured at low nanomolar levels, indicating that osimertinib resistance primarily affects the EGFR pathway and does not result in significant cross-resistance to chemotherapeutic agents.

EMT is known to be osimertinib resistance mechanism in the literature (PMID: 31564718). Our cells showed cell protrusions in their morphology. PC9-OsiR cells showed slight cell protrusions morphologically and this was investigated by various methods. qPCR results revealed a significant increase in Vimentin (mesenchymal marker) gene expression, but this increase was not detected when checked at the protein level. These results indicated that the morphological changes in the PC9 cell line may be an EMT phenotype, but E-cadherin and Vimentin genes do not directly play a role in its regulation. On the other hand, a decrease in the E-cadherin gene and an increase in the Vimentin gene were observed in H1975 cells, both at the gene expression and protein level, which can be directly associated with the EMT phenotype. As cells become resistant, the signal in the EGFR pathway shifts to which pathway after osimertinib blockade has been investigated. In this context, it has been shown that resistance shifts to the AKT pathway in both PC9-OsiR and H1975-OsiR cell lines. As cells become resistant, the signal in the EGFR pathway is shifted to which pathway after osimertinib blockade. In this context, it was shown that resistance shifted to the AKT pathway in both PC9-OsiR and H1975-OsiR cell lines. Furthermore, cells treated with increasing doses of osimertinib showed that the AKT

pathway was unresponsive at increasing doses, suggesting that the shift and maintenance of the EGFR response to the AKT pathway plays an important role in the regulation of resistance in both cell lines. In osimertinib resistance, as is frequently observed in the literature, a shifting to the AKT pathway is observed in osimertinib-resistant cell models (37).

To evaluate the effect of osimertinib on phenotypic and cellular properties, cell proliferation, cell cycle and motility tests were performed in both cells using increasing doses of osimertinib. Cell proliferation index was tested by BrdU incorporation analysis. As a result, no change was observed in cell proliferation indices in the presence of increasing doses of osimertinib in both PC9-OsiR and H1975-OsiR. Then, cell cycles of the cells were tested with the same experimental approach and no response to osimertinib was observed in the cell cycle profiles of resistant cells. Finally, the motility of the cells was analyzed for cellular characterization. In this phenotype analysis, no effect was observed in the motility of PC9-OsiR cells in the presence of osimertinib. On the other hand, PC9-Veh cells responded to osimertinib and a significant decrease in cell motility was observed. Wound healing assay mediated motility test could not be performed in H1975-OsiR cell lines because the cells were not suitable for the assay due to the extreme mesenchymal phenotype shift of the cells.

To reveal transcriptomic landscapes of both osimertinib-resistant cell lines, RNA-sequencing was performed. According to the results both sublines showed distinct biological separation between the two groups. These findings suggest that as cells develop resistance to osimertinib, they undergo significant changes in their global transcriptome. This extensive reprogramming of the gene expression profile suggests an adaptation in which the cellular response to osimertinib resistance involves an extensive reprogramming of gene expression. This adaptation has been shown to promote survival and growth in cells despite ongoing osimertinib treatment.

As a result of GO and pathway enrichment analyses, findings confirming the phenotype and character of both osimertinib-resistant cell lines. In addition, other pathways associated with osimertinib resistance in the literature were also observed in the analysis results. Among these pathways, pathways involving IL6 and IGFBP proteins were prominent as a result of gene set enrichment analyses in both H1975 and PC9 cells. Literature review revealed that there were studies showing that osimertinib resistance increased in IL6-induced PC9 and H1975 cell lines (117). In addition, in another study using cells with the T790M mutation, it was shown that pathways involving IGF1R and IGFBP3 proteins regulated osimertinib resistance (118). These findings show that the obtained osimertinib-resistant cells are compatible with the models defined in the literature.

6. CONCLUSION AND FUTURE PERSPECTIVES

The aim of this thesis project was to develop osimertinib-resistant NSCLC cell lines to comprehensively investigate the mechanisms of osimertinib resistance. For this purpose, NSCLC cell lines with two different mutational profiles were characterized by various approaches. Characterization of the osimertinib resistant cell models generated showed similarities with the other models in the literature, but at the same time they were quite different. For this reason, a gene family or signaling pathway that commonly regulates osimertinib resistance could not be identified in our study. Although this finding is not very surprising considering the information in the literature, it reveals that we have developed unique osimertinib-resistant cellular models. These developed models are currently being used in our laboratory within the scope of another TUBITAK project aimed at investigating the mechanisms regulating osimertinib resistance. In addition, these cells are being used in another study, the manuscript process of which is ongoing, aiming to uncover synthetic lethal interactions regulated by epigenetic and transcriptional factors underlying osimertinib resistance.

In the future, we plan to perform CRISPR-Cas9 knockout screening using a kinome library of 763 kinases, together with these resistant cell models and another resistant cell model, HCC827-OsiR, developed in our laboratory. As a result, we aim to reveal the kinases that regulate resistance.

In addition to kinome screening, we also plan to employ transcriptomic and epigenomic profiling approaches, such as ChIP-seq and ATAC-seq, to identify potential transcriptional and chromatin regulators of osimertinib resistance. By integrating the data from these diverse omics platforms, we hope to gain deeper insights into the regulatory networks that contribute to resistance. Furthermore, these findings could provide valuable information for the development of combination therapies aimed at overcoming resistance by targeting alternative mechanisms. In conclusion, this study will enable the development of new treatment methods by providing better treatment options for NSCLC patients who develop resistance to osimertinib. Additionally, we can mimic clinical scenarios more specifically using PDX models. Integrating our cell models into clinical studies may significantly contribute to improving treatment and testing strategies.

7. REFERENCES

1. Sung H, Ferlay J, Siegel RL, Laversanne M, Soerjomataram I, Jemal A, et al. Global Cancer Statistics 2020: GLOBOCAN Estimates of Incidence and Mortality Worldwide for 36 Cancers in 185 Countries. CA Cancer J Clin. 2021 May;71(3):209–49.

2. Ferlay J, Colombet M, Soerjomataram I, Parkin DM, Piñeros M, Znaor A, et al. Cancer statistics for the year 2020: An overview. Int J Cancer. 2021 Apr 5;

3. Siegel RL, Giaquinto AN, Jemal A. Cancer statistics, 2024. CA Cancer J Clin. 2024;74(1):12–49.

4. Polanco D, Pinilla L, Gracia-Lavedan E, Mas A, Bertran S, Fierro G, et al. Prognostic value of symptoms at lung cancer diagnosis: a three-year observational study. J Thorac Dis. 2021 Mar;13(3):1485–94.

5. Duma N, Santana-Davila R, Molina JR. Non-Small Cell Lung Cancer: Epidemiology, Screening, Diagnosis, and Treatment. Mayo Clin Proc. 2019 Aug;94(8):1623–40.

6. Araghi M, Mannani R, Heidarnejad Maleki A, Hamidi A, Rostami S, Safa SH, et al. Recent advances in non-small cell lung cancer targeted therapy; an update review. Cancer Cell Int. 2023 Aug 11;23(1):162.

7. Gridelli C, Rossi A, Carbone DP, Guarize J, Karachaliou N, Mok T, et al. Non-small-cell lung cancer. Nat Rev Dis Primers. 2015 May 21;1:15009.

8. Zappa C, Mousa SA. Non-small cell lung cancer: current treatment and future advances. Transl Lung Cancer Res. 2016 Jun;5(3):288–300.

9. Govindan R, Page N, Morgensztern D, Read W, Tierney R, Vlahiotis A, et al. Changing epidemiology of small-cell lung cancer in the United States over the last 30 years: analysis of the surveillance, epidemiologic, and end results database. J Clin Oncol. 2006 Oct 1;24(28):4539–44.

10. Osmani L, Askin F, Gabrielson E, Li QK. Current WHO guidelines and the critical role of immunohistochemical markers in the subclassification of non-small cell lung carcinoma (NSCLC): Moving from targeted therapy to immunotherapy. Semin Cancer Biol. 2018 Oct;52(Pt 1):103–9.

11. Dayanc B, Eris S, Senturk S. Challenges in First-Line Osimertinib Therapy in EGFR-Mutant Non-small Cell Lung Cancer: Acquired Resistance Is the Issue. In Cham: Springer International Publishing; 2022 [cited 2024 Aug 12]. (Interdisciplinary Cancer Research). Available from: https://link.springer.com/10.1007/16833_2022_54

12. Chevallier M, Borgeaud M, Addeo A, Friedlaender A. Oncogenic driver mutations in non-small cell lung cancer: Past, present and future. World J Clin Oncol. 2021 Apr 24;12(4):217–37.

13. Bannoura SF, Uddin MH, Nagasaka M, Fazili F, Al-Hallak MN, Philip PA, et al. Targeting KRAS in pancreatic cancer: new drugs on the horizon. Cancer Metastasis Rev. 2021 Sep;40(3):819–35.

14. Zhu G, Pei L, Xia H, Tang Q, Bi F. Role of oncogenic KRAS in the prognosis, diagnosis and treatment of colorectal cancer. Mol Cancer. 2021 Nov 6;20(1):143.

15. Skoulidis F, Li BT, Dy GK, Price TJ, Falchook GS, Wolf J, et al. Sotorasib for Lung Cancers with KRAS p.G12C Mutation. N Engl J Med. 2021 Jun 24;384(25):2371–81.

16. Taniue K, Akimitsu N. Fusion Genes and RNAs in Cancer Development. Noncoding RNA. 2021 Feb 4;7(1):10.

17. Herbst RS, Morgensztern D, Boshoff C. The biology and management of non-small cell lung cancer. Nature. 2018 Jan 24;553(7689):446–54.

18. Yoneda K, Imanishi N, Ichiki Y, Tanaka F. Treatment of Non-small Cell Lung Cancer with EGFR-mutations. J UOEH. 2019;41(2):153–63.

19. Wang Z. ErbB Receptors and Cancer. Methods Mol Biol. 2017;1652:3–35.

20. Roskoski R. The ErbB/HER family of protein-tyrosine kinases and cancer. Pharmacological Research. 2014 Jan 1;79:34–74.

21. Kumagai S, Koyama S, Nishikawa H. Antitumour immunity regulated by aberrant ERBB family signalling. Nat Rev Cancer. 2021 Mar;21(3):181–97.

22. Mendrola JM, Shi F, Park JH, Lemmon MA. Receptor tyrosine kinases with intracellular pseudokinase domains. Biochem Soc Trans. 2013 Aug;41(4):1029–36.

23. Olayioye MA, Neve RM, Lane HA, Hynes NE. The ErbB signaling network: receptor heterodimerization in development and cancer. EMBO J. 2000 Jul 3;19(13):3159–67.

24. Mikuličić S, Shamun M, Massenberg A, Franke AL, Freitag K, Döring T, et al. ErbB2/HER2 receptor tyrosine kinase regulates human papillomavirus promoter activity. Front Immunol. 2024 Feb 2;15:1335302.

25. Wee P, Wang Z. Epidermal Growth Factor Receptor Cell Proliferation Signaling Pathways. Cancers (Basel). 2017 May 17;9(5):52.

26. Roskoski R. Small molecule inhibitors targeting the EGFR/ErbB family of protein-tyrosine kinases in human cancers. Pharmacol Res. 2019 Jan;139:395–411.

27. Cheng WL, Feng PH, Lee KY, Chen KY, Sun WL, Van Hiep N, et al. The Role of EREG/EGFR Pathway in Tumor Progression. Int J Mol Sci. 2021 Nov 27;22(23):12828.

28. Kogan EA, Rozhkova EB, Seredin VP, Paltsev MA. [Prognostic value of the expression of thyreoglobulin and oncomarkers (p53, EGFR, ret-oncogene) in different types of papillary carcinoma of the thyroid: clinicomorphological and immunohistochemical studies]. Arkh Patol. 2006;68(4):8–11.

29. Schneider MR, Yarden Y. Structure and function of epigen, the last EGFR ligand. Semin Cell Dev Biol. 2014 Apr;28:57–61.

30. Hsu JL, Hung MC. The role of HER2, EGFR, and other receptor tyrosine kinases in breast cancer. Cancer Metastasis Rev. 2016 Dec;35(4):575–88.

31. Maruyama IN. Mechanisms of Activation of Receptor Tyrosine Kinases: Monomers or Dimers. Cells. 2014 Apr 22;3(2):304–30.

32. Thompson DM, Gill GN. The EGF receptor: structure, regulation and potential role in malignancy. Cancer Surv. 1985;4(4):767–88.

33. Castellanos E, Feld E, Horn L. Driven by Mutations: The Predictive Value of Mutation Subtype in EGFR-Mutated Non-Small Cell Lung Cancer. J Thorac Oncol. 2017 Apr;12(4):612–23.

34. Harrison PT, Vyse S, Huang PH. Rare epidermal growth factor receptor (EGFR) mutations in non-small cell lung cancer. Semin Cancer Biol. 2020 Apr;61:167–79.

35. Shigematsu H, Gazdar AF. Somatic mutations of epidermal growth factor receptor signaling pathway in lung cancers. Int J Cancer. 2006 Jan 15;118(2):257–62.

36. Guo G, Gong K, Wohlfeld B, Hatanpaa KJ, Zhao D, Habib AA. Ligand-Independent EGFR Signaling. Cancer Res. 2015 Sep 1;75(17):3436–41.

37. Leonetti A, Sharma S, Minari R, Perego P, Giovannetti E, Tiseo M. Resistance mechanisms to osimertinib in EGFR-mutated non-small cell lung cancer. Br J Cancer. 2019 Oct;121(9):725–37.

38. Gazdar AF. Activating and resistance mutations of EGFR in non-small-cell lung cancer: role in clinical response to EGFR tyrosine kinase inhibitors. Oncogene. 2009 Aug;28 Suppl 1(Suppl 1):S24-31.

39. Sharma SV, Bell DW, Settleman J, Haber DA. Epidermal growth factor receptor mutations in lung cancer. Nat Rev Cancer. 2007 Mar;7(3):169–81.

40. Rosenzweig SA. Acquired Resistance to Drugs Targeting Tyrosine Kinases. Adv Cancer Res. 2018;138:71–98.

41. Purba ER, Saita EI, Maruyama IN. Activation of the EGF Receptor by Ligand Binding and Oncogenic Mutations: The “Rotation Model.” Cells. 2017 Jun 2;6(2):13.

42. Massarelli E, Johnson FM, Erickson HS, Wistuba II, Papadimitrakopoulou V. Uncommon epidermal growth factor receptor mutations in non-small cell lung cancer and their mechanisms of EGFR tyrosine kinase inhibitors sensitivity and resistance. Lung Cancer. 2013 Jun;80(3):235–41.

43. Ferguson KM. A structure-based view of Epidermal Growth Factor Receptor regulation. Annu Rev Biophys. 2008;37:353–73.

44. Tamirat MZ, Koivu M, Elenius K, Johnson MS. Structural characterization of EGFR exon 19 deletion mutation using molecular dynamics simulation. PLoS One. 2019 Sep 19;14(9):e0222814.

45. Sutto L, Gervasio FL. Effects of oncogenic mutations on the conformational free-energy landscape of EGFR kinase. Proc Natl Acad Sci U S A. 2013 Jun 25;110(26):10616–21.

46. Yun CH, Boggon TJ, Li Y, Woo MS, Greulich H, Meyerson M, et al. Structures of lung cancer-derived EGFR mutants and inhibitor complexes: mechanism of activation and insights into differential inhibitor sensitivity. Cancer Cell. 2007 Mar;11(3):217–27.

47. Carey KD, Garton AJ, Romero MS, Kahler J, Thomson S, Ross S, et al. Kinetic Analysis of Epidermal Growth Factor Receptor Somatic Mutant Proteins Shows Increased Sensitivity to the Epidermal Growth Factor Receptor Tyrosine Kinase Inhibitor, Erlotinib. Cancer Research. 2006 Aug 15;66(16):8163–71.

48. Shigematsu H, Lin L, Takahashi T, Nomura M, Suzuki M, Wistuba II, et al. Clinical and Biological Features Associated With Epidermal Growth Factor Receptor Gene Mutations in Lung Cancers. JNCI: Journal of the National Cancer Institute. 2005 Mar 2;97(5):339–46.

49. Levitzki A, Gazit A. Tyrosine kinase inhibition: an approach to drug development. Science. 1995 Mar 24;267(5205):1782–8.

50. Arora A, Scholar EM. Role of tyrosine kinase inhibitors in cancer therapy. J Pharmacol Exp Ther. 2005 Dec;315(3):971–9.

51. Ebrahimi N, Fardi E, Ghaderi H, Palizdar S, Khorram R, Vafadar R, et al. Receptor tyrosine kinase inhibitors in cancer. Cell Mol Life Sci. 2023 Mar 22;80(4):104.

52. Amelia T, Kartasasmita RE, Ohwada T, Tjahjono DH. Structural Insight and Development of EGFR Tyrosine Kinase Inhibitors. Molecules. 2022 Jan 26;27(3):819.

53. Karachaliou N, Fernandez-Bruno M, Bracht JWP, Rosell R. EGFR first- and second-generation TKIs—there is still place for them in EGFR-mutant NSCLC patients. Transl Cancer Res. 2019 Jan;8(Suppl 1):S23–47.

54. Mok TS, Wu YL, Thongprasert S, Yang CH, Chu DT, Saijo N, et al. Gefitinib or carboplatin-paclitaxel in pulmonary adenocarcinoma. N Engl J Med. 2009 Sep 3;361(10):947–57.

55. Rosell R, Carcereny E, Gervais R, Vergnenegre A, Massuti B, Felip E, et al. Erlotinib versus standard chemotherapy as first-line treatment for European patients with advanced EGFR mutation-positive non-small-cell lung cancer (EURTAC): a multicentre, open-label, randomised phase 3 trial. Lancet Oncol. 2012 Mar;13(3):239–46.

56. Zhao Q, Cheng J, Chen P, Sun J, Guan S. Icotinib: efficacy in different solid tumors and gene mutations. Anticancer Drugs. 2020 Mar;31(3):205–10.

57. Riely GJ, Politi KA, Miller VA, Pao W. Update on epidermal growth factor receptor mutations in non-small cell lung cancer. Clin Cancer Res. 2006 Dec 15;12(24):7232–41.

58. Wu YL, Zhou C, Liam CK, Wu G, Liu X, Zhong Z, et al. First-line erlotinib versus gemcitabine/cisplatin in patients with advanced EGFR mutation-positive non-small-cell lung cancer: analyses from the phase III, randomized, open-label, ENSURE study. Ann Oncol. 2015 Sep;26(9):1883–9.

59. Shi YK, Wang L, Han BH, Li W, Yu P, Liu YP, et al. First-line icotinib versus cisplatin/pemetrexed plus pemetrexed maintenance therapy for patients with advanced EGFR mutation-positive lung adenocarcinoma (CONVINCE): a phase 3, open-label, randomized study. Ann Oncol. 2017 Oct 1;28(10):2443–50.

60. Fukuoka M, Wu YL, Thongprasert S, Sunpaweravong P, Leong SS, Sriuranpong V, et al. Biomarker analyses and final overall survival results from a phase III, randomized, open-label, first-line study of gefitinib versus carboplatin/paclitaxel in clinically selected patients with advanced non-small-cell lung cancer in Asia (IPASS). J Clin Oncol. 2011 Jul 20;29(21):2866–74.

61. Chhouri H, Alexandre D, Grumolato L. Mechanisms of Acquired Resistance and Tolerance to EGFR Targeted Therapy in Non-Small Cell Lung Cancer. Cancers (Basel). 2023 Jan 13;15(2):504.

62. Yun CH, Mengwasser KE, Toms AV, Woo MS, Greulich H, Wong KK, et al. The T790M mutation in EGFR kinase causes drug resistance by increasing the affinity for ATP. Proc Natl Acad Sci U S A. 2008 Feb 12;105(6):2070–5.

63. Yu HA, Arcila ME, Rekhtman N, Sima CS, Zakowski MF, Pao W, et al. Analysis of tumor specimens at the time of acquired resistance to EGFR-TKI therapy in 155 patients with EGFR-mutant lung cancers. Clin Cancer Res. 2013 Apr 15;19(8):2240–7.

64. Huang L, Jiang S, Shi Y. Tyrosine kinase inhibitors for solid tumors in the past 20 years (2001–2020). Journal of Hematology & Oncology. 2020 Oct 27;13(1):143.

65. Liam CK. The role of osimertinib in epidermal growth factor receptor (EGFR)-mutant non-small cell lung cancer. J Thorac Dis. 2019 Mar;11(Suppl 3):S448–52.

66. Riely GJ. Second-Generation Epidermal Growth Factor Receptor Tyrosine Kinase Inhibitors in Non-small Cell Lung Cancer. Journal of Thoracic Oncology. 2008 Jun 1;3(6, Supplement 2):S146–9.

67. Yu HA, Riely GJ. Second-Generation Epidermal Growth Factor Receptor Tyrosine Kinase Inhibitors in Lung Cancers. 2013 Feb 1 [cited 2024 Aug 18]; Available from: https://jnccn.org/view/journals/jnccn/11/2/article-p161.xml

68. Engelman JA, Zejnullahu K, Gale CM, Lifshits E, Gonzales AJ, Shimamura T, et al. PF00299804, an Irreversible Pan-ERBB Inhibitor, Is Effective in Lung Cancer Models with EGFR and ERBB2 Mutations that Are Resistant to Gefitinib. Cancer Research. 2007 Dec 18;67(24):11924–32.

69. Walter AO, Sjin RTT, Haringsma HJ, Ohashi K, Sun J, Lee K, et al. Discovery of a Mutant-Selective Covalent Inhibitor of EGFR that Overcomes T790M-Mediated Resistance in NSCLC. Cancer Discovery. 2013 Dec 10;3(12):1404–15.

70. Li D, Ambrogio L, Shimamura T, Kubo S, Takahashi M, Chirieac LR, et al. BIBW2992, an irreversible EGFR/HER2 inhibitor highly effective in preclinical lung cancer models. Oncogene. 2008 Aug;27(34):4702–11.

71. Stewart EL, Tan SZ, Liu G, Tsao MS. Known and putative mechanisms of resistance to EGFR targeted therapies in NSCLC patients with EGFR mutations-a review. Transl Lung Cancer Res. 2015 Feb;4(1):67–81.

72. Tan AC, Teh YL, Lai GGY, Tan DSW. Third generation EGFR TKI landscape for metastatic EGFR mutant non-small cell lung cancer (NSCLC). Expert Review of Anticancer Therapy. 2019 Jun 3;19(6):431–5.

73. Nagasaka M, Zhu VW, Lim SM, Greco M, Wu F, Ou SHI. Beyond Osimertinib: The Development of Third-Generation EGFR Tyrosine Kinase Inhibitors For Advanced *EGFR*+ NSCLC. Journal of Thoracic Oncology. 2021 May 1;16(5):740–63.

74. Tan DSW, Leighl NB, Riely GJ, Yang JCH, Sequist LV, Wolf J, et al. Safety and efficacy of nazartinib (EGF816) in adults with *EGFR*-mutant non-small-cell lung carcinoma: a multicentre, open-label, phase 1 study. The Lancet Respiratory Medicine. 2020 Jun 1;8(6):561–72.

75. A Novel Third-generation EGFR Tyrosine Kinase Inhibitor Abivertinib for EGFR T790M-mutant Non–Small Cell Lung Cancer: a Multicenter Phase I/II Study | Clinical Cancer Research | American Association for Cancer Research [Internet]. [cited 2024 Aug 18]. Available from: https://aacrjournals.org/clincancerres/article/28/6/1127/682040/A-Novel-Third-generation-EGFR-Tyrosine-Kinase

76. Zhou W, Ercan D, Chen L, Yun C hong, Li D, Capelletti M, et al. Novel mutant-selective EGFR kinase inhibitors against EGFR T790M. Nature. 2009 Dec 24;462(7276):1070–4.

77. Cross DAE, Ashton SE, Ghiorghiu S, Eberlein C, Nebhan CA, Spitzler PJ, et al. AZD9291, an irreversible EGFR TKI, overcomes T790M-mediated resistance to EGFR inhibitors in lung cancer. Cancer Discov. 2014 Sep;4(9):1046–61.

78. Fu K, Xie F, Wang F, Fu L. Therapeutic strategies for EGFR-mutated non-small cell lung cancer patients with osimertinib resistance. J Hematol Oncol. 2022 Dec 8;15:173.

79. Remon J, Steuer CE, Ramalingam SS, Felip E. Osimertinib and other third-generation EGFR TKI in EGFR-mutant NSCLC patients. Annals of Oncology. 2018 Jan 1;29:i20–7.

80. Li Y, Mao T, Wang J, Zheng H, Hu Z, Cao P, et al. Toward the next generation EGFR inhibitors: an overview of osimertinib resistance mediated by EGFR mutations in non-small cell lung cancer. Cell Commun Signal. 2023 Apr 11;21:71.

81. Gomatou G, Syrigos N, Kotteas E. Osimertinib Resistance: Molecular Mechanisms and Emerging Treatment Options. Cancers. 2023 Jan;15(3):841.

82. Finlay MRV, Anderton M, Ashton S, Ballard P, Bethel PA, Box MR, et al. Discovery of a potent and selective EGFR inhibitor (AZD9291) of both sensitizing and T790M resistance mutations that spares the wild type form of the receptor. J Med Chem. 2014 Oct 23;57(20):8249–67.

83. Colclough N, Chen K, Johnström P, Strittmatter N, Yan Y, Wrigley GL, et al. Preclinical Comparison of the Blood-brain barrier Permeability of Osimertinib with Other EGFR TKIs. Clin Cancer Res. 2021 Jan 1;27(1):189–201.

84. Mok TS, Wu YL, Ahn MJ, Garassino MC, Kim HR, Ramalingam SS, et al. Osimertinib or Platinum–Pemetrexed in EGFR T790M–Positive Lung Cancer. New England Journal of Medicine. 2017 Feb 16;376(7):629–40.

85. Overall Survival with Osimertinib in Untreated, EGFR-Mutated Advanced NSCLC | New England Journal of Medicine [Internet]. [cited 2024 Aug 18]. Available from: https://www.nejm.org/doi/full/10.1056/NEJMoa1913662

86. Tsuboi M, Herbst RS, John T, Kato T, Majem M, Grohé C, et al. Overall Survival with Osimertinib in Resected EGFR-Mutated NSCLC. New England Journal of Medicine. 2023 Jul 12;389(2):137–47.

87. Zalaquett Z, Catherine Rita Hachem M, Kassis Y, Hachem S, Eid R, Raphael Kourie H, et al. Acquired resistance mechanisms to osimertinib: The constant battle. Cancer Treatment Reviews. 2023 May 1;116:102557.

88. Gristina V, Malapelle U, Galvano A, Pisapia P, Pepe F, Rolfo C, et al. The significance of epidermal growth factor receptor uncommon mutations in non-small cell lung cancer: A systematic review and critical appraisal. Cancer Treat Rev. 2020 Apr;85:101994.

89. Nagasaka M, Balmanoukian AS, Madison R, Zhang SS, Klempner SJ, Ou SHI. Amivantamab (JNJ-61186372) induces clinical, biochemical, molecular, and radiographic response in a treatment-refractory NSCLC patient harboring amplified triple EGFR mutations (L858R/ T790M/G796S) in cis. Lung Cancer. 2022 Feb;164:52–5.

90. Watanabe S, Goto Y, Yasuda H, Kohno T, Motoi N, Ohe Y, et al. HSP90 inhibition overcomes amplification-induced resistance to third-generation EGFR-TKIs. Thoracic Cancer. 2021;12(5):631–42.

91. Mu Y, Hao X, Xing P, Hu X, Wang Y, Li T, et al. Acquired resistance to osimertinib in patients with non-small-cell lung cancer: mechanisms and clinical outcomes. J Cancer Res Clin Oncol. 2020 Sep 1;146(9):2427–33.

92. Oxnard GR, Hu Y, Mileham KF, Husain H, Costa DB, Tracy P, et al. Assessment of Resistance Mechanisms and Clinical Implications in Patients With EGFR T790M–Positive Lung Cancer and Acquired Resistance to Osimertinib. JAMA Oncology. 2018 Nov 1;4(11):1527–34.

93. Ghasemi M, Turnbull T, Sebastian S, Kempson I. The MTT Assay: Utility, Limitations, Pitfalls, and Interpretation in Bulk and Single-Cell Analysis. Int J Mol Sci. 2021 Nov 26;22(23):12827.

94. Feoktistova M, Geserick P, Leverkus M. Crystal Violet Assay for Determining Viability of Cultured Cells. Cold Spring Harb Protoc. 2016 Apr 1;2016(4):pdb.prot087379.

95. Kim B. Western Blot Techniques. Methods Mol Biol. 2017;1606:133–9.

96. Martin M. Cutadapt removes adapter sequences from high-throughput sequencing reads. EMBnet.journal. 2011 May 2;17(1):10–2.

97. Frankish A, Carbonell-Sala S, Diekhans M, Jungreis I, Loveland JE, Mudge JM, et al. GENCODE: reference annotation for the human and mouse genomes in 2023. Nucleic Acids Res. 2023 Jan 6;51(D1):D942–9.

98. Liao Y, Smyth GK, Shi W. The Subread aligner: fast, accurate and scalable read mapping by seed-and-vote. Nucleic Acids Res. 2013 May 1;41(10):e108.

99. Liao Y, Smyth GK, Shi W. featureCounts: an efficient general purpose program for assigning sequence reads to genomic features. Bioinformatics. 2014 Apr 1;30(7):923–30.

100. Bioconductor [Internet]. [cited 2024 Aug 18]. edgeR. Available from: http://bioconductor.org/packages/edgeR/

101. Subramanian A, Tamayo P, Mootha VK, Mukherjee S, Ebert BL, Gillette MA, et al. Gene set enrichment analysis: a knowledge-based approach for interpreting genome-wide expression profiles. Proc Natl Acad Sci U S A. 2005 Oct 25;102(43):15545–50.

102. Amaral MVS, Portilho AJDS, Silva ELD, Sales LDO, Maués JHDS, Moraes MEAD, et al. Establishment of Drug-resistant Cell Lines as a Model in Experimental Oncology: A Review. Anticancer Research. 2019 Dec 1;39(12):6443–55.

103. Nishihara S, Yamaoka T, Ishikawa F, Ohmori T, Ando K, Kusumoto S, et al. Diverse Mechanisms of Resistance against Osimertinib, a Third-Generation EGFR-TKI, in Lung Adenocarcinoma Cells with an EGFR-Activating Mutation. Cells. 2022 Jul 14;11(14):2201.

104. Li L, Gu X, Yue J, Zhao Q, Lv D, Chen H, et al. Acquisition of EGFR TKI resistance and EMT phenotype is linked with activation of IGF1R/NF-κB pathway in EGFR-mutant NSCLC. Oncotarget. 2017 Sep 21;8(54):92240–53.

105. Lee CS, Milone M, Seetharamu N. Osimertinib in EGFR-Mutated Lung Cancer: A Review of the Existing and Emerging Clinical Data. Onco Targets Ther. 2021;14:4579–97.

106. Tang ZH, Lu JJ. Osimertinib resistance in non-small cell lung cancer: Mechanisms and therapeutic strategies. Cancer Lett. 2018 Apr 28;420:242–6.

107. Qin Q, Li X, Liang X, Zeng L, Wang J, Sun L, et al. Targeting the EMT transcription factor Snail overcomes resistance to osimertinib in EGFR-mutant non-small cell lung cancer. Thorac Cancer. 2021 Jun;12(11):1708–15.

108. Takahashi A, Seike M, Chiba M, Takahashi S, Nakamichi S, Matsumoto M, et al. Ankyrin Repeat Domain 1 Overexpression is Associated with Common Resistance to Afatinib and Osimertinib in EGFR-mutant Lung Cancer. Sci Rep. 2018 Oct 5;8(1):14896.

109. Ohara S, Suda K, Mitsudomi T. Cell Line Models for Acquired Resistance to First-Line Osimertinib in Lung Cancers—Applications and Limitations. Cells. 2021 Feb 9;10(2):354.

110. Bray F, Laversanne M, Sung H, Ferlay J, Siegel RL, Soerjomataram I, et al. Global cancer statistics 2022: GLOBOCAN estimates of incidence and mortality worldwide for 36 cancers in 185 countries. CA Cancer J Clin. 2024;74(3):229–63.

111. Westover D, Zugazagoitia J, Cho BC, Lovly CM, Paz-Ares L. Mechanisms of acquired resistance to first- and second-generation EGFR tyrosine kinase inhibitors. Ann Oncol. 2018 Jan 1;29(suppl_1):i10–9.

112. Jänne PA, Ou SHI, Kim DW, Oxnard GR, Martins R, Kris MG, et al. Dacomitinib as first-line treatment in patients with clinically or molecularly selected advanced non-small-cell lung cancer: a multicentre, open-label, phase 2 trial. Lancet Oncol. 2014 Dec;15(13):1433–41.

113. Ho GF, Chai CS, Alip A, Wahid MIA, Abdullah MM, Foo YC, et al. Real-world experience of first-line afatinib in patients with EGFR-mutant advanced NSCLC: a multicenter observational study. BMC Cancer. 2019 Sep 9;19(1):896.

114. Uribe ML, Marrocco I, Yarden Y. EGFR in Cancer: Signaling Mechanisms, Drugs, and Acquired Resistance. Cancers (Basel). 2021 Jun 1;13(11):2748.

115. Tang ZH, Jiang XM, Guo X, Fong CMV, Chen X, Lu JJ. Characterization of osimertinib (AZD9291)-resistant non-small cell lung cancer NCI-H1975/OSIR cell line. Oncotarget. 2016 Dec 6;7(49):81598–610.

116. Yu HA, Arcila ME, Hellmann MD, Kris MG, Ladanyi M, Riely GJ. Poor response to erlotinib in patients with tumors containing baseline EGFR T790M mutations found by routine clinical molecular testing. Ann Oncol. 2014 Feb;25(2):423–8.

117. Li L, Li Z, Lu C, Li J, Zhang K, Lin C, et al. Ibrutinib reverses IL-6-induced osimertinib resistance through inhibition of Laminin α5/FAK signaling. Commun Biol. 2022 Feb 23;5(1):155.

118. Activation of insulin-like growth factor-1 receptor confers acquired resistance to osimertinib in non-small cell lung cancer with EGFR T790M mutation - PubMed [Internet]. [cited 2024 Aug 18]. Available from: https://pubmed.ncbi.nlm.nih.gov/31758670/

8. APPENDICES

İZMİR BİYOTIP VE GENOM MERKEZİ
GİRİŞİMSEL OLMAYAN ARAŞTIRMALAR ETİK KURULU (İBG-GOEK)
KARARI

Toplantı Tarihi	: 30/12/2022	**Toplantı Günü**	: Cuma
Toplantı Sayısı	: 16	**Toplantı Saati**	: 10:30

Sayın Doç. Dr. Şerif ŞENTÜRK,

2022-043 Protokol No'lu; sorumlusu olduğunuz "Osimertinib Dirençli Küçük Hücreli Dışı Akciğer Kanseri Hücre Modellerinin Geliştirilmesi ve Karakterizasyonu" başlıklı araştırmanın uygulanmasında etik açıdan sakınca olmadığına oy birliği ile karar verilmiştir.

Bilgilerinizi ve gereğini rica ederiz.

Prof. Dr. H. Alper BAĞRIYANIK **Başkan**	**Dr. Serap ERKEK ÖZHAN** **Başkan Yardımcısı**
Prof. Dr. Sedef AKGÜNGÖR **Üye**	**Prof. Dr. İnci ALACACIOĞLU** **Üye** (Katılmadı)
Prof. Dr. Gülgün OKTAY **Üye**	**Prof. Dr. Hilmi ORHAN** **Üye** (Katılmadı)
Prof. Dr. Şermin GENÇ **Üye** (Katılmadı)	**Doç. Dr. Canan Aslı YILDIRIM** **Üye** (Katılmadı)
Doç. Dr. Can KÜÇÜK **Üye**	**Dr. Öğr. Üyesi Yavuz OKTAY** **Üye**

SUDE ERİŞ

Personal Information

Contact Information

Contact Address

Phone

Email

Web Page

Education Information

26 January 2022 - Now (2 Year 8 Month)
Yüksek Lisans, Tezli Program, DOKUZ EYLÜL ÜNİVERSİTESİ, TÜRKİYE
İZMİR ULUSLARARASI BİYOTIP VE GENOM ENSTİTÜSÜ, MOLEKÜLER BİYOLOJİ VE GENETİK (YL) (TEZLİ) (İNGİLİZCE)

15 August 2016 - 22 June 2021 (4 Year 11 Month)
Lisans, Anadal/Normal Öğretim, KADİR HAS ÜNİVERSİTESİ, TÜRKİYE
MÜHENDİSLİK VE DOĞA BİLİMLERİ FAKÜLTESİ, BİYOENFORMATİK VE GENETİK PR. (İNGİLİZCE) (TAM BURSLU)
Diploma Number: 2021-17-15373
Cumulative Grade Point Average: 3.95 / 4.0

Experience Information

February 2021 - Now (3 Year 8 Month) (Tam Zamanlı)
DİĞER, İZMİR BİYOTIP VE GENOM MERKEZİ

Foreign Language Information

İNGİLİZCE (Reading: İyi, Writing: İyi, Speaking: İyi)

R&D Competency

Books

B. ULUATA DAYANÇ, S. ERİŞ & Ş. ŞENTÜRK, Challenges in First-Line Osimertinib Therapy in EGFR-Mutant Non-small Cell Lung Cancer: Acquired Resistance Is the Issue, N. REZAEİ [Editors], Interdisciplinary Cancer Research(1 - 33): Springer, 08 October 2022, Kitapta Bölüm.

Articles

A. KURDEN-PEKMEZCİ, E. CAKİROGLU, S. ERİS, F. A. MAZİ, O. S. COSKUN-DENİZ, E. DALGİC, O. OZ & S. SENTURK, MALT1 paracaspase is overexpressed in hepatocellular carcinoma and promotes cancer cell survival and growth, LIFE SCIENCES, 2023, 0024-3205, 323.

Conference Papers

M. KALYONCU, D. DEMİRCİ, S. ERİŞ, B. ULUATA DAYANÇ, E. ÇAKIROĞLU, M. BAŞOL, M. UYSAL, G. ÇAKAN AKDOĞAN, G. KARAKÜLAH & Ş. ŞENTÜRK, Escape from TGF-ß-induced Senescence Promotes Aggressive Cancer Hallmarks in Epithelial Hepatocellular Carcinoma Cells, Poster Sunumu, The 2024 Annual Congress of the European Association for Cancer Research (EACR 2024), 10 June 2024, 13 June 2024, 1574-7891, 347 - 348.

E. ÇAKIROĞLU, S. ERİŞ, Ö. ÖZ, G. KARAKÜLAH & Ş. ŞENTÜRK, Exploring Cancer Dependencies with Genome-Wide CRISPR Screens: Unveiling BUB1 Kinase as a Druggable Vulnerability in Malignant Pleural Mesothelioma, Poster Sunumu, The 2024 Annual Congress of the European Association for Cancer Research (EACR 2024), 10 June 2024, 13 June 2024, 1574-7891, 183 - 184.

B. AKDEMİR, S. ERİŞ, M. KALYONCU, E. ÇAKIROĞLU, Ö. Ş. COŞKUN, G. KARAKÜLAH & Ş. ŞENTÜRK, Genome-wide CRISPR Screening Identifies RUVBL1/2 Complex as a Druggable Vulnerability in Bladder Cancer, Poster Sunumu, The 2024 Annual Congress of the European Association for Cancer Research (EACR 2024), 10 June 2024, 13 June 2024, 1574-7891, 180 - 181.

B. ULUATA DAYANÇ, S. ERİŞ, E. ÇAKIROĞLU, G. ÖZDEN YILMAZ, N. E. GÜLFIRAT, Ö. Ş. COŞKUN, G. KARAKÜLAH, S. ERKEK ÖZHAN & Ş. ŞENTÜRK, Pooled CRISPR Screening Identifies AP-1Transcription Factor as a Druggable Driver of Osimertinib Resistance in Non-Small Cell Lung Cancer, Sözlü Sunum, The 2024 Annual Congress of the European Association for Cancer Research (EACR 2024) , 10 June 2024, 13 June 2024, 1574-7891, 224 - 224.

B. ULUATA DAYANÇ, S. ERİŞ, E. ÇAKIROĞLU, F. A. MAZI, Ö. Ş. COŞKUN, D. DEMİRCİ, G. KARAKÜLAH & Ş. ŞENTÜRK, EP08.02-022 Investigating Partners in Crime: Osimertinib Resistance Mechanisms in Non-small Cell Lung Cancer Using Focused CRISPR Screen, Poster Sunumu, The 2022 World Conference on Lung Cancer, 06 August 2022, 09 August 2022.

B. ULUATA DAYANÇ, S. ERİŞ, E. ÇAKIROĞLU, G. ÖZDEN YILMAZ, Ö. Ş. COŞKUN, S. ERKEK ÖZHAN, G. KARAKÜLAH & Ş. ŞENTÜRK, Osimertinib Resistance Mechanisms in Non-small Cell Lung Cancer Using Focused CRISPR Screen: FOSL1 and JUN, Poster Sunumu, The 47th FEBS Congress, 08 July 2022, 12 July 2022.

B. ULUATA DAYANÇ, S. ERİŞ, E. ÇAKIROĞLU, F. A. MAZI, Ö. Ş. COŞKUN, D. DEMİRCİ, G. KARAKÜLAH & Ş. ŞENTÜRK, Investigating Non-Genetic Osimertinib Resistance Mechanisms in Non-small Cell Lung Cancer Using Focused CRISPR Screen., Sözlü Sunum, XVII. Congress of Medical Biology and Genetics, 28 October 2021, 31 October 2021.

TÜBİTAK Scholarships and Fundings

Project Info

122Z890, Küçük Hücreli Dışı Akciğer Kanseri Tedavisinde Osimertinib Direnci: Fosl1 Ve Jun Transkripsiyon Faktörlerinin Rolü Ve Sentetik Letal Etkileşimleri, Burslu, Yürürlükte, KBAG - Kimya Biyoloji Araştırma Destek Grubu, 1001 - Araştırma, ARDEB, Project Participation/Leave Dates: 7/3/23 - (), Project Start/End Dates: 4/1/23 - 4/1/26.

119Z540, Egfr-Mutant Küçük Hücreli Dışı Akciğer Kanseri'nde Birinci Basamak Osimertinib Tedavisinde Gelişen Edinsel Dirençte Epigenetik ve Transkripsiyonel Faktörlerin Rolünün Araştırılması, Burslu, Sonuçlandı, KBAG - Kimya Biyoloji Araştırma Destek Grubu, Uluslararası / ABD-NSF, ARDEB, Project Participation/Leave Dates: 2/1/21 - 8/1/21, Project Start/End Dates: 11/15/19 - 5/15/23.

119Z540, Egfr-Mutant Küçük Hücreli Dışı Akciğer Kanseri'nde Birinci Basamak Osimertinib Tedavisinde Gelişen Edinsel Dirençte Epigenetik ve Transkripsiyonel Faktörlerin Rolünün Araştırılması, BİDEB Burslusu, Sonuçlandı, KBAG - Kimya Biyoloji Araştırma Destek Grubu, Uluslararası / ABD-NSF, ARDEB, Project Participation/Leave Dates: 8/1/22 - 5/15/23, Project Start/End Dates: 11/15/19 - 5/15/23.

BIDEB Supports

SUDE ERİŞ, Araştırma Burs ve Destekleri Müdürlüğü, 2247-C Stajyer Araştırmacı Burs Programı (STAR)- Star Lisans, Destek Sona Erdi, 2020 - 2.

SUDE ERİŞ, Etkinlik Destekleri ve Eğitim Bursları Müdürlüğü, 2210-A Genel Yurt İçi Yüksek Lisans Burs Programı, Bursu Kesildi, 2022 - 1, 3/1/22 - 2/29/24.

Number of Panelist/Observer/Reporter Jobs

Job	ARDEB	BIDEB	SCIENCE	SOCIETY	UIDB	TEYDEB	Total
Refereeing/Panelist/Outer Consultant Count	0	0	0		0	0	0
Moderatorships Count	0	0	0		0	0	0
Number of Observer/Consultant Jobs	0	0	0		0	0	0
Number of Reporter Jobs	0	0	0		0	0	0
Not Attended Refereeing/Panelist/Outer	0	0	0		0	0	0